TECHNISCHE UNIVERSITÄT MÜNCHEN

Walter Schottky Institut

Zentralinstitut für physikalische Grundlagen der Halbleiterelektronik

# GaN Heterostructures for Biosensing and Radiation Detection

John D. Howgate

Vollständiger Abdruck der von der Fakultät für Physik der Technischen Universität München zur Erlangung des akademischen Grades eines

Doktors der Naturwissenschaften (Dr. rer. nat.)

genehmigten Dissertation.

| | |
|---|---|
| Vorsitzender: | Univ.-Prof. Dr. Peter Vogl |
| Prüfer der Dissertation: | 1. Univ.-Prof. Dr. Martin Stutzmann |
| | 2. Priv.-Doz. Dr. Stefan Thalhammer, Universität Augsburg |

Die Dissertation wurde am 04.12.2012 bei der Technischen Universität München eingereicht und durch die Fakultät für Physik am 11.12.2012 angenommen.

# Abstract

In this thesis I show the results from our investigation of the interface between gallium nitride wide bandgap semiconductor heterostructures and (bio)molecular systems on their surfaces for biosensing, bioelectronics, and photoelectric applications, with a large emphasis on the processes arising from high energy ionizing irradiation, including heterostructure photoelectric gain mechanisms. Wide bandgap semiconductors, such as gallium nitride, have received increasing attention as potential components in advanced organic/inorganic hybrid systems. Working to further this topic, we determine a new semiconductor alignment required for low energy photo-induced charge transfer ionization of alkyl chains well below the energy normally required for molecular cleavage, show original results of the influence of binding methods on enzyme functionality in conjunction with a novel electrochemical and environmental control system and demonstrate new possibilities to significantly improve upon *p*H measurements through the use of high sensitivity devices. Furthermore, based on the extension of this work to support future studies of radiation effects on cell systems, we present a detailed characterization of new simultaneous chemical sensing and ionizing radiation dosimetry using single devices. We found that their *p*H sensitivity was retained during X-ray irradiation and that the fundamental characteristics can be used to separate the irradiation signal from the *p*H response without compromising operational stability. These data provide clear indications of the separate response mechanism tied to the presence of a two-dimensional electron gas channel. Here, we found new results exhibiting exceptionally high gains and independence of the well-known persistent photoconductivity for soft X-rays and high energy particles in the ultralow dose-rate regime. This material system provides the capability for high sensitivity and resolution real time monitoring, which is competitive with and complements state-of-the-art detectors. Thus, is extremely promising for future applications ranging from advanced organic/inorganic hybrid systems to medical imaging.

# Contents

# 1 Introduction

This thesis investigates several linked questions covering device optimization, hybrid semiconductor/(bio)molecular interfaces and the semiconductor photoresponse to ionizing radiation. In the first section (**1.1**), several literature reviews are presented, each summarizing the relevant scientific findings up to the original questions that this work is based on. This is followed, in the second section (**1.2**), by the scope, where a short overview of how these questions are tackled is presented together with the corresponding publications to which I made a significant contribution. Furthermore, a short summary can also be found directing the reader to where in this thesis each topic is discussed in more detail. Moreover, **Section 6.1** repeats these questions followed by a summary of our findings and conclusions.

## 1.1 Literature Review

Detailed understanding of charge transfer mechanisms, for example between inorganic semiconductors and organic molecules, is of fundamental importance in the emerging field of molecular and bio-molecular electronics. Wide bandgap semiconductors, such as gallium nitride (GaN) and silicon carbide (SiC), have received increasing attention as potential components in advanced semiconductor/(bio)molecular detection systems.[1] Furthermore, the Fermi levels of both materials can be varied over a wide energetic range by controlled impurity incorporation, and both have the possibility for bandgap engineering.[2,3] This makes them excellent candidates for creating a direct electrical coupling to an organic interface, and various proven routes have been developed to covalently immobilize self-assembled monolayers (SAMs) of active molecules onto inorganic surfaces from either liquid or gas phases.[4–8] While thiol-based processes have been intensively studied for both metals[9] and semiconductors,[10,11] the silanization-based process,[12,13] in which organosilane molecules react with hydroxyl-terminated surfaces in the presence of water to yield organic monolayers bound over a crosslinked Si-O-Si

network,[14] has recently attracted attention. Although these reactions are typically performed on thin hydroxyl-terminated silica films on Si, both GaN and SiC surfaces can be readily hydroxyl-activated, and the covalent functionalization of both materials with silane monolayers has recently been demonstrated.[15,16] So far, such hybrid (bio)molecular/semiconductor interfaces have largely been used as passive bio-electronic elements, even though many organic systems possess energetic levels whose occupation could be altered by direct electronic charge transfer to or from a semiconductor substrate.[17–19] However, it is hitherto unknown whether it is possible to identify a compatible energetic window for GaN or SiC, within which it is favorable for selected organic systems to be actively charged or discharged by direct interaction with the semiconductor substrate.

A well-known advantage of a selected few wide bandgap semiconductors, such as GaN, is the possibility to create high electron mobility transistors (HEMT) through the introduction of GaN/aluminum gallium nitride (AlGaN) heterointerfaces.[20,21] With an additional GaN capping layer to terminate the less chemically stable AlGaN uppermost layer of the heterointerface, the devices have been frequently used as sensors operated in electrolytes,[22–29] and are known to have a highly linear *p*H sensitivity,[30,31] which can be explained by the site-binding model.[32,33] There are many reported ways to increase the transconductive sensitivity of such devices,[29] but the only suggestion to achieve this through the reduction of the two-dimensional electron gas (2DEG)-to-surface distance was, so far, by using the N-face polarity heterostructure.[34] However, this approach leads to structures with lower chemical stability[35] and the growth of N-face heterostructures is not well established, making it difficult to obtain high quality material.[36] Here, recent improvements in plasma-assisted molecular beam epitaxial growth of aluminum nitride (AlN)/GaN structures allow for a very thin AlN barrier, while retaining a 2DEG with high electron concentrations, without a significant reduction of the electron mobility.[37] In spite of the benefits that such a reduction of barrier thickness would give to device performance, sensor applications using AlN/GaN-based HEMT structures have not yet been studied.

The advancement and simplification of analytic screening and biomedical monitoring requires in-depth knowledge of how to bind a bio-receptor, which translates information

from the biochemical domain into a physical or chemical signal with defined sensitivity, to the active surface of a transducer, which in turn transforms the output signal of the bio-receptor into a measurable and processable signal, and what impact the immobilization method has on this signal. The previously discussed GaN devices have been categorized as biocompatible,[22,38] and exhibit excellent characteristics for bio-electronic applications, which have been directly demonstrated through the recording of cardiac myocyte syncytium action potentials.[23] Furthermore, GaN surfaces have been chemically functionalized by deposition of self-assembled organosilane monolayers. Here, the subsequent immobilization of biomolecules and the electronic detection of protein adsorption has been verified.[15,39] Therefore, they should be well suited to monitor the activity of enzymes immobilized on their surface,[40] where the change in potential of the devices ion sensitive surface, caused by enzymatically catalyzed products, is measured.[41,42] As it is known from the development of various ion sensitive field effect transistor (ISFET)-based enzyme sensors the sensing performance, that is the sensitivity, response time, detection range, and lifetimes, is determined by numerous contributions such as enzyme activity, enzyme concentration, mass transport, thickness, and porosity of the sensing layer.[43] Thereby, the immobilization method to couple the enzymatic recognition layer to the device surface plays a crucial role. While the development of such sensors has been a major field of interest,[44–50] there has not been a systematic comparison with respect to the techniques applied for enzyme immobilization or their effects on enzyme activity.

Clinical treatment procedures, such as external beam radiotherapy, intensity-modulated radiation therapy and stereotactic radiotherapy, as well as conventional X-ray examinations and computer tomography, are important and increasingly utilized tools in modern medicine. The rapid improvement of interventional radiology, which results in high X-ray doses due to long exposure times, contributes to the global average radiation exposure from medical applications.[51] To combat this, the development of devices with high spatial, temporal, energy, and dose resolutions to high energy ionizing radiation are of significant interest, and have been vigorously pursued.[52] While ionization chambers are highly reliable, and thus widely used in medical dosimetry, they have poor spatial resolution,[53] show an angular dependence, and integrate over dose gradients.[54] In recent

years, several devices have been developed that have higher spatial resolution than ionization chambers,[54–58] but they also possess a number of disadvantages, for example:

- Metal oxide semiconductor field effect transistors (MOSFETs),[59] silicon (Si) strip detectors,[60] Si photomultipliers,[61] and Si drift detectors[62] are all based on a well-established material that has a known limited lifetime,[63] corresponding to a total received dose below 200 Gy.[54]
- Bulk gallium arsenide (GaAs),[64] diamond,[56,65,66] and SiC devices[67] are based on radiation hard materials, but their defect-related photo-dynamics have dominated device performance in a largely irreproducible manner.

In fact, the luminescence of such defects in GaN has already been used for scintillation detectors.[68] However, due to its remarkable tolerance to high energy ionizing irradiation[69–71] GaN was recently suggested as a potential replacement for Si as a semiconductor detector material[72,73] and offers a number of advantages over Si, SiC and diamond, such as a larger density, molar mass and a high average atomic number value. However, the X-ray absorption coefficient of GaN is still considered to be small and it is expected that thin films of this material are poorly suited for X-ray dosimetry at energies higher than 20 keV.[74] Furthermore, even in light of recent advances in growth that have led to improved film qualities, GaN is still plagued by, for example, a long transient persistent photoconductivity.[75] Here, even though there are numerous publications on HEMT-based UV detectors,[76–84] and the GaN/AlGaN heterostructure is known to be radiation hard,[85–92] no *in situ* measurements have been performed to evaluate such structures as high energy ionizing radiation dosimeters.

Furthermore, the capability for *in situ* monitoring of biological systems is critically important to the modern medical community, and there is an abundant need of highly sensitive and time-resolved devices which are able to operate in harsh fluidic environments. Apart from microelectrode arrays,[93–95] field effect transistors (FETs)[96] have been applied for the *in vitro* recording of physiological signals. This includes AlGaN/GaN devices,[23] which show promising characteristics for biosensing[22,97] and have additionally been reported to be non-toxic to cells.[22,24] However, a study of real-time changes in the environment, prior to, during and after exposure to ionizing radiation, for

future applications of measuring physiological signals of cells under stress, has not been made.

## 1.2 Scope of this Work

We investigate if a compatible energetic window exists for GaN, within which it is favorable for selected organic systems to be actively charged or discharged by direct interaction with the semiconductor substrate. SiC was chosen as a reference system and underwent rigorous surface and functionalization characterization. The results of the latter investigation are only partially discussed in this thesis, and can be found in full elsewhere.[98,99] Here, we study the impact of illumination on *n*- and *p*-type GaN and SiC with covalently bound SAMs formed from octadecyltrimethoxysilane. By exploiting the large energetic window spanned by the valence and conduction bands of *n*- and *p*-type GaN and SiC, we determine the alignment required to accommodate such a transfer by assessing the stability of the SAMs. The use of simple aliphatic chains provides a model system for the study of charge transfer processes which can be extended to complex biological and hybrid systems in the future.[100–103]

An initial avenue of this work was concerned with the development of techniques to create *pH*-sensitive devices with enhanced sensitivity, resolution and stability. For the challenge of creating highly specific and sensitive devices, a fundamental understanding of electronic noise is of crucial importance. The results of the latter investigation are only partially discussed in this thesis, and can be found in full elsewhere.[104] Here, we demonstrate the enhanced characteristics of AlN/GaN HEMT structures, in which the 2DEG-to-surface distances are reduced in comparison to the AlGaN/GaN structures which are primarily used throughout this thesis, as a *p*H-sensitive solution gate (SG)HEMTs.[105]

Using this device technology, we have investigated the catalytic activity of covalently bound enzymes on the transistor gates by immobilization of penicillinase for detection of the catalytic product penicillic acid from benzylpenicillin. Here, the impact of the immobilization process on enzyme functionality is investigated by the comparison of

covalent and physisorbed immobilization of penicillinase on the GaN gate area of AlGaN/GaN SGHEMT. We found that this type of measurement puts a high demand on equipment capabilities. Therefore, a novel combined electrochemical and environmental control system was designed and constructed to achieve the goals of this project.[101,106,107]

To find out if GaN can overcome difficulties such as long transient persistent photoconductivity and be used for high energy ionizing radiation dosimetry, we investigate the photoreseponse of advanced AlGaN/GaN heterointerfaces, and compare it to the response of GaN thin films. Here, we look at the possibilities of utilizing the built-in electric fields present in GaN-based heterostructures to obtain high gains and fast transient responses in the ultralow dose-rates regimes. The corresponding results, including response time, sensitivity, noise, and energy dependence, are compared to establish a separate response mechanism distinct from conventional photoconduction of GaN thin films. Furthermore, we confirm that the sensors can be used as dose-rate-dependent fluorescence detectors and show the possibility of using the devices for imaging.[101,108–112]

Based on the successful development of processes and instrumentation for precisely controlling and monitoring solution gate devices, we present a detailed characterization of simultaneous chemical sensing and ionizing radiation dosimetry using single devices. Due to the critical importance for *in situ* monitoring of biological systems, which enable the study of possible radiation effects on cell systems in the medical community, a large portion of this work was concerned with extending the characterization of the GaN thin film photo-induced current response to include the medical X-ray spectrum. This enabled the *in vitro* bio-functionality study of radiation effects on cell systems grown on the surfaces of devices. The results are only partially discussed in this thesis, and can be found in full elsewhere.[113–115] Here, we study the device stability while operated in an electrolyte under realistic conditions with photon energies in the medical X-ray regime. We analyze the data evaluating the sensitivity to external X-ray radiation and the sensitivity to *p*H changes in aqueous solutions simultaneously, highlighting the potential for multi-functional *in situ* biosensing and X-ray dosimetry.[101,113,116]

Further details on each topic can be found in the following places: In **Chapter 3**, the enhanced characteristics of AlN/GaN HEMT structures for novel sensors is discussed. In **Chapter 4**, new effects of the hybrid semiconductor/organic interface through the photocatalytic cleavage of self-assembled organic monolayers by UV-induced charge transfer from GaN substrates are discussed, and a new enzyme functionality analysis on immobilization technique through the catalytic activity of enzymes immobilized on AlGaN/GaN SGHEMTs, is discussed in **Sections 4.4 -** Error! Reference source not found.. In **Chapter 5**, the development and evaluation of GaN-based thin films for X-ray dosimetry, including new ultrahigh gain AlGaN/GaN structures, are discussed, and a new study on multi-functional device capabilities through simultaneous real-time X-ray dosimetry and *p*H measurements, is presented.

# 2 Material and Methods

This chapter provides insight into the working principles of different experimental techniques, specific changes made to systems that are not described by the manufacturer, experimental environments, which protocols were used and, where necessary, the specifications of the materials that were used.

## 2.1 Wafers

In this work the following single thin film layers of GaN on sapphire were used:

- 3 µm thick *n*-type GaN was grown by metal organic chemical vapor deposition (MOCVD) (Lumilog, Vallauris, France) on 330µm *c*-plane sapphire substrates. The GaN thin film was Si-doped with a net carrier concentration of n $\approx 10^{18}$ $cm^{-3}$.
- 3 µm thick *p*-type GaN was grown by MOCVD (TopGaN, Warsaw, Poland) on 330 µm *c*-plane sapphire substrates and consisted of the following layer stack: 1.5 µm undoped GaN, 1.5 µm Si-doped GaN, 0.5 µm Mg-doped GaN, and 10 nm of Mg-doped GaN adjusted to p $\approx 10^{18}$ $cm^{-3}$. Similar structures were initially provided by Dr. Eva Monroy (CEA, Grenoble, France).
- 3 µm thick carbon-compensated GaN (GaN:C) thin films grown on 330 µm *c*-plane sapphire with a high sheet resistance from TopGaN Ltd. (Warsaw, Poland).
- 3 µm thick iron-compensated GaN (GaN: Fe) thin films grown on 330 µm *c*-plane sapphire with a sheet resistance of 6 MΩ at 300 K from Lumilog (Vallauris, France).

The SiC samples used in this work were diced from 350 µm thick single-crystalline, (0001)-oriented 6*H*-SiC wafers. The *n*-type wafer was nitrogen doped with n $\approx 10^{18}$ $cm^{-3}$ (CrysTec GmbH, Berlin, Germany) and the *p*-type wafer was aluminum doped with p $\approx 10^{18}$ $cm^{-3}$ (Cree, Inc. Durham, NC, USA). Prior to use, all SiC wafers were polished to a

surface root-mean-square (rms) roughness of approximately 0.3 nm (NovaSiC, Le Bourget du Lac Cedex, France).

HEMT devices were structured from 3µm thick Ga-face GaN films that were grown by MOCVD (TopGaN Ltd., Warsaw, Poland) on a 330 µm thick *c*-plane sapphire substrate. The deposited films, unless otherwise noted, consisted of a 20 nm low temperature GaN layer, a highly resistive 2.9 µm C-compensated GaN buffer layer, a 60 nm nominally undoped GaN layer, a 25 nm $Al_{0.25}Ga_{0.75}N$ barrier layer, and a 3 nm nominally undoped GaN capping layer. The 2DEG, formed just below the heterojunction interface, had a sheet carrier concentration of $n_{2DEG} \approx 8\times10^{12}$ $cm^{-2}$ and a mobility of $\mu \approx 1100$ $cm^2/Vs$ at 300 K. In-depth fabrication methods and physical properties of the HEMT devices are described elsewhere.[20,117]

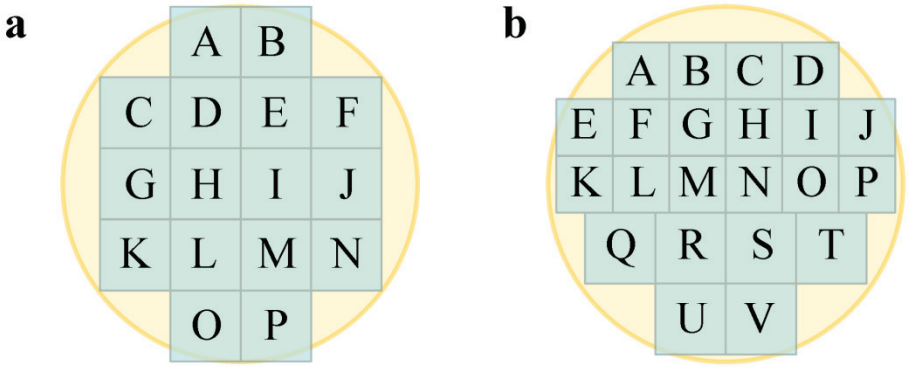


**Figure 1 | Sample Mask for Wafer Dicing. a)** Scheme for a 2" wafer cut into 8×8 $mm^2$ samples. **b)** Scheme for a 2" wafer cut into 8×8 $mm^2$ and 6×6 $mm^2$ samples. Since the center of the wafer is of highest quality, the masks were designed so that samples **a)** H and I as well as **b)** M and N, which were always in the center, could be used for final measurements.

The 2" wafers were diced (Kristal Labor, Physics Department, TUM) according to the patterns in **Figure 1**. This produced 8×8 $mm^2$ or 6×6 $mm^2$ samples. As the center of the wafer is of highest quality, the mask was designed so that samples H and I in **Figure 1a** and M and N in **Figure 1b** were centered and the devices from these pieces were used for final measurements.

GaN samples were cleaned according to a procedure consisting of room temperature ultrasonic agitation (Sononex Digital) in deionized water (18 MΩ/cm, Millipore), acetone

and isopropanol for 10 min each and then were dried with $N_2$ gas. OH-terminated GaN was achieved by treating the sample for 10 min in hot 3:1 solution $H_2SO_4$:$H_2O_2$ followed by 10 min in oxygen plasma using a Technics Plasma 100-E system, operated at 200 W with an oxygen pressure of 1.4 mbar.

## 2.2 Device Processing

### Photolithography

Photolithography, by means of a standard laser-written chrome-on-quartz shadow mask, was used to define areas of the sample surfaces down to feature sizes of 1 µm. AZ5214 reversible photoresist, which consists of the standard positive photoresist based on diazonaphthoquinone and a phenol-formaldehyde resin with a crosslinking agent, was used in accordance with the manufacture's specifications (MicroChemicals, Ulm, Germany). Unless otherwise noted, the resist was spun onto the sample surface for 40 s at 3000 rpm with a 2 s ramping time, which yields a film thickness of 1.6 µm (confirmed by Sloan Dektak 3030 Surface Profile Measuring System). The samples are then soft-baked at 90 °C for an uncritical time of 90 s, primarily to reduce the amount of remaining solvent in the layer. However, this also helps to avoid mask contamination and/or the samples sticking to the mask, prevents popping or foaming of the resist by $N_2$ created during exposure, improves resist adhesion to the substrate, minimizes dark erosion during development, and prevents bubbling during subsequent thermal processes. The sample is then aligned and exposed through a shadow mask for 1.8 s at 18 mW/cm$^2$, where the exposure time is a function of the applied film thickness. Here, upon exposure to light, the diazonaphthoquinone, which inhibits the dissolution of the phenol-formaldehyde resin, increases the dissolution rate beyond that of pure phenol-formaldehyde resin. Exposure to developer at this point would yield what is expected from a positive resist, namely opening the film where it has been exposed and was also utilized in this way for this work. The reversal-bake temperature is very critical (typically 30s at 120 °C on a hotplate) and almost always needs recalibrating before every session, as the cross-linker only becomes active at over 110 °C and the resist starts to thermally crosslink (hard-bake)

at over 130 °C. When activated, the cross-linker binds together all exposed areas of the photoresist. The samples are then flood-exposed (illumination without the shadow mask), to make sure that the areas that have not been cross-linked then become soluble. This step is also non-critical, and 30s at 18mW/cm$^2$ suffices. The samples are then developed with A2400K solution, which is usually a standard aqueous KOH solution for positive resists additionally diluted 1:4, for 30s then 40s in DI water with gentle agitation.

## Etching

Inductively-coupled plasma reactive ion etching (ICP-RIE) (Oxford Instruments, Plasmalab) using chlorine gases was employed to etch the HEMT structure. Active channel regions were defined by a protective, somewhat faster etching, 1.6 µm hard-baked lithographically patterned photoresist.

| Parameter | Value |
|---|---|
| **Initial pressure** | $1.7 \cdot 10^{-5}$ mbar |
| **Pressure** | $40 \cdot 10^{-3}$ mbar |
| **$BCl_3$ gas flow** | 25 sccm |
| **$Cl_2$ gas flow** | 2.5 sccm |
| **Helium backing gas flow** | 10 sccm |
| **Substrate temperature** | 25 °C |
| **DC bias** | 230 V |
| **RF power** | 50 W |
| **ICP power** | 300 W |
| **Process time** | 40 s |

**Table 1 | List of ICP-RIE Initialization Parameters for Calibration.** These values can usually be used in their present state when etching devices with channel widths around 500 µm.

We note that ICP-RIE is very sensitive to any change. In our case, the system was configured to use fluorine gases, and changing over to chlorine gases meant that the optimum etching parameters needed to be found by calibration. Here, the end values could vary as much as 20% between gas changes. To optimize the process, which is especially valid for gate widths below 100 µm, the initialization values, which are

presented in **Table 1**, were used. Normally, wafer edge samples with 500 µm wide gates would be used for calibration, evaluated by scanning electron microscope (SEM), since these widths would still yield working devices. After the samples were loaded, the chamber was evacuated until an initial pressure of below $1.7 \cdot 10^{-5}$ mbar was reached to minimize contaminants. The carrier, on which the samples are mounted, was cooled to maintain a temperature of 25 °C throughout the process with the help of 10 sccm cold helium in a heated backing chuck. The bias or acceleration voltage ($V_{DC}$) increases as a function of the radio frequency (RF) power or ion energy and decreases as a function of ICP power or plasma density. The RF power is responsible for a more physical etching because of the increase of ion energy, whereas the ICP power is, in turn, more responsible for a chemical etching because it increases the concentration of free radicals. While the plasma contains highly reactive species, increasing its density is not sufficient to overcome the bond strength of GaN. Since we were interested in minimizing the lateral damage rather than optimizing the etch speed, the forward power, RF power and $V_{DC}$ needed to be kept close to the etching threshold while optimizing the ICP power for minimum pillar or pit formation, which occurs since defects etch with a different speed than the surrounding material. The $BCl_3/Cl_2$ gas mixture and pressure were optimized for maximized etch rate.[118]

Focused ion beam (FIB) was used to mill pre-characterized ICP-RIE samples to gain more information for the optimization of sample gate widths from a single sample. Two milling areas of 19×15 $\mu m^2$ were used in deposition mode on each side of the structure. The areas were milled with a Ga source at 10 pA for 1 s each. It was necessary to use the lowest settings of 1s and 10 pA to be comparable with ICP-RIE. We note that FIB can perform milling currents lower than 1 pA, but charging effects made it too difficult to retain a sharp enough focus to create reliable structures.

## Contacts

The samples were cleaned in accordance to the previous protocol, and the oxide was stripped from the surface using an ammonium solution. Then, lithographically defined ohmic contacts were formed by evaporation of between 50 and 200 Å of Ti (200 Å being optimum) followed by 400 to 800 Å of Al (enough to fully cover the Ti layer even after

intermixing). The oxidation of this layer causes the contacts to degrade, which is a problem since the employed thermal evaporator is limited to two metals in its standard configuration. However, a system modification allowed for the direct evaporation of three metals, at continuous pressures lower than $10^{-6}$ mbar, and 200/800/100/900 Å stacks of Ti/Al/Ti/Au were used with an optional additional Au layer evaporated at 20 ° on a rotating holder. The samples were then annealed in a specially built oven for this project, consisting of a CF-100 UHV chamber connected to a turbo/scroll pump combination. The pressures were measured with a cold cathode and a thermocouple for the chamber and fore-line, respectively. A needle valve connected to ultrapure $N_2$ for variable annealing pressures and a valve for normal $N_2$ purging, were installed together with the corresponding over-pressure valve. A "Boralectric" heating element (Tectra, Germany) with a type *k* thermocouple inserted inside and surrounded by a heat shield was installed into the center of the chamber and regulated by a PID controller (HC3500, Tectra, Germany). The system was rinsed several times by closing the fore-line valve after the scroll pump was turned on, and refilling the chamber with $N_2$. The chamber was then pumped down to a pressure around $10^{-7}$ mbar and adjusted back to $10^{-4}$ with ultrapure $N_2$ under a throttled pump opening. A 20 s ramp brought the heater up to 750 °C where it was held for a total annealing time of 2 min. The ultrapure $N_2$ was turned off once the heater was below 300 °C, after which it was left to cool under vacuum. The samples where cleaned once again and, if applicable, isolating gate contacts were made by lithographically defined deposition of a 10 nm sticking layer of Ti and 70 nm of Au on a 100 nm thick sputtered $SiO_2$ film.

## Packaging

SGHEMT devices were cleaned, mounted to a chip carrier, and wired by Au bonding. The SGHEMTs source and drain contacts were electrically isolated with a two-component epoxy-based glue. This was done in several layers with a 150 °C heating step in-between each layer, allowing the glue to relax before quickly curing. (Bio)molecularly modified SGHEMTs were contacted by Au bonding, and then a single layer of cyanoacrylate-based Si glue was applied to isolate the source and drain wiring.

## 2.3 (Bio)Molecular Functionalization

In **Chapter 4**, GaN and SiC surfaces are functionalized with (bio)molecules. Here, the protocols used to achieve these hybrid (bio)molecular/semiconductor interfaces are presented.

### Silanization

To functionalize the surface of a sample via silanization, one of the two molecules octadecyltrimethoxysilane (ODTMS) or aminopropyltriethoxysilane (APTES) were used to form SAMs of octadecylsilane (ODS) or aminopropylsilane (APS) as presented below and depicted in **Figure 2a** and **b**.

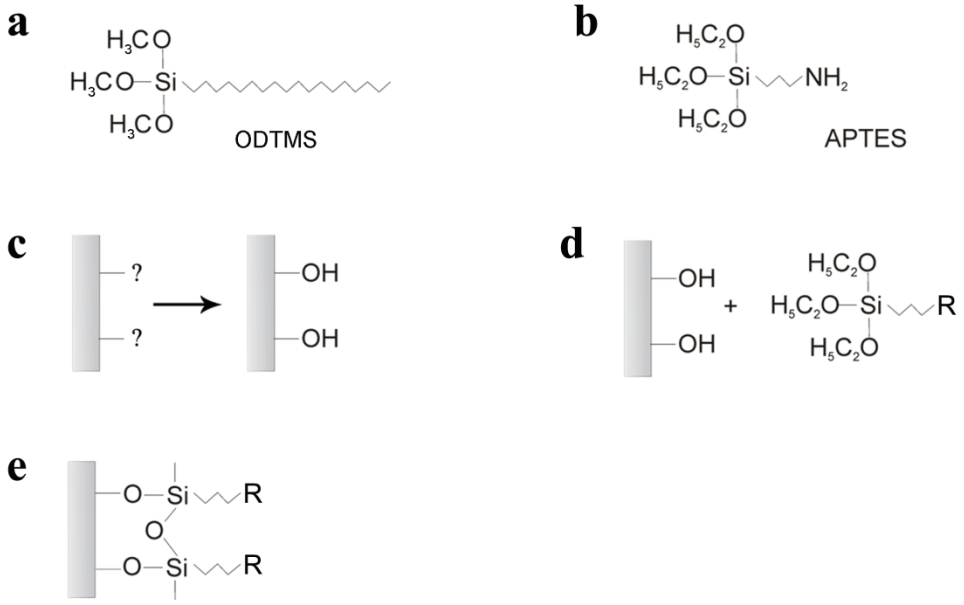


**Figure 2 | Illustration of Surface Modification Through the Silanization Process. a)** The silanization molecule octadecyltrimethoxysilane (ODTMS). **b)** The silanization molecule aminopropyltriethoxysilane (APTES). **c)** The as-grown samples were treated to form a uniform hydroxylated surface as described in the text. **d)** The silanization molecule is introduced into a toluene solution containing the hydroxylated surface. **e)** The silanization molecule reacts to form a SAM with a Si-O-Si cross-linked interfacial network on the surface.

In order to functionalize the surface with the aforementioned molecules, the sample surfaces need to be clean and hydroxyl-terminated as shown in **Figure 2c**. This preparation was performed by ultrasonic cleaning at room temperature in deionized water

(18 MΩ/cm, Millipore), acetone and methanol for 10 min each step. OH-terminated GaN was achieved by treating the sample for 10 min in hot sulfuric acid solution by mixing 3:1 $H_2SO_4$:$H_2O_2$, then it was rinsed in hot deionized water and dried with $N_2$ gas, followed by 10 min in oxygen plasma (Technics Plasma 100-E, operated at 200 W with an oxygen pressure of 1.4 mbar). In contrast, OH-terminated SiC was achieved by performing the following procedure twice in succession; 5 min oxygen plasma treatment followed by etching for 5 min in 5% hydrofluoric acid (HF).[119–121] The samples were then placed over night (12h) in vacuum or, alternatively, in an inert-gas glove box. In the next steps, special precautions were taken to keep the sample and the entire process environment as dry as possible. This precaution makes the process more reproducible since the necessary water to activate the methoxysilane to silanol groups is present on an ambient sample's hydrophilic surface. The lack of water in the surrounding stops the chemicals from premature degradation.

The formation of self-assembled ODS layers on OH-terminated surfaces, **Figure 2d**, was performed by placing the samples into 120 ml of dry toluene that was stirred over molecular sieves and adding 6 ml ODTMS and 0.6 ml of butylamine and sealed into a glass-lidded beaker with Parafilm.[15,16] This container was kept at 14 °C for 150 min (Haake CH thermostat with remote thermometer) under ultrasonic agitation. When completed, the ultrasound was turned off and the samples were left for an additional hour in their cooled state. The silanization chemical, ODTMS, and the reaction catalyst, butylamine, were both acclimatized to room temperature before use, but the solvent toluene remained at refrigerated temperatures for as long as possible.

Alternatively, the formation of self-assembled APS layers from APTES on OH-terminated surfaces (**Figure 2d)** was performed by immediately placing the clean samples into 20 ml of the solvent toluene containing 94 µl of the salinization chemical APTES, both of which were heated to room temperature before use. The lid was then properly sealed onto the beaker with Parafilm and placed into an ultrasonic bath for three intervals of 15 min with and without agitation.

To gain a self-assembled sub-monolayer as depicted in **Figure 2e**, the samples were thoroughly cleaned to remove any physisorbed molecules by rinsing in toluene, drying

with $N_2$ gas, and then placing them into a new beaker with fresh toluene and running them in the ultrasonic bath for 15 min and drying once again with $N_2$ gas. This step was repeated with methanol. Then the samples were placed into a solution of 10 ml deionized water and 3.4 µl of acetic acid and treated for 30 min in the ultrasonic bath at full intensity. As a final step, the samples were cleaned in the ultrasonic bath at full intensity with deionized water for 15 min, followed by rinsing in deionized water and drying them with $N_2$ gas.

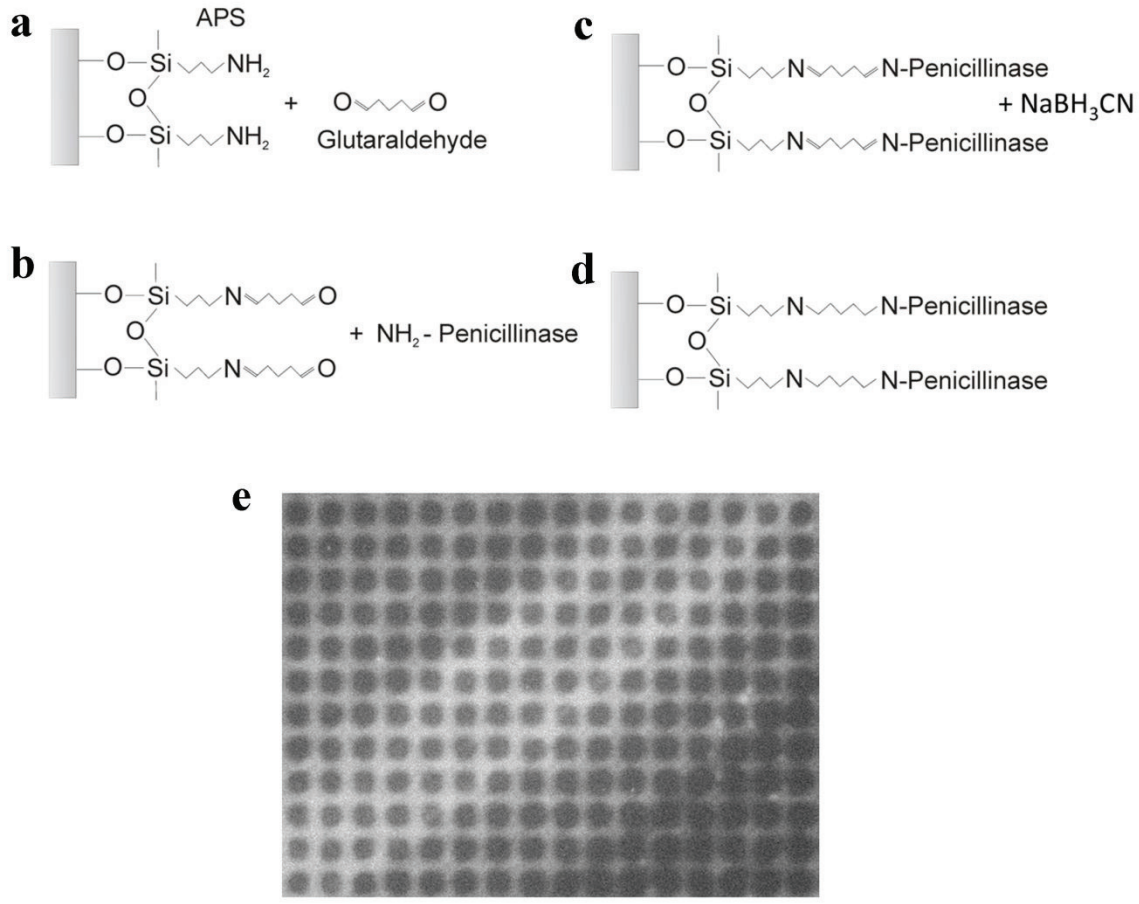


**Figure 3 | Illustration of the APS Enzyme Immobilization Process. a)** Glutaraldehyde is added as a cross-linker since its double-bound oxygen termination at both ends reacts with amino groups. **b)** With the cross-linker in place, any amino-terminated bio-molecule can be immobilized onto the surface. **c)** The remaining double-bonds of the cross-linker are unstable, so reductive amination of imines (C=N) to secondary amines (C–N) in the presence of sodium cyanoborohydride ($NaBH_3CN$) stabilizes the water-sensitive Schiff base bonds. **d)** The resulting covalently bound enzymes. **e)** Fluorescence image of Alexa Fluor 488 penicillinase conjugates selectively immobilized on functionalized GaN surfaces (bright areas). The pattern size is 4×4 $\mu m^2$.

Covalent immobilization of penicillinase from bacillus cereus was carried out by sodium cyanoborohydride-stabilized amino-glutaraldehyde Schiff base bonds on APS monolayer modified GaN gate areas[15,107] using the following procedure. If patterning is desired, the sample is exposed with an exposure length of 999 s to UV light through a standard chromium/quartz shadow mask using a mask aligner. This ensures that the APTES molecules can no longer bind to cross-linker molecules in regions where the sample was exposed. In order to attach amino-terminated molecules to the amino-terminated surface, a symmetrical cross-linker molecule was used, as depicted in **Figure 3a**. This was achieved by placing the samples into a beaker with 20 ml water, and adding 74 µl of the cross-linker glutaraldehyde. The lid was once again sealed onto the beaker with Parafilm and left for 1 h at room temperature or for approximately 24 h at 4 °C. Since glutaraldehyde is very reactive, the samples were quickly rinsed with deionized water, dried with $N_2$ gas, and the following step to immobilize the enzymes onto the cross-linker, as shown in **Figure 3b**, was performed immediately. The samples were placed into a crystallization beaker and a droplet of diluted 20 µg/ml enzymes with a prepared 10 mM solution of phosphate-buffered saline (PBS) solution containing 50 mM of NaCl was placed onto the sample. If the enzymes were labeled, the crystallization beaker was covered with aluminum foil to prohibit photo-bleaching and allowed to stand for 1h without drying. The samples were then rinsed several times with water and PBS solution and dried with $N_2$ gas. After this, the samples were placed into an Eppendorf tube with PBS solution and slowly agitated with a tube mixer for 1h, then rinsed and stored (at 4°C) in buffer. As the generated Schiff-base linkage tends to hydrolyze in humid environments, the coupling is strengthened with a PBS solution containing cyanoborohydride ($NaCNBH_3$) (C4187, Sigma), as shown in **Figure 3c**. The presence of fluorescence labeled penicillinase after covalent immobilization (**Figure 3d)** was verified by fluorescence microscopy and is shown as the bright mesh in **Figure 3e**.[107] Confirmation of the intermediate steps of this process was accomplished by X-ray photoelectron spectroscopy, Fourier transform infrared spectroscopy and static water contact angle analysis, which is not shown here.[15]

### Self-Initiated Photografting and Photopolymerization

Self-initiated photografting and photopolymerization (SIPGP) of N,N-dimethyl-aminoethyl methacrylate (DMAEMA) was performed according to known protocols.[122] Freshly prepared SGHEMTs were added to approximately 1 ml of freshly distilled and degassed DMAEMA. Polymerization was performed for 2.5 h under irradiation with 350 nm UV light with a total power density of approximately 5 $mW/cm^2$ at room temperature. After polymerization, the samples were removed from the reaction solution and immediately rinsed with ethanol. To ensure that only chemically grafted polymers remained on the surface, all substrates were additionally cleaned by ultrasonication for 5 min in the same solvent, followed by ultrasonication in ethyl acetate and ethanol for 5 min each.

### Drop Coating

Physisorbed penicillinase multilayers were prepared by drop coating. Here, a droplet of 20 µg/ml of enzymes was deposited directly onto the sample and allowed to dry.

Ultra-pure fluorescent proteins, provided by the Max-Plank-Institute for Neurobiology, were formed into physisorbed multilayers by drop coating. Here, a droplet of diluted proteins was placed directly onto a samples surface, allowed to dry, then rinsed in fresh PBS buffer with ultrasonic agitation and dried with $N_2$ gas.

## 2.4 Experimental Methods

### Transistor Operation

Unless otherwise noted, the device under test was characterized with a source measurement unit (2400 SourceMeter, Keithley, USA). The device was kept in darkness prior to and during experiments and operated at room temperature with no additional cooling. Source-drain voltages could be set spanning ranges of 200.00 mV to 200.00 V. However, 100 mV or 120 mV were the most commonly used set points. Source-drain currents were recorded spanning ranges 1.00000 µA to 1.00000 A with peak-to-peak

noise at 5 pA to 25 µA for sampling speeds of 0.1 Hz to 10 Hz respectively. For special applications where speed was preferred over resolution, the “measure to general purpose interface bus” (GPIB) maximum single sample rate of 537 S/s to “uninterrupted GPIB” speeds of 1754 S/s were used at the highest possible resolution of 10 nA. Testing the devices prior to mounting them onto chip carriers was achieved with a needle probe station (E26, WSI, TUM).

## UHV Surface Analytics

UHV surface analysis was one of the key techniques used in this work and for this reason a new system was built. The system operates with a combination of turbo molecular pumps and scroll pumps and the pressure read out by a series of thermocouple, cold cathode and Bayard-Alpert pressure gauges. The entire system is run from two uninterruptable Kelvin ground isolation transformer power supplies, providing a sound power environment for the sensitive analyzers. The system consists of four self-contained and gate-valve separable chambers:

- The load lock, shown in **Figure 4a,** allows samples to be introduced into the system while maintaining UHV pressures in the high $10^{-10}$ mbar range within the other chambers.
- The preparation chamber, shown in **Figure 4b**, is equipped with a differentially pumped ion gun (Tectra, Germany), a temperature regulated “Boralectric” heating element (Tectra, Germany), a visible-UV transparent window with variable wavelength light sources mounted on the outside, and a mass-spectrometer (Hiden Analytical, USA). This enables samples to be baked out at up to 1000 °C and their surfaces to be cleaned by an ion beam. Furthermore, analysis by programmed thermal desorption spectroscopy (PTDS), UV desorption spectroscopy (UVDS), and secondary ion mass spectroscopy (SIMS) can also be performed.

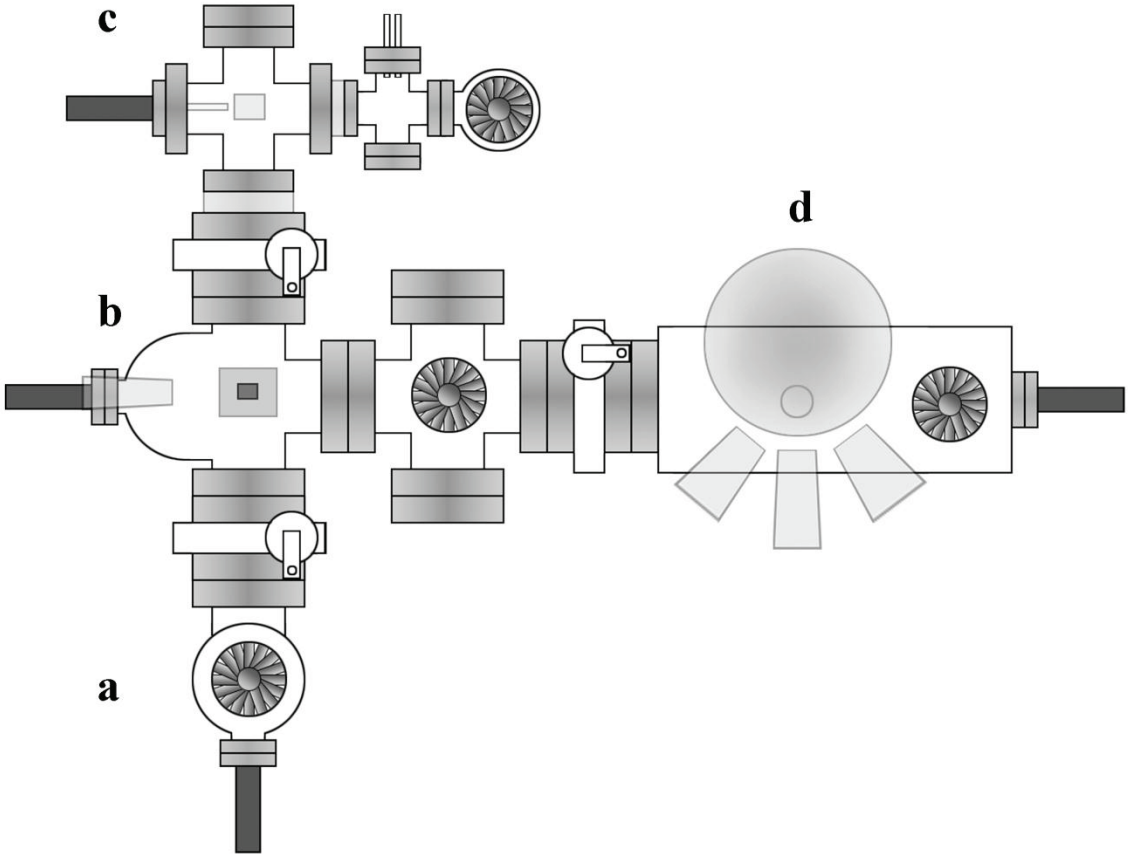


**Figure 4 | Illustration of the UHV Surface Analysis Chamber. a)** The load lock. **b)** The preparation chamber. **c)** The pressurizable chamber. **d)** The electron analyzer chamber.

- The variable pressure chamber, shown in **Figure 4c**, can be flooded from the normal standby pressure of high $10^{-10}$ mbar to 1 atmosphere through UHV gas lines connected to a gas bottle cabinet. The chamber was built with restriction and overpressure valves and is also separated from the rest of the system by glass-separated UHV flanges to electrically isolate the chamber for sensitive measurements. A visible-UV transparent sapphire window with variable wavelength light sources mounted on the outside was top-mounted onto the chamber. The chamber supports a manipulator onto which an oscillating Au reference electrode (Kelvin Probe S Besocke Delta Phi, Jülich, Germany) is mounted, and operated by a controller unit (Kelvin Control 07, Besocke Delta Phi,

Jülich, Germany). Contact potential difference (CPD) and surface photovoltage (SPV) studies were performed with this equipment.

- The electron analyzer chamber shown in **Figure 4d** has a 100 mm radius hemispherical analyzer (Specs), an X-ray source equipped with a dual Al and Mg $K_\alpha$ anodes, a UV light source (Specs), and an electron gun (Specs). This chamber has a typical base pressure of $1 \cdot 10^{-10}$ mbar and can be used for X-ray photoelectron spectroscopy (XPS), UV photoelectron spectroscopy (UPS) and Auger electron spectroscopy (AES).

## Contact Potential Difference

The Kelvin probe method is a nondestructive way to obtain the contact potential difference (CPD) between two materials. It was employed to study the surface photovoltage (SPV) of GaN and SiC. The set-up is part of the previously described UHV surface analytics system, and measurements were performed at low $10^{-10}$ mbar. It consists of:

- A manipulator with an oscillating Au reference electrode
- A sample holder connected to the control unit.
- Sample illumination from, for example, a 250 W Xe lamp through a range of neutral density filters.

When two materials with different work functions are electrically contacted, electrons will flow from the material with the lower work function to the one with the higher work function, until the Femi levels are aligned. If these materials are then brought together to form a capacitor, an equal and opposite charge will appear on each capacitor plate. When the distance between the plates is increased the capacitance decreases and, since the charge remains constant, the voltage must increase in accordance to

$$U = {}^{Q}/_{C} \qquad (1)$$

where C is the capacitance, Q is the charge and U is the voltage. Here, the moving plate is a gold reference electrode attached to a mechanical oscillator. A voltage ramp, $U_r$, is then applied between the sample and gold electrode while measuring the peak to peak value of

the capacitive voltage U. The corresponding linearly interpolated zero value of U corresponds to

$$U_r = -U_{CPD} \qquad (2)$$

where $U_{CPD}$ is the contact potential difference. This set-up was also used to measure the time-dependent photovoltage. Here, a light source was used, together with a specially written program in Labview (National Instruments, USA), to measure the difference between the settled dark CPD value, $U_{CPD}^{d}$, and the saturated illuminated CPD value, $U_{CPD}^{l}$, versus time, giving the surface photovoltage

$$U_{SPV} = U_{CPD}^{l} - U_{CPD}^{d} \qquad (3)$$

## X-ray Photoelectron Spectroscopy

X-ray photoelectron spectroscopy (XPS) is a nondestructive technique and was employed to study the chemical composition of hybrid (bio)molecular/GaN and (bio)molecular/SiC interfaces. The set-up is part of the UHV surface analytics system and measurements were performed at pressures of low $10^{-10}$ mbar. It consists of:

- Al filtered, dual Al and Mg $K_\alpha$ anodes (XR 50, Specs, Germany), operated well above the $K_\alpha$ energy of Al (1487eV) or Mg (1254eV) at 12.5 kV with an emission current of 20 mA .
- An adjustable sample stage with a low-impedance grounding to the analyzer.
- A hemispherical energy analyzer (PHOIBOS 100, Specs, Germany), operated at constant pass energy (40 eV) and variable retardation voltage.

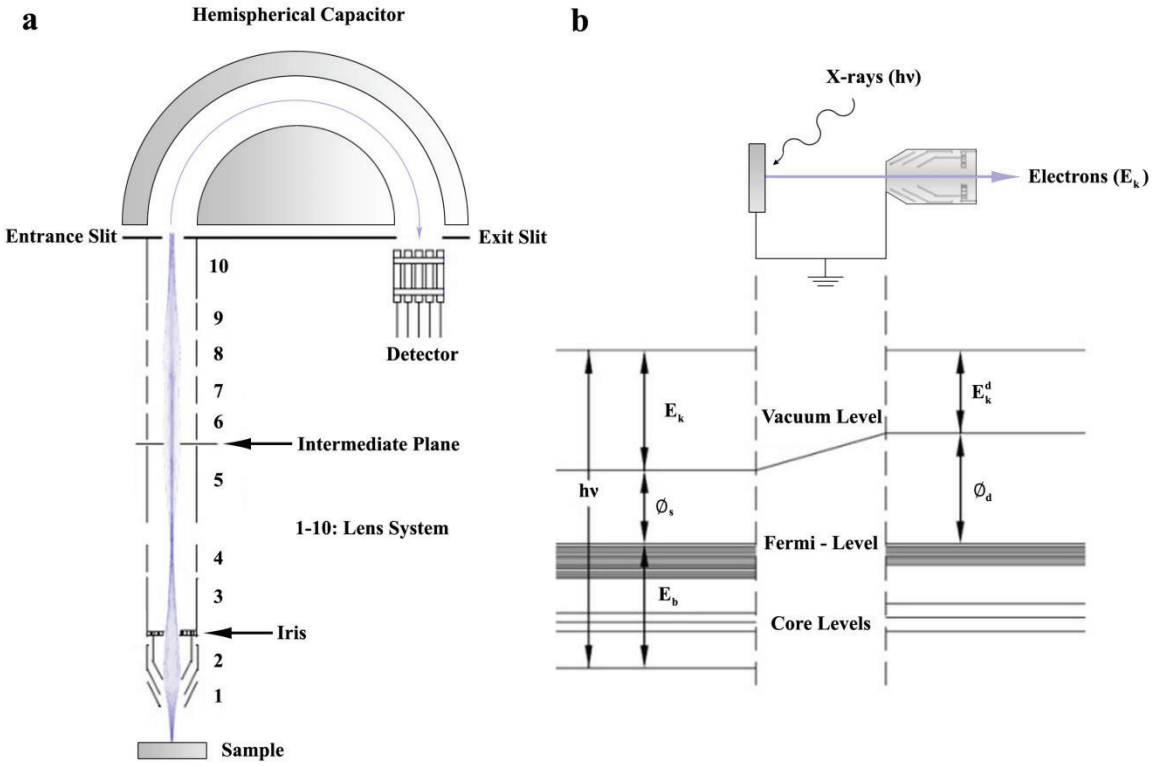


**Figure 5 | Illustration of the Key Points of XPS. a)** A cross section of the electron energy analyzer showing the sample, lens system, hemispherical capacitor and detector. b) Illustration of the band alignment between a sample and the detector with the energies noted as explained in the text. (This picture was adapted from the Specs PHOIBOS 100 manual)

As illustrated in **Figure 5**, the X-ray beam is directed onto the measurement sample where, depending on the samples cross section, it penetrates typically 10 µm to 100 µm into the surface. However, scattering restricts emission of photoelectrons from the sample to the top 20 nm, making this method a surface-sensitive technique. The electrons of interest will be emitted with a kinetic energy, $E_k$, in accordance to the photoelectric effect

$$E_k = h\nu - E_b - \emptyset_s \qquad (4)$$

where $h\nu$ is the photon energy, $E_b$ is the electron binding energy and $\emptyset_s$ is the samples work function. Here, $E_b$ is the value of interest, as it is specific to each individual atomic or molecular electron orbital. To obtain it, the sample must share the analyzers grounding so that the Fermi levels are equal. As the emitted electrons enter the first stage of the analyzer they are focused with a series of ten electrodes into the multimode transfer lens. The analysis spot size can be magnified with the lens system to give a maximum

resolution of 100 µm diameter. There are also a series of obstacles, including an adjustable iris and an intermediate plane, positioned to hinder stray electrons from reaching the detector and increasing the background noise. The lens system has a linear retardation voltage, which is used to change the kinetic energy of the electrons entering the hemisphere. Because of this, its work function must be known through calibration. The hemispherical capacitor adds two additional slits to the previously mentioned series of obstacles, one at the entrance and one at the exit in front of the detector. As the electrons enter the capacitor they are angularly accelerated, which is used to separate electrons with different kinetic energies. Due the symmetry of applying potentials to the inner and outer parts, the work function does not need to be known. Thus, the higher these potentials, the higher the energy resolution at the loss of intensity. Electrons with an exact kinetic energy pass the exit slit, are accelerated, and strike the electron multiplier which consists of a series of secondary emissive plates with pre-calibrated voltages applied to cause a measurable avalanche effect represented as a single count. Since the Fermi level of the sample and detector are considered to be equal

$$E_k + \emptyset_s = E_k^d + \emptyset_d \qquad (5)$$

must hold, where $E_k^d$ is the photoelectron's kinetic energy as seen by the detector and $\emptyset_d$ is the detector's work function. Therefore, the binding energy can be determined from the photoelectron's kinetic energy as follows,

$$E_b = h\nu - E_k^d - \emptyset_d \qquad (6)$$

So, by sweeping the retardation voltage, it is possible to create a binding energy spectrum specific to the composition of the samples surface.

## Desorption Spectroscopy

Thermal and UV desorption spectroscopy are destructive methods and were employed to resolve information about binding energies of (bio)molecules on GaN and and SiC surfaces. The set-up is part of the UHV surface analytics system and measurements were performed at high $10^{-10}$ mbar. It consists of:

- A heating source ("Boralectric" heating element with a HC3500 PID controller, Tectra, Germany) or filtered (254 nm) light from a low pressure Hg lamp for thermal or UV desorption spectroscopy, respectively.
- A quadrupole mass spectrometer (HAL, Hiden Analytical, USA)

The sample is heated with a linear ramp or irradiated with UV light and desorbing molecules cause a partial pressure as a function of ramp time, temperature or irradiation time. As the molecules enter the mass-spectrometer they are converted into positive ions or fragments. This is achieved by electron impact ionization via thermionic emission from a hot filament. The ions are extracted into the mass filter consisting of two pairs of poles each connected to a RF and a DC power source. The molecules travel down the space in between these poles and only ions with a certain mass-to-charge ratio will reach the detector, a Faraday cup, for a given ratio of voltages. Individual molecules can be identified through an ion fragment database.

## Static Water Contact Angle

Static water contact angle (SWCA) determination is a nondestructive technique to assess the hydrophobicity of a surface. It was employed to study the quality of SAMs on hybrid (bio)molecular/GaN and (bio)molecular/SiC interfaces. It consists of:

- A digital camera with a macro lens mounted so that a picture lateral to the surface can be taken.
- The sample with 1.5 µl drops of ultrapure deionized water (>18 MΩ·cm, Millipore) placed on top.

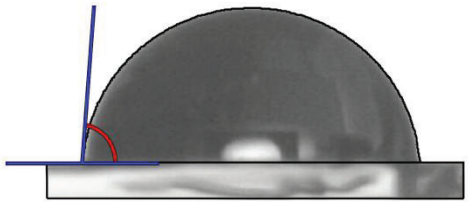

**Figure 6 | Illustration of Static Water Contact Angle Measurement.**

As shown in **Figure 6**, the contact angle between the sample and droplet edge is measured and used to evaluate the degree of hydrophobicity of a sample's surface.

## Attenuated Total-Reflectance Fourier Transform Infrared Spectroscopy

Attenuated total-reflectance Fourier transform infrared spectroscopy (ATR-FTIR) is a nondestructive technique and was employed to study the chemical composition of hybrid (bio)molecular/GaN and (bio)molecular/SiC interfaces. The set-up consists of:

- A commercial evacuated spectrometer (Vertex 70v, Bruker, Germany).
- A MIRacle ATR-unit equipped with a single reflection Ge ATR crystal (Pike Technologies, USA).

In this work, FTIR is used for absorption spectroscopy and is conceptually similar to dispersive absorption spectroscopy, where the absorption of a sample is recorded for monochromatic steps of a light spectrum. FTIR is a less intuitive way to obtain the same information since the amount of polychromatic light absorbed by the sample is measured. Each data point contains the samples absorption for a different combination of known wavelengths, which is achieved with a Michelson interferometer. Here, light is split into two directions with a beam splitter. In the first direction it is reflected back to the splitter with a known fixed distance of the mirror and in the second direction it is reflected back with a mirror at a known adjustable distance. The two beams are recombined with the same beam splitter and the sample absorption to the known interference patterns, calculated from the mirror position, is measured and recombined into a spectrum with a Fourier transform algorithm.

For ATR-FTIR the polychromatic light is passed through a crystal using its total internal reflection property and the detector positioned to measure the exiting light. Here, the detector measures the interaction of the light's evanescent field with the sample's surface when it is pressed onto the crystal with light mechanical pressure, to obtain a good contact. All spectra need to be background-referenced to the clean ATR crystal measured against vacuum, which was done in this work with a resolution of 3 $cm^{-1}$ and with 1200 scans for each measurement.

## X-Ray Reflectivity

X-ray reflectivity (XRR) is a nondestructive technique and was employed, at standard temperature and pressure, to study the thickness of the self-assembled (bio)molecular layers on GaN and SiC surfaces. The set-up was provided by the group of Bert Nickel at the Ludwig-Maximilians-Universität München and consisted of:

- A Mo $K_\alpha$ (17.4 keV) X-ray source.
- An X-ray detector.
- A specular translation stage with sample holder.

This technique measures the reflection of X-rays on a flat surface through a range of angles, where the incident angle is equal to the reflected angle and referred to as the specular angle. Here the deviation from Fresnel reflectivity is used through the extended Fresnel reflectivity equations to provide information on density, thickness and interface roughness of the layer(s).

## Solution Gate Analysis Cell

A measurement and automation system was constructed to regulate SGHEMTs and precisely control their environment with a specially written program in Labview (National Instruments, USA). A schematic diagram of the set-up is shown in **Figure 7**. At the center of the system was a single electrochemical cell consisting of a standard glass-electrode (*p*H/Ion-Meter 781, Metrohm, Switzerland), a Pt counter-electrode, a saturated KCl dual chamber Ag/AgCl reference-electrode, an SGHEMT configured as a working electrode, (Voltalab potentiostat, France), a Pt-1000 temperature sensor, and a top-mounted Teflon stirring unit. The cell was closed from the top by a Teflon cap, which also defined the electrode mounting positions for the inner cell. In most cases, the cell solution consisted of 10 mM HEPES and 0.1 M KCl buffer solution at approximately *p*H 7 and was titrated with buffer solution containing high concentrations of KOH, or HCl.

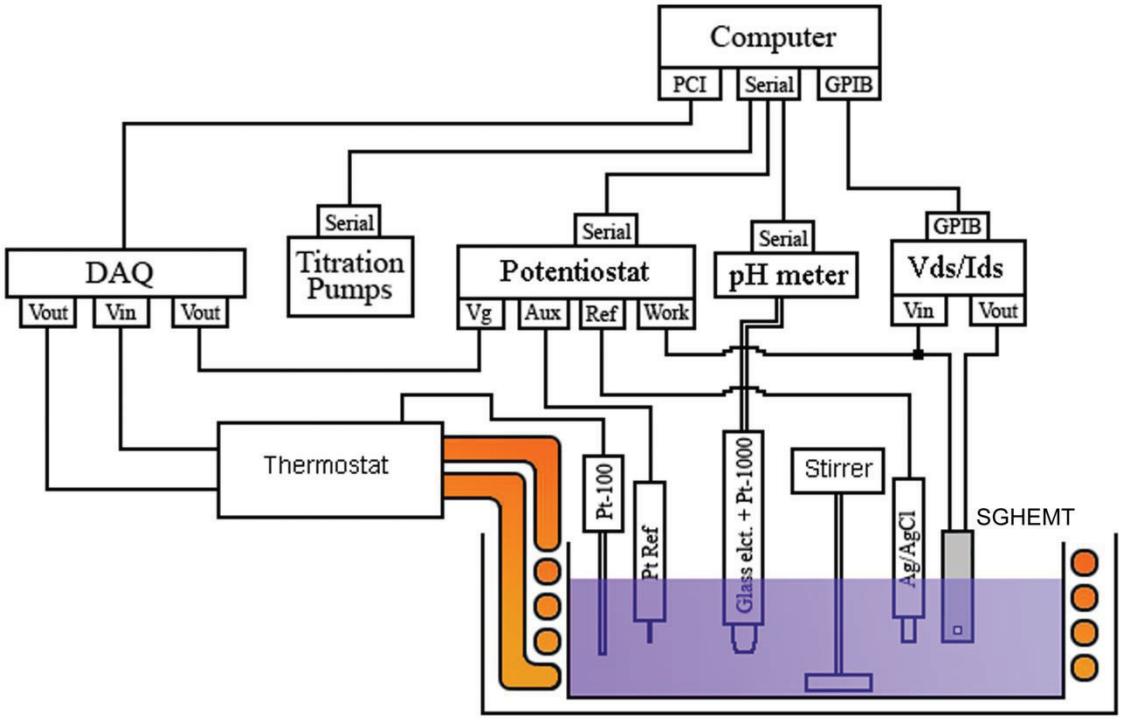


**Figure 7 | The SGHEMT Electrochemical and Environmental Control System.** In the center, the electrochemical cell is depicted and is based on a three-electrode set-up (Pt counter-, Ag/AgCl reference- and SGHEMT working-electrodes).

The solution temperature, read out from the Pt-100 sensor, was regulated by cycling cooling liquid from a thermostat reservoir in-between the double walls of the glass chamber. Computer-controlled milliliter to microliter titration pumps (Reglo digital, Ismatec, Germany) were capable of titrating and thereby regulating the concentration of eight different solutions simultaneously. This segment was housed inside a grounded metal box, which functioned both as a way of blocking out light and as a Faraday cage. For optimum measurement conditions, the potentiostat held the reference electrode at 0 V via the counter electrode. The reference electrode was placed as close to the HEMT device as possible. The source-drain voltage of the transistor was controlled by a semi floating source meter and the potential difference between drain and the solution was set by the work output of the potentiostat. This source measurement unit contained the integrated components from a FPGA (National Instruments, USA), source measurement unit (2400 SourceMeter, Keithley, USA), and a 5 Hz to 13 MHz parameter analyzer (4192A, HP, USA), making it capable of simultaneously measuring or regulating the

source-drain voltage, source-drain current, gate-solution voltage, gate-solution current, gate-solution impedance, and/or gate-solution capacitance.

At the center of the code, responsible for communicating with the aforementioned equipment, was the SGHEMT control algorithm. A set-point for the device could be found by a calibration routine that created a matrix of data by recording, for example, the source-drain current, while sweeping the gate-drain voltage at different source-drain voltages. This could be performed in half or full cycle intervals, and the matrix would contain readings from any or all of the previously mentioned units. The program could then be run statically, or, by selecting an active variable and a variable to be kept constant, with a control algorithm. The most commonly used variant in this work was to keep the source-drain current constant by varying the gate-drain voltage at a constant source-drain voltage. The algorithm works on the basis of a proportional, integral and derivative (PID) analysis of one measurement value. In this case the PID control was used to provide a constant value of transconductance by modulating the gate-source voltage. This routine is contained within an outer watchdog circuit consisting of predefined boundary conditions and a maximum linear slope of change running a $3^{rd}$ degree polynomial, which introduces a fast response for large changes, and effectively switches itself off at the set-point value due to the absence of self-oscillation around the zero point. Furthermore, the thermostat and pumps can be implemented into a running program. A standard deviation or time value from the main algorithm can trigger the next cell temperature step or titration in their respective loops. Titrations can be performed by constant volume or previously calibrated constant *p*H step titration.

## Photo-Bleaching

Photo-bleaching curves of fluorescent proteins were achieved by using a fluorescence microscope (Carl-Zeiss, Germany), which allows the illumination of a sample through a system of filters at one wavelength range and the measurement of its fluorescence at a second wavelength range without spectral interference. The degradation of the proteins emission was recorded by a high-speed black and white Hamamatsu camera. Each frame of the movie was converted into average intensity from the brightness information with a specially written program in Labview (National Instruments, USA).

## Bremsstrahlung

Several Bremsstrahlung sources were used for controlled irradiation of HEMT devices for characterization purposes including attenuation measurements on a human phantom and X-ray-induced fluorescence measurements.

For X-ray radiation at energies above an acceleration voltage of 50 kV, a medical X-ray system with a 4 mm Al filter (Stabilipan TR300f, Siemens, Germany) was provided by the Helmholtz Zentrum München. Reference air kerma measurements, the energy absorbed per kg of air, were recorded at the tube exit with a transmission ionization chamber (Diamentor 34015, PTW, Germany) connected to a dose area product meter (Diamentor M4, PTW, Germany). The system had a resolution of 0.01 $\mu Gy \cdot m^2$. For reference measurements, where a more local position was required, a freely mounted 1 $cm^3$ ionization chamber (23331, PTW, Germany) was used and operated with its corresponding controller (Dosimentor DL4 dosimeter, PTW, Germany).

Low dose X-ray radiation at energies below an acceleration voltage of 50 kV were performed with a technical X-ray system (MG 325 with MCN 323 tube, Philips Industrial X-rays, Hamburg, Germany) in the IAEA/WHO Secondary Standard Dosimetry Laboratory (Helmholtz Zentrum München). Samples were irradiated on a calibration bench under monitor control (TM 786, PTW, Germany) with an electrometer (IQ4, PTW, Germany) using an ISO narrow series radiation quality of 40 kV with 0.21 mm Cu and 4.0 mm Al filtration and mean photon energy of 33 keV. Air kerma doses were measured with a calibrated 30 $cm^3$ ionization chamber (TM 23361, PTW, Germany) and an electrometer (Unidos, PTW, Germany) with appropriate corrections for radiation quality, ambient pressure and temperature.

Attenuation measurements were performed with 2.5 cm thick slices of a radiation therapy phantom (Alderson, RSD, USA) perpendicularly orientated to the beam direction. The phantom consists of human bone material embedded in an artificial matrix which is equivalent to human soft tissue. For imaging purposes, a device was fixed to a custom-built computer-controlled two-dimensional translation stage. A specially written program in Labview (National Instruments, USA) controlled the translation stage stepper motor

positions and read out the device current from the source measurement unit (2400 SourceMeter, Keithley, USA). By these means two-dimensional attenuated current maps of a human phantom wrist segment were realized.

X-ray induced fluorescence measurements of the of AlGaN/GaN heterostructures was performed by recording the fluorescence intensity with a low-light imaging camera (Luca S 658M, Andor Technology, Belfast, U.K.) at different dose-rates. The samples were irradiated for 30 s at each adjusted dose rate, after which a total of 50 pictures were taken within 3 s under constant X-ray irradiation. The average intensity within the defined region of interest from the 50 pictures was calculated for each dose rate.

## Tandem Accelerator

Particle-induced current measurements were performed using focused 20 MeV protons of the ion microprobe SNAKE at the Maier-Leibnitz-Laboratorium tandem accelerator.[123–125] By using a superconducting lens, the proton beam could be focused to a diameter of less than 1 µm (full width at half maximum) in air. Due to the geometry used for irradiation in this work the beam spot size at the sample was approximately a few microns in diameter. The beam can be scanned by an electrostatic deflection unit over a 1×1 $mm^2$ area. The particle flux was adjusted using a micro slit system in the beam line and was measured using a photomultiplier tube covered by a BC-400 plastic scintillator positioned behind the device.

## Synchrotron

X-ray irradiation measurements were performed at the µSpot Beamline at the BESSY II synchrotron of the Helmholtz Zentrum Berlin during operation in single bunch mode, which yielded beam currents in the range of 10 to 20 mA. All measurements were performed with monochromatized 1-20 keV photons which were focused to a spot size of approximately 3 µm in diameter through a fixed silica capillary. Unless otherwise indicated, 7 keV photons are presented from this energy range. The photon flux was determined using a 5 cm long intensity-monitoring ionization chamber (IC Plus, FMB Oxford, U.K.) with a 10 mm electrode spacing. The chamber was placed before the capillary along with a calibrated correction for the transmission loss through the capillary.

Photocurrent mapping was achieved by translating the sample in front of the capillary. The photon flux was adjusted using a combination of an aperture and a series of Al filters.

# 3 The AlGaN/GaN Material System

In this chapter, we introduce many of the concepts used in this thesis, such as the material system, device characteristics, solution gate operation, and high energy particle cross-sections. Furthermore, we demonstrate new possibilities to significantly improve *p*H measurements through the use of high sensitivity devices.

## 3.1 Overview of the Material Properties

In this thesis, we study thin films of gallium-face (0001) GaN and GaN/AlGaN/GaN heterostructures grown on sapphire.[21] Gallium forms a tetrahedral bond structure to nitrogen with a theoretical $sp^3$- hybridization angle of 109.47°, as depicted in **Figure 8a**. When these tetrahedral blocks are stacked together, they can form either the binary cubic zinc-blend or the binary hexagonal wurtzite crystal structure. Since it is the thermodynamically stable phase and was solely used in this work, we will exclusively discuss the wurtzite structure whose stacking sequence is illustrated in **Figure 8b**. The $sp^3$-hybridization defines the "ideal" wurtzite lattice. Here, the dipolar bonds of a symmetrical binary system are geometrically balance out, so that the net total polarity of the molecule is zero. For this reason, we can build a wurtzite structure without a macroscopic polarization, even though Ga and N have very different electro-negativities of 1.81 and 3.04 Pauling units, respectively. However, as soon as we consider the lattice as a finite entity, other contributions to the total crystal energy such as the surface charge become important. Indeed, the abrupt termination of the lattice breaks the tetrahedral symmetry at the surfaces, causing the crystal to distort as the charge throughout the structure compensates for the boundaries. Locally, this leads to the effect that the barycenter of positive and negative charge of the wurtzite structure no longer coincides. Thus, both the bond angles and lengths will minutely distort as the crystal relaxes into a new point of equilibrium and the tetrahedral symmetry breaks down, "spontaneously" polarizing the crystal at zero strain.

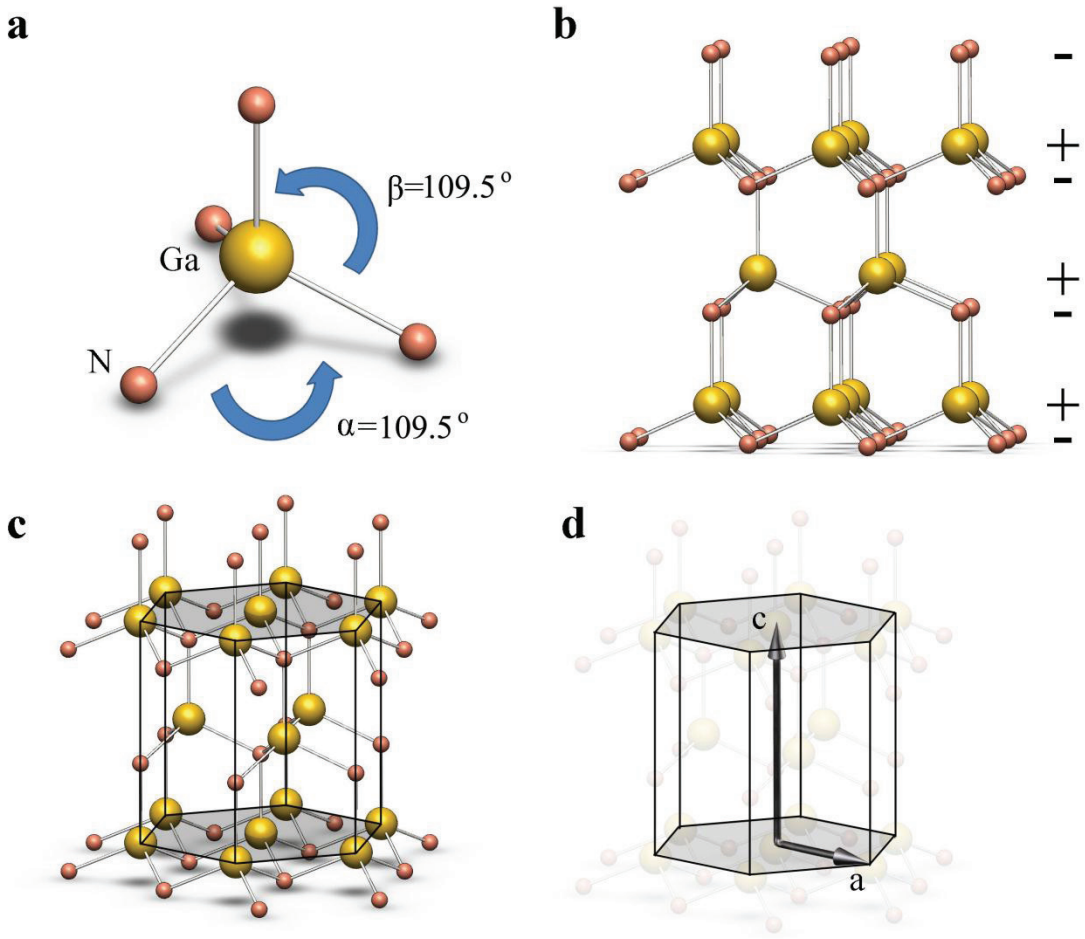


**Figure 8 | Crystal Structure of GaN. a)** Gallium forms a tetrahedral bond structure to nitrogen with a theoretical $sp^3$- hybridization angle of $\alpha = \beta = 109.47°$. **b)** As the tetrahedrons are assembled, the difference in electronegativity between Ga and N creates a periodic dipole throughout the lattice. **c)** The thermodynamically stable form of GaN is a binary hexagonal crystal structure, referred to as a wurtzite crystal, where the hexagonal cell is defined with unit vectors *a* and *c,* as depicted in **d)**.

Remarkably, this crystal relaxation, best realized by studying the wurtzite unit cell depicted in **Figure 8c**, only impacts the *c* axis of the unit cell by pushing the three lower nitrogen atoms, decreasing $\alpha$ and increasing $\beta$, while also decreasing the *c/a* ratio (**Figure 8d**) at room temperature, leaving the hexagonal symmetry intact. This makes the non-centrosymmetric wurtzite structure the highest symmetry compatible with the existence of spontaneous polarization. It is accepted that, if a crystal possesses pyroelectric characteristics, it will also be piezoelectric, where, in this case, tensile strain will add to the spontaneous polarization. While changing the degree of polarization by external

pressure can be used in itself for sensing applications, only the effects induced by creating additional polarization through growth-induced strain are of interest here.

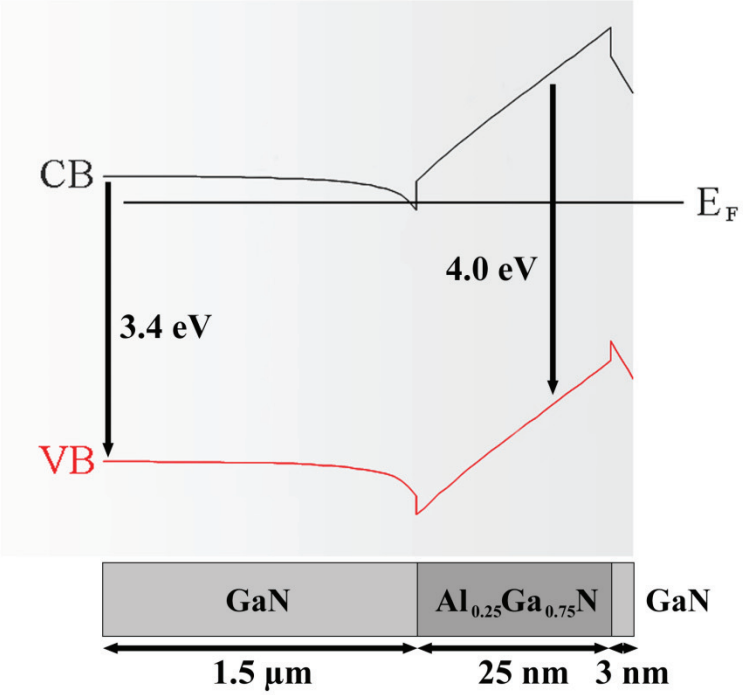


**Figure 9 | Diagram of the Heterostructure Band-Alignment.** A nextnano[3] model of the GaN/$Al_{0.25}Ga_{0.75}N$/GaN heterostructure band alignment, with the conduction (CB) and valence band (VB) edges shown relative to the Fermi level ($E_F$).

It is common practice to form ternary alloys like $Al_xGa_{1-x}N$ and $In_xGa_{1-x}N$, where *x* has a value between 0 and 1. This work only encompasses thin layers of $Al_xGa_{1-x}N$ (≈ 20 nm) grown on GaN, which are under increasing tensile strain with increasing Al content, since both *c* and *a* are smaller than for GaN, correspondingly increasing the polarization. Since this is an *n*-type system, the bound positive polarization-induced interface charges, created at the Ga-face polarity GaN/AlGaN heterojunction, are screened by electrons, causing the formation of a 2DEG.[126,127] To further illustrate this, the conduction (CB) and valence band (VB) edges were modeled (nextnano[3], Germany) as shown in **Figure 9**. Here, the positive interface charge leads to a downward band bending that forces the conduction-band below the Fermi level ($E_F$) at the heterointerface. Extremely high carrier mobilities arise from the spatial separation between the electrons in the two-dimensional channel and, for example, the ionized donor atoms and impurity centers, thereby reducing the ionized impurity scattering.[128] The 2DEG densities in such channels are epitaxially

tunable over a large range from $10^{12}$ to $3\times10^{13}$ $cm^{-2}$, and typical low-field mobilities achieved at room temperature are in the range of 1500 $cm^2/V\cdot s$.

## 3.2 Optimization and Characteristics of High Electron Mobility Transistors

Devices can be created from the previously described heterostructures as illustrated in **Figure 10**. Here, active channel regions can be defined by, for example, ICP-RIE of hard-baked lithographically patterned surfaces with chlorine gases.[129] The goal is to etch down 100 nm, removing the 2DEG that is usually located 30 nm below the surface and the surrounding conductive layers, so that only the highly resistive GaN:C buffer layer remains and the 2DEG is left intact under the thicker, somewhat faster etching, protective photoresist.

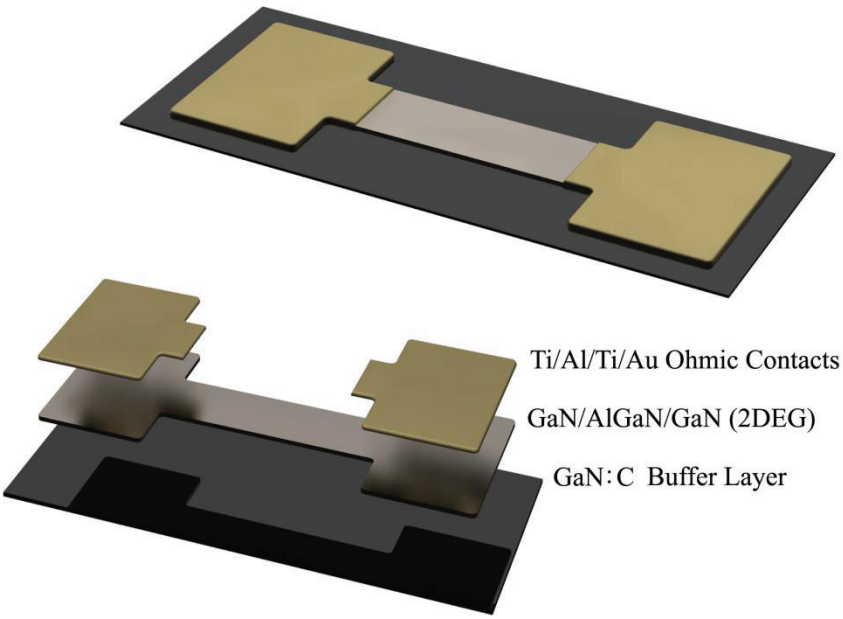


**Figure 10 | Illustration of a High Electron Mobility Transistor.** A 3D illustration demonstrating a typical configuration for a device processed from a heterostructure wafer. The exploded view illustrates the highly resistive carbon-compensated GaN thin-film grown on a sapphire substrate (GaN:C Buffer Layer), the 2DEG heterostructure with GaN capping layer that is grown on top (GaN/AlGaN/GaN (2DEG)), and the metal sandwich structure used to create ohmic contacts to the 2DEG (Ti/Al/Ti/Au Ohmic Contacts).

The mesa structure can then be contacted. Forming ohmic contacts to GaN has been a topic of considerable interest.[130] In this work we use the Ti/Al system, which is believed to become ohmic by forming an *n*-type subsurface through the depletion of nitrogen from GaN during annealing at high temperatures, underneath a thin TiN or $AlTi_2N$ layer at the GaN/metal interface.[131] The resulting strong band-bending is enough to allow an ohmic behavior through the tunneling of carriers.[132] The oxidation of this layer and also the direct application of a protective Au layer, due to diffusion into the Ti/Al layer, causes the contacts to degrade. A metal with a high melting point is often used here to block this diffusion,[133] and as Ti is reported to work well as a barrier material,[134] Ti/Al/Ti/Au contacts were used throughout this work. Furthermore, $SiO_2$/Ti/Au was used to electrically gate the devices, where Ti is used as a sticking layer.

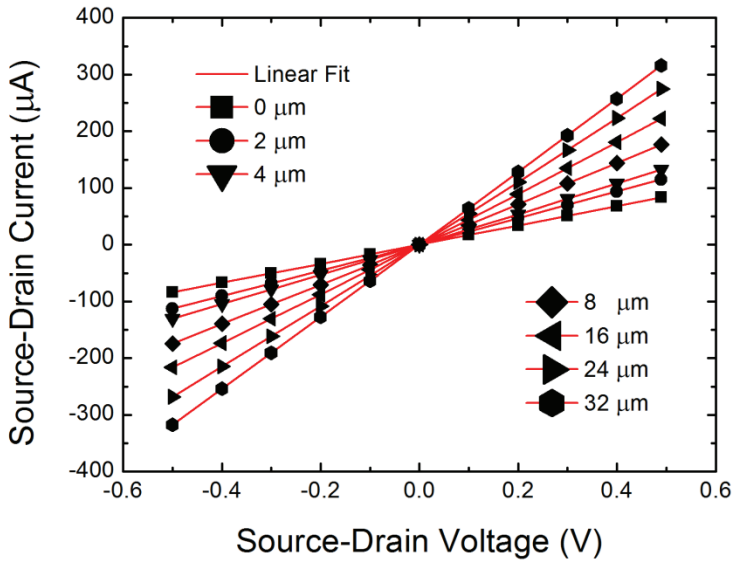


**Figure 11 | Cyclic Source-Drain Current-Voltage Characteristics.** The partial data set of cyclic source-drain current as a function of source-drain voltage for devices with varying gate widths.

There have been numerous accounts of how to achieve GaN-based nano-structures through growth[135–137] with a 2DEG present.[138] However, we focus on achieving small heterostructure devices by etching, and since it was recently shown to be successful down to sizes of tens of nanometers with the 2DEG kept intact,[139,140] this technique offers a good outlook for future nano-scale devices. Here, various shadow masks were created, initially with arrays of 40 structures individually fitting on a 5×5 $mm^2$ sample. Each array contained 24 contacted line and 16 transmission line method (TLM) structures. Together,

these arrays covered lengths between 4 µm and 2048 µm, and widths between 1 µm and 1024 µm in multiple steps of two.

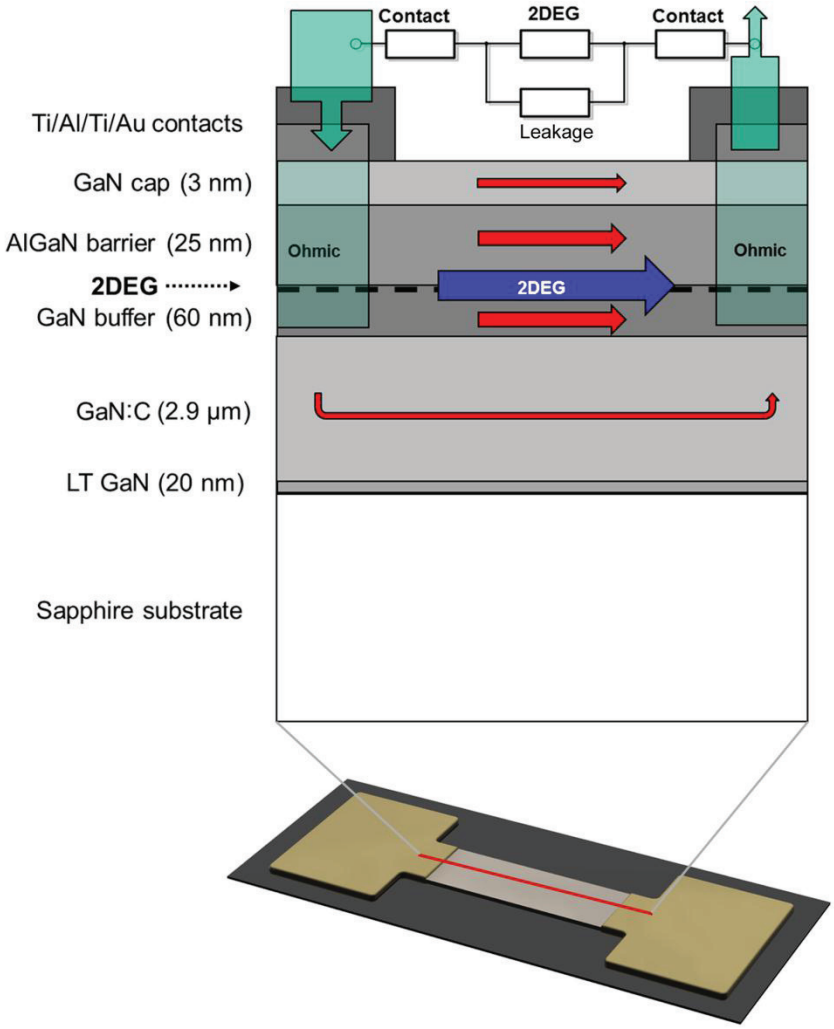


**Figure 12 | Cross Section and Conduction Path of the Heterostructure Layers.** The extra conduction paths that are responsible for the leakage currents are shown with red arrows.

Once the devices were created, cyclic measurements of the source-drain current as a function of source-drain voltage were performed. As an electric potential is applied across the source and drain contacts the electrostatic force causes the carriers to first accelerate and then reach a constant velocity due to scattering with impurities and lattice vibrations. As shown in **Figure 11**, the change in current as a function of applied potential is mostly a linear, or ohmic, relationship. However, as the carrier drift velocity increases, the kinetic energy passes the optical phonon energy, upon which the subsequent phonon

emission causes an abrupt saturation of the velocity. For the structures discussed in this thesis this effect occurs at source-drain voltages between 10 and 100 V, depending on the device geometry. Typical results between ±500 mV are shown in **Figure 11**. The devices exhibited ohmic behavior, and for each source-drain current-voltage data-set, the resistance and conductance were extracted from linear regression. As can be seen in **Figure 11**, these devices are characterized by large leakage currents, whereas an ideal zero gate width device should have an infinite resistance. The extra conduction paths responsible for this leakage current are illustrated in a cross-section of the stack structure in **Figure 12**. Since the current passing through the mesa is the sum of the currents from all of the layers, the background current depends on how far down the structure was etched and the width of the contacts in relation to the width of the mesa. In the case when the contacts are much wider than the mesa, which was the only reproducible way to contact structures of this size, the background current can become dominant and needs to be corrected for, together with the finite contact resistance of the ungated area between source and drain.

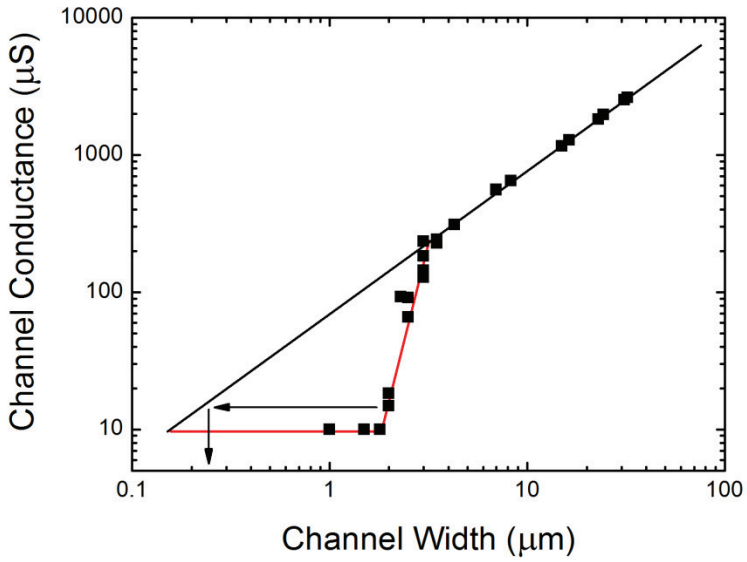


**Figure 13 | Breakdown of Channel Conduction vs. Channel Width.** A non-linearity can be seen in the conductance vs. channel width plot, showing a fast decrease in the conductance, indicating that damage starts to dominate channel widths smaller than 3 μm.

The dependence of the source-drain conductance verses channel width is plotted in **Figure 13**. As can be seen, an abrupt decrease of the conductance occurs for small

widths. This indicates that the 2DEG starts too depleted because of etching damage at an approximate width of 3 µm and is totally depleted at approximately 2 µm. If the last values of channel widths with a measurable conductance are projected on the linear extrapolation, a value of the smallest 2DEG width that can be obtained with this technique can be estimated to 250 ±100 nm for a 2 µm physical channel width. However, the smallest devices used in this work were wider than 10 µm to avoid the problem of lateral collapse.

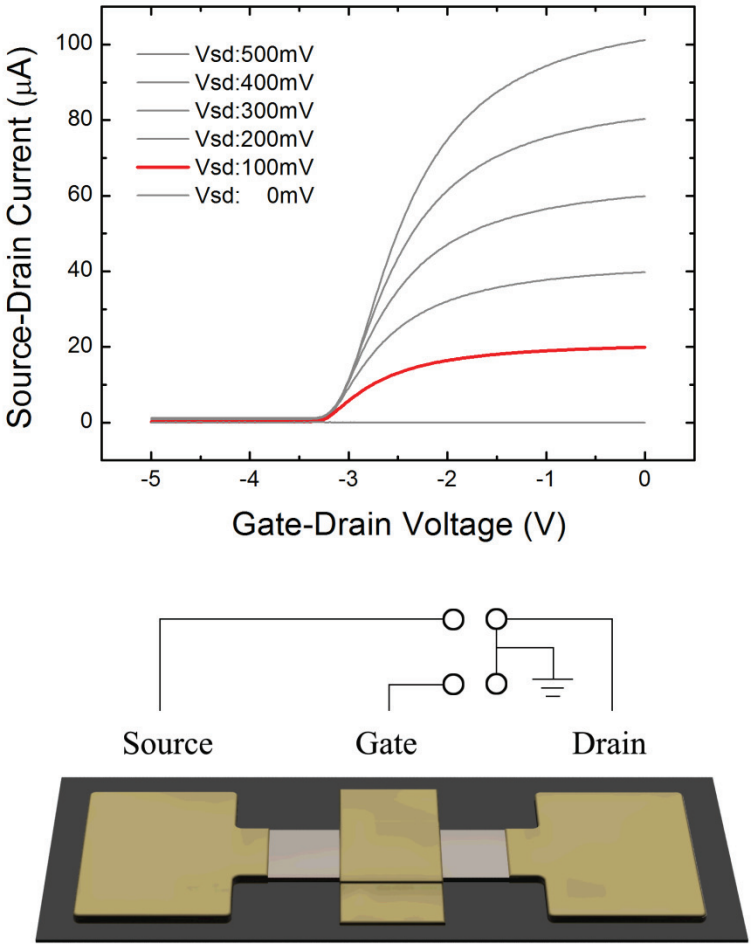


**Figure 14 | Characteristics of a Metal Oxide Gated HEMT.** Illustration of a metal-gated device together with a typical output characteristics, that is, of the source-drain current as a function of the gate-drain voltage.

These devices were optionally gated with either a metal-insulator ($SiO_2$/Ti/Au) or Schottky (Pt) contact as illustrated in **Figure 14**. The devices are normally depletion-mode transistors, being in a switched-on state at zero gate-drain voltage, and the source-

drain voltage as a function of source-drain current will retain the ohmic behavior seen in **Figure 11**. As indicated in **Figure 14**, if two floating DC power supplies are directly shorted to ground and drain on their low terminals and a constant voltage is supplied across source-drain, as the gate-drain voltage becomes more negative the corresponding upwards band bending pulls the 2DEG channel away from the Fermi level (**Figure 9**) shutting the device off. The corresponding plot can be seen in **Figure 14** for source-drain voltages from 0-500 mV in 100 mV steps. As it can be seen, the device is not completely switched on at 0V. The maximum transconductivity, which is the position of largest slope is at a gate-drain voltage of -2.8 V, and the threshold voltage is at -3.2 V.

## 3.3 A Novel Measurement System and an Overview of Solution-Gate Devices

In order to analyze the gate potential response of (bio)molecularly modified SGHEMTs, a special measurement and automation system was constructed to regulate and change the environment of the devices in a controlled manner. This system was further used for characterizing the effects of operating solution gated devices under ionizing radiation. Here, we will make a brief description of the semiconductor/electrolyte interface.[141]

Starting from the left of **Figure 15**, a semiconductor band structure is illustrated where $E_V$ is the valence band edge, $E_F$ is the Fermi level, $E_{(C\text{-}F)}$ is the difference between the conduction band edge and Fermi level, $E_C$ is the conduction band edge, and $E_{BB}$ is the degree of band bending. If we first consider the semiconductor in vacuum, usually a space charge layer is formed when the majority carriers from the semiconductor bulk are captured in surface states, which are caused by the abrupt termination of the crystal, and a space charge of uncompensated ionized donors or acceptors is built up in the semiconductor.[142] When the surface is placed into contact with an electrolyte solution, free carriers of the semiconductor can additionally be transferred to redox ions with appropriate energy levels in the solution to compensate for an initial difference in the chemical potentials between the two phases.[143] Furthermore, reactants in the solution may also alter the surface termination, leading to a change in surface charge. In what manner

the electrolyte will then interact with the surface can be described by the Gouy-Chapman-Stern model, which is divided into two regions, the Helmholtz double layer and the Gouy-Chapman layer.[143,144]

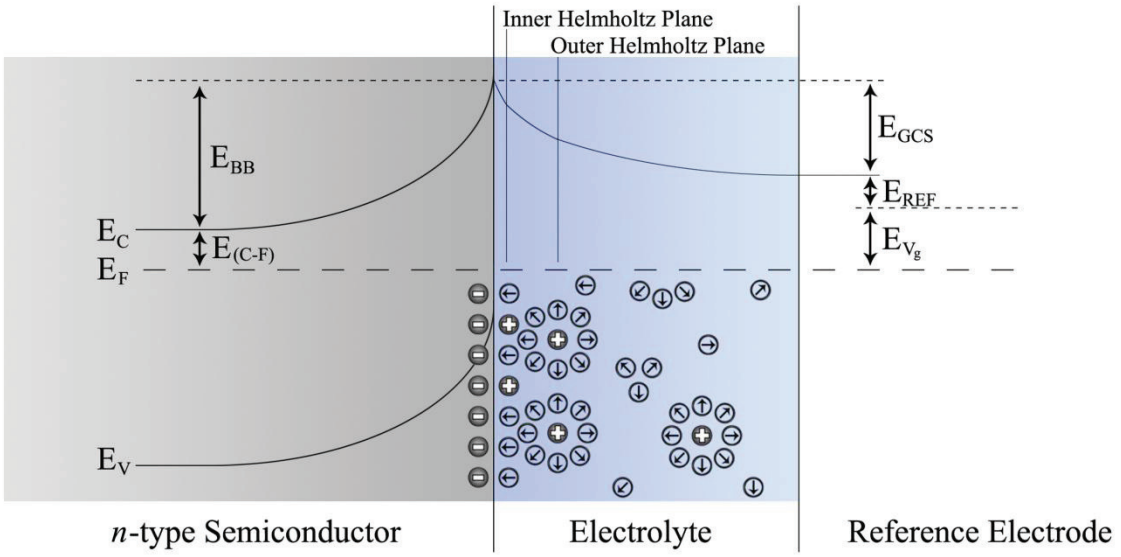


**Figure 15 | Qualitative Illustration of the GaN/Electrolyte Interface Energies.** $E_V$ is the bulk valence band edge, $E_F$ is the Fermi level, $E_C$ is the conduction band edge, $E_{BB}$ is the band bending, $E_{(C\text{-}F)}$ is the difference between the conduction band edge and the Fermi level, $E_{CGS}$ is the drop predicted by the Gouy-Chapman-Stern model, $E_{REF}$ is the standard electrode potential, and $E_{Vg}$ is the gate-drain potential.

The Helmholtz double layer consists of inner and outer Helmholtz planes and plays a major role in most electrochemical processes. The inner plane is formed by unsolvated ions which are adsorbed electrostatically or chemically to the solid surface, which together with the plane of closest approach for solvated ions forms the double layer (**Figure 15**). Beyond these two layers, in particular for solutions with low ionic concentrations, the charge of the solid surface may still not be completely shielded. In this case, a diffuse layer in which an excess of ions of one charge exists, extends from the outer Helmholtz plane into the solution and is referred to as the Gouy-Chapman layer. Eventually, the surface is completely shielded, the potential drop saturates and is designated as $E_{GCS}$ for the drop predicted by the Gouy-Chapman-Stern model.

In this work, and generally in electrochemistry, it is important to use a reference electrode.[145] This is because, if an arbitrary conductor is placed into the solution with a potential applied to it, $E_{REF}$ (**Figure 15**) would be a function of the current passing

through it. Here, an electrode whose potential does not vary with current is referred to as an ideal non-polarizable electrode. The Ag/AgCl reference electrode used in this work is robust and dose not polarize for small currents, keeping $E_{REF}$ constant, and therefore is widely used in electrochemistry. This electrode consists of a silver wire coated with silver chloride, which is immersed in a saturated solution of chloride ions and separated from the electrolyte by a porous frit. The relevant redox reaction is

$$AgCl_s + e^- <=> Ag_s + Cl^- \quad (7)$$

If too much current is passed in one direction through such an electrode, it will drive this process either completely to the right or left and it will start to polarize. To stop this from happening, the reference electrode is connected to a high impedance input and an inert non ideal electrode is place into the solution connected to a low impedance output well away from the other electrodes. This "counter" electrode is used to regulate a favorable potential measured by the reference electrode, in this work 0 V. The reference potential can be derived through the Nernst equation,

$$E_{REF} = E^0 + \frac{RT}{nF} \cdot -ln(a_{Cl^-}) \quad (8)$$

where $E^0$ is the standard electrode potential, $a_{Cl^-}$ is the activity of $Cl^-$ ions, $R$ is the gas constant, $T$ is the temperature in Kelvin, $F$ is the Faraday constant, and $n$ is the number of electrons exchanged in **Equation (7)**. This equation shows two important things; the temperature must be known or kept constant, and the concentration of chloride in the electrode chamber must be kept saturated or $E_{REF}$ will start to drift. Through the control of the potentiostat, the reference electrode represents system ground and the semiconductor potential can be offset relative to Ag/AgCl.

A typical output and set-point values for a (bio)molecularly modified SGHEMT can be seen in **Figure 16**, together with a schematic of how the previously discussed electrodes were configured. The device responds to electrical and electrochemical changes, in a very similar manner to that of devices with gate oxides and metallization (**Figure 14**). We found that the most advantageous way of characterizing the devices in solution was to, for example, start with the source-drain voltage set to 0 V and sweep the gate-drain voltage at 100 mV steps to -3.5 V. Here, the voltage is set and then the current is measured after a

predefined settling time has been reached. The advantage comes from this first line because the source-drain meter is at its most sensitive range and any deviation from zero current, due to a leakage path formed between the source-meter and the solution (potentiostat), will be detected here before the device is irreparably damaged.

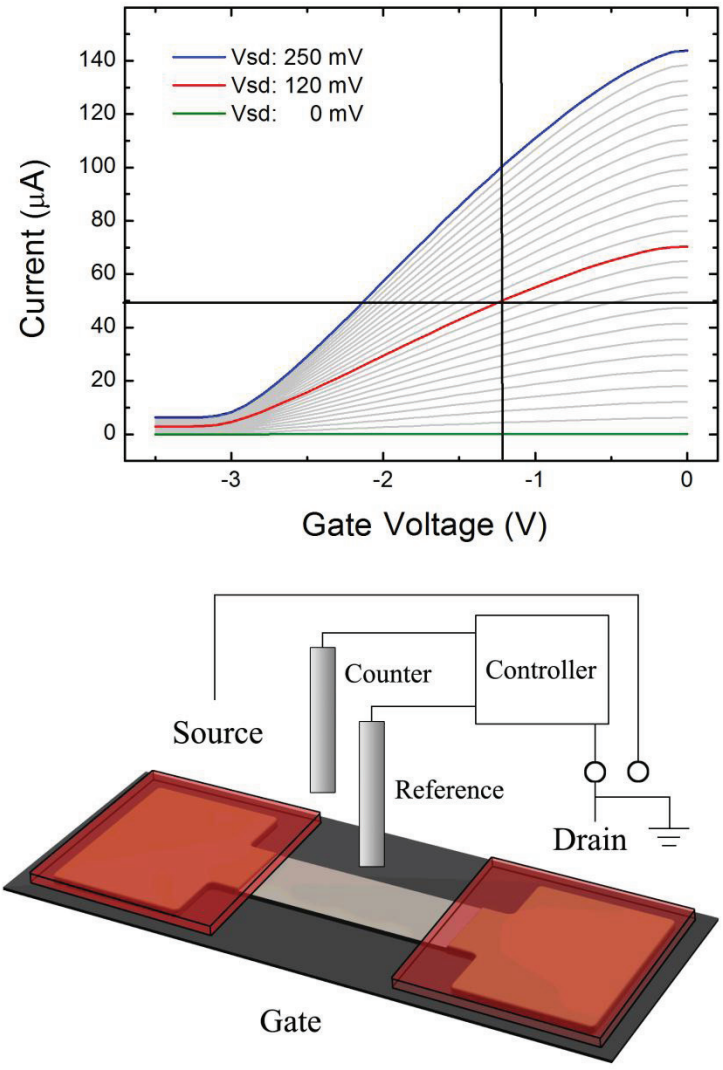


**Figure 16 | Typical Gate-Drain SGHEMT Characteristics.** Source-drain current as a function of the gate-drain voltage. The lower part shows the electrode configuration used in this work; Pt counter-electrode, Ag/AgCl reference-electrode, and a SGHEMT as work-electrode.

These gate-drain sweeps are made for every 10 mV source-drain step, producing a matrix of just under 1000 points. The data in **Figure 16** shows the threshold potential at around -3 V and that the device does not completely shut down. Since there is no current change

for gate voltages beyond the threshold potential, it is due to leakage current through the GaN buffer layers between the source and drain contacts. It is therefore usually due to a fabrication feature or persistent photocurrent, which is not detrimental to the measurements. To make a choice of the initial operating point we rely on the transposed matrix information of the source-drain current as a function of source-drain voltage.

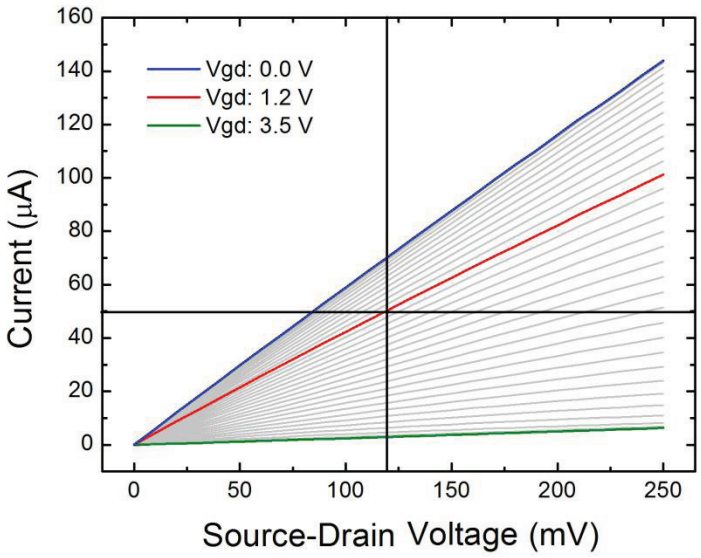


**Figure 17 | Typical Source-Drain SGHEMT Characteristics.** Source-drain current as a function of the source-drain voltage

The result can be seen in **Figure 17**; the dependence is linear, showing that the contacts are behaving ohmically in this potential window. A suitable operational power level can be chosen by interpolation of the matrix. The optimum gate voltage set point would be at the largest value of the first derivative, which is around -2 V in **Figure 16**. However, the voltage set point used throughout this work, especially in conjunction with biomolecules functionalized on the surface, was kept at gate-drain voltages around -1 V. This window of operation is placed between the positive and small negative potentials that can cause anodic etching from the above bandgap light in the laboratory ambient, and large negative potentials that cause surface bound organic molecules to degrade.

In contrast to the bulk semiconductor material it is based upon, the HEMT is a positive temperature coefficient (PTC) thermistor, increasing its resistance with increasing temperature. This is due to the temperature induced resistance increase, arising from

scattering processes, thereby requiring the gate voltage to increase in order to retain the same source-drain set-point current. **Figure 18** shows the change in gate-drain voltage for different temperatures and the device shows a sensitivity of approximately 18 mV/°C.

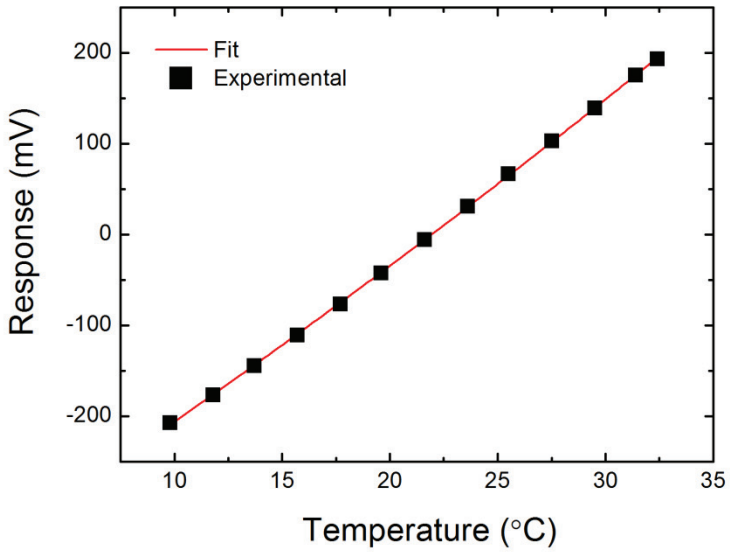


**Figure 18 | Typical SGHEMT Temperature Dependence.** The response, or change in gate-drain voltage, from cyclic temperature-dependent measurements showing a sensitivity of approximately 18 mV/°C.

One use of such a device is to determine the concentration of specific ions in the electrolyte it is submersed in. Electrochemical impedance studies on *n*-type GaN electrodes found a linear *p*H dependence of the flatband voltage of 55 mV/*p*H,[30] which was confirmed with thermally oxidized GaN/AlGaN/GaN devices at a nearly Nernstian *p*H-response of about 56 mV/*p*H in aqueous solutions.[31] The term, Nernst, comes from the fact that the influence of the cell potential, $E_{cell}$, as a function of pH, 'seen' by the transistor is defined like previously through the Nernst equation as

$$E_{cell} = E^0 + \underbrace{\frac{2.303 \cdot RT}{nF}}_{0.0592\ V} \cdot \underbrace{-log_{10}(aH^+)}_{p\mathrm{H}} \qquad (9)$$

where $E^0$ is a constant offset and can be ignored, $aH^+$ is the activity of hydrogen ions, $R$ is the gas constant, $T$ is the temperature in Kelvin (here the equivalent of 25 °C), $F$ is the Faraday constant, $n$ the number of electrons exchanged, which here is one, and the constant 2.303 that comes from converting the natural logarithm to base 10. Thus, the closer the gate-drain voltage per *p*H is to 59.2 mV/*p*H (for room temperature) it fits a

Nernst behavior. We note that it is also important to consider using buffers to stabilize the electrolyte while titrating.[145]

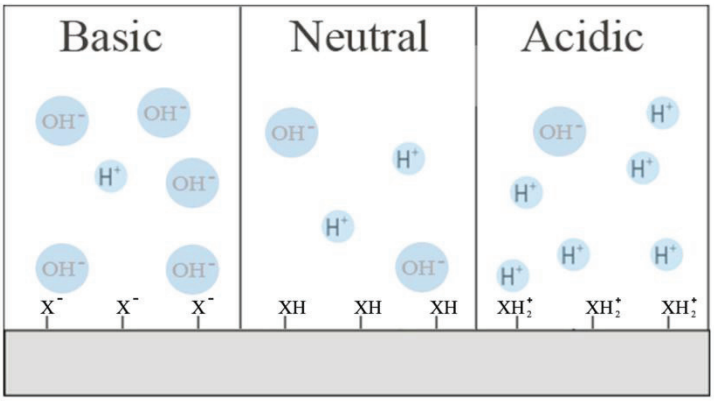


**Figure 19 | Illustration of the Site-Binding Model.** An illustration of the surface charge change as a function of *p*H predicted by the site-binding model.

The surface charge dependence on *p*H can be explained by the site binding model.[33,146,147] It proposes that certain surface atoms such as oxygen are amphoteric, acting as both an acid and a base depending on the solution *p*H and the material specific dissociation constants. The main idea is illustrated in **Figure 19**. In basic conditions, for example, around *p*H 7-11, the metal oxide surface releases protons and becomes negatively charged, consequently decreasing the sheet carrier density of the 2DEG[31,34] and increasing the channel resistance, requiring the control program to supply a more positive voltage to the gate in order to keep the source-drain current constant. As the *p*H is decreased into the acidic region, for example around *p*H 3-7, the metal oxide surface tends to accept protons, passing the point of zero charge where the oxidic surface is hydrogen-terminated and neutral, and ending with a more positive charge as an additional protons are bound to the surface. This positive charging of the surface causes the gate resistance to fall and a corresponding negative voltage to be applied to the gate to compensate. In **Figure 20** a comparison of the change in gate voltage in dependence on *p*H, of GaN and hydrogenated diamond surfaces is shown. The points represent a complete *p*H cycle where the SGFET solution is titrated in both directions, for example, from acidic to basic and *vice versa.*

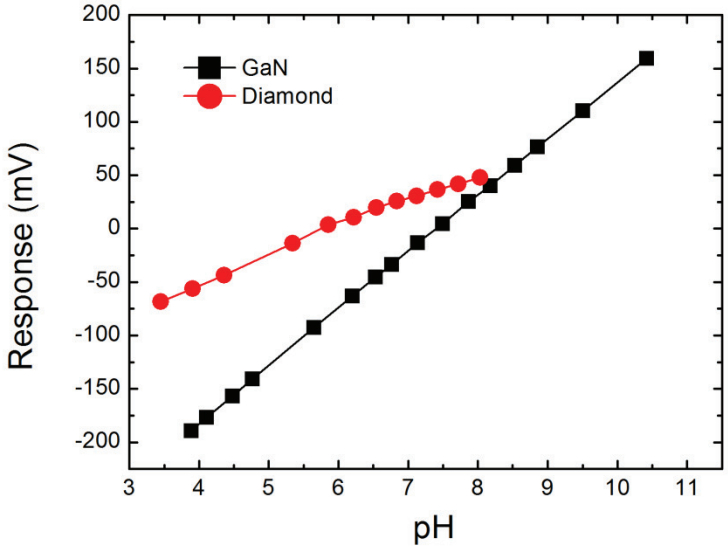


**Figure 20 | SGHEMT vs. Diamond *p*H Dependence.** The response, or change in gate-drain voltage, of cyclic *p*H measurements showing the difference between GaN (53.3 mV/*p*H at 10.6 °C) and diamond (25.9 mV/pH at 22 °C) devices.

As can be seen, hydrogenated diamond surfaces are also *p*H sensitive, but have a different detection mechanism.[148] The difference in sensitivity between GaN and diamond devices are 53.3 mV/*p*H at 10.6 °C and 25.9 mV/*p*H at 22 °C, respectively, with no hysteresis.

## 3.4 New Sensors with High Transconductive Gain Through Thinner Heterostructures

In addition to optimizing the channel widths, we have investigated the influence of increasing the barrier height and decreasing the 2DEG-to-surface distance by replacing the AlGaN barrier with a thinner AlN barrier in SGHEMTs, to increase the devices transconductive *p*H sensitivity.[105] This means optimizing the device to increase the largest value obtained by the first derivative of the source-drain current ($I_{sd}$) as a function of gate-drain voltage ($U_{gd}$), or transconductance maximum ($g_m^{max}$), which can be written as

$$g_m^{max} = \left(\frac{\partial I_{ds}}{\partial U_{gd}}\right)^{max} = \left(\frac{W}{L}\right) \cdot U_{ds} \cdot \mu^{max} \cdot \frac{\varepsilon_r \cdot \varepsilon_0}{z} = \mathrm{K} \cdot \frac{\mu^{max}}{z} \qquad (10)$$

where $W$ is the width, $L$ is length, $U_{ds}$ is the source-drain voltage, $\varepsilon_r$ is the relative permittivity $\varepsilon_0$ is the vacuum permittivity and $z$ is the 2DEG-to-solution distance. Here, we optimize the transconductance by changing the mobility and the solution to 2DEG distance.

| | **GaN/AlN** | **GaN/AlGaN** |
|---|---|---|
| **Layer 1 (Top)** | 3 nm GaN | 3 nm GaN |
| **Layer 2** | 4.5 nm AlN | 16 nm $Al_{0.27}Ga_{0.73}$ |
| **Layer 3** | GaN | GaN |
| **Layer 4** | GaN:Fe | GaN:Fe |
| **Layer 5 (Substrate)** | 330 µm Sapphire | 330 µm Sapphire |
| **Barrier Thickness** | 7.5 nm | 19 nm |

**Table 2 | Stacking thicknesses of two PAMBE-Grown Samples.**

The maximum mobility for a GaN/AlGaN 2DEG is known to vary between 800-2000 $cm^2/Vs$ at room temperature, depending on growth technique and structure. Higher mobilities can be achieved by, for example, minimizing alloy scattering by placing an AlN spacer between the GaN and AlGaN, decreasing the 2DEG carrier concentration by varying the AlGaN thickness, changing the underlying carrier density in the GaN buffer by creating a highly resistive film with carbon compensation and using higher concentrations of Al in the AlGaN alloy (12% → 35%). Optimization of $z$, can be achieved by, for example, using the inverse polarity (N-face GaN) which places the 2DEG on top of (instead of under) the AlGaN barrier. This, however, can only be easily achieved by PAMBE and not MOCVD, which is known to produce higher crystalline quality. N-face material is also known to be more unstable in aqueous solutions. Here we compare PAMBE-grown samples with different structures, which are listed in **Table 2**. The experimental results obtained from these samples are in agreement with **Equation (10)**, as can be seen in **Figure 21a**. Here, the GaN/AlN samples, having a higher mobility and smaller 2DEG-to-surface distance, had a higher maximum transconductance of 131 µS, or transconductivity of 17500 S/m, at a gate-drain voltage of -0.24 V and device shutdown voltage at -1 V.

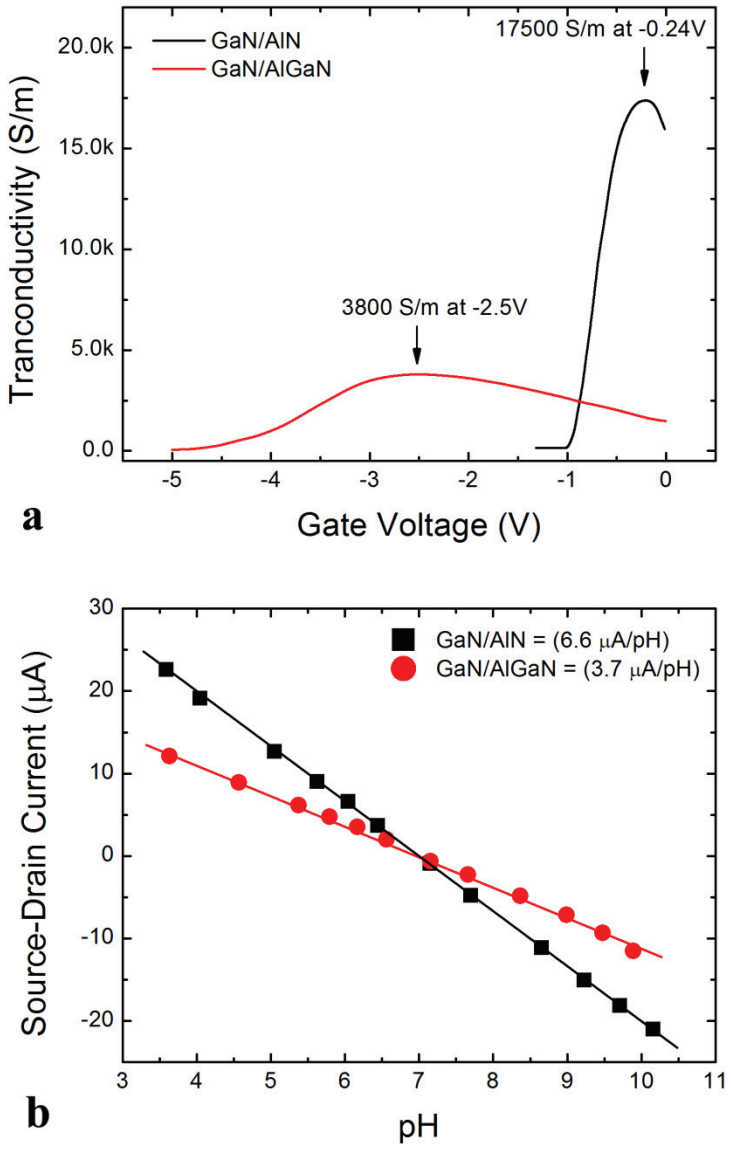


**Figure 21 | Transconductivity enhancement for devices with thin AlN barriers.** The AlN device has a higher mobility and smaller 2DEG-to-surface distance than the AlGaN device, the results of which can be seen in **a)** the higher transconductivity and **b)** the source-drain current dependence on the gate solution's *p*H.

In comparison, the GaN/AlGaN samples, having a lower mobility and larger 2DEG-to-surface distance, had a smaller maximum transconductance of 72 μS, or transconductivity of 3800 S/m, at a gate-drain voltage of -2.5 V and a 5 times larger device shutdown voltage at -5 V.

*p*H-induced changes in the surface potential were evaluated between *p*H 4 and 10 for the samples by regulating a constant source-drain current by changing the gate-drain voltage. The devices *p*H sensitivity was in good agreement with each other at approximately 52 mV/*p*H, and exhibited good chemical stability and reproducibility. While the surface potential mainly depends on the chemical characteristics of the device surface, the pH-dependence of the source-drain current at constant source-drain and gate-drain voltages is strongly affected by the electrical characteristics of the 2DEG, such as the transconductance. **Figure 21b** shows the devices source-drain current dependence on the solution-gates *p*H, where the gate-drain voltage was set to the highest point of transconductance at *p*H 7. Despite the devices inherent nonlinearity, a linear dependence was used to calculate the sensitivity of 6.6 µA/*p*H and 3.7 µA/*p*H for the GaN/AlN and GaN/AlGaN devices respectively. We note that increasing the transconductivity is advantageous in constant source-drain current mode as it increases the devices dynamic range.

## 3.5 Overview of the Ionizing Radiation Cross-Section for GaN

Ionizing radiation is radiation composed of particles that individually can liberate one or several electrons from an atom or molecule, producing ions. It is usually quantified as absorbed dose, which is a measure of the energy deposited per unit mass of medium and represented with the units Joule per kilogram (*J/kg*) or Gray (*Gy*). Therefore, the absorbed dose not only depends on the incident radiation but also on the absorbing material.

Information about the material specific absorption for narrow beams of monoenergetic photons is tabulated as the *mass attenuation coefficient*, and can be obtained through the exponential power law

$$\frac{I}{I_0} = e^{-\kappa \cdot \rho \cdot x} \qquad (11)$$

where $I_0$ is the incident intensity penetrating a material with a mass attenuation coefficient $\kappa$ (cm$^2$/g) with a material density $\rho$, and emerging with intensity $I$ after passing the

material thickness $x$. The mass attenuation coefficient for gallium is plotted in **Figure 22**, using tabulated values of $\kappa$ that can be found elsewhere,[149,150] and clearly shows the electron core level transitions.

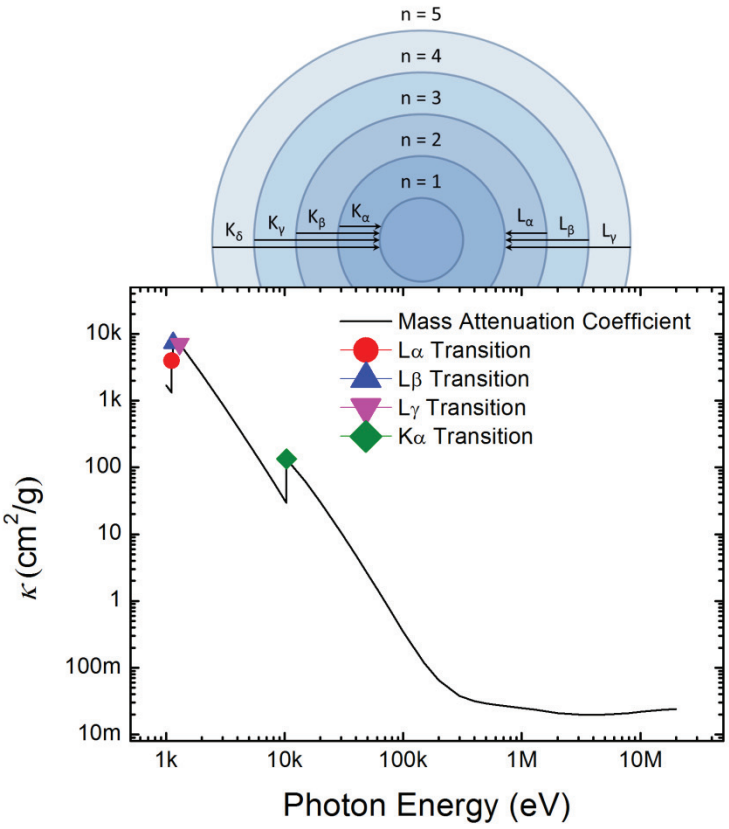


**Figure 22 | The Mass Attenuation Coefficient for Ga as a Function of Photon Energy**. The atomic electron core level transitions can be clearly seen and are defined in the illustration.

There is extensive work behind theoretically adapting $\kappa$ to quantify the energy absorbed for specific processes. In this work we used the unmodified "direct" mass attenuation coefficient to create a model of the X-ray beam characteristics from known variables like the measured air kerma. However, we note that the mass energy-transfer coefficient, defined as "the sum of the kinetic energies of all those primary charged particles released by uncharged particles per unit mass",[149] while having a negligible influence in this work, gives a better description of kerma.

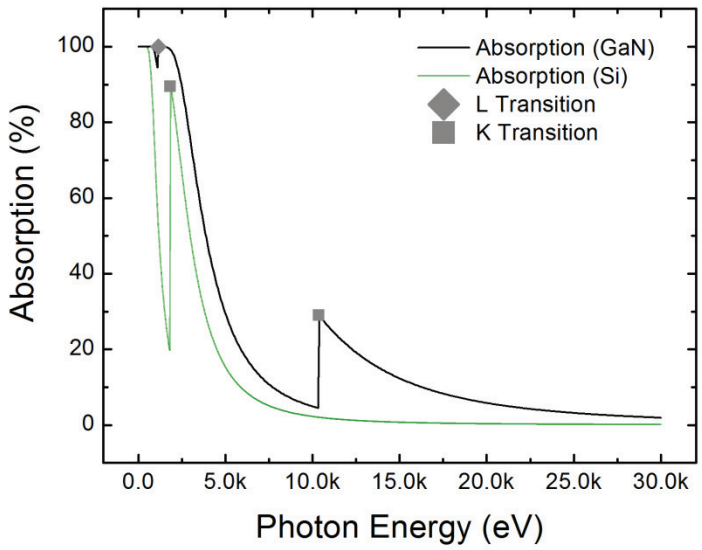


**Figure 23 | Absorption of X-ray Radiation in GaN vs. Si.** The absorption calculated for 3 μm of GaN and 3 μm of Si calculated through the exponential power law.

To illustrate the exponential power law, the cross-section for 3 μm of GaN was calculated between 10 eV and 30 keV, and the result is plotted in **Figure 23**. According to Moseley's empirical formula, since gallium has the largest atomic number, the *K*-shell transition energies at approximately 10 keV will be the highest within the system studied here. As the absorbance from the K-transition peak disappears beyond 20 keV, it becomes apparent why the 40-300 kV medical X-ray spectrum is expected to be poorly suited for thin films of GaN.[74] As a reference point, since many state-of-the-art detectors are based on Si, its absorption is shown in comparison to GaN in **Figure 23**. Si has its *K*-shell transition energies at around 1.8 keV, illustrating the advantages of using a material with larger atomic numbers.

# 4 Hybrid GaN/(Bio)Molecular Interfaces

In this chapter, we investigate the photo-degradation process used to create patterned regions of chemical functionality for self-assembled organosilane monolayers on GaN. Here, we study the energetic alignment between the semiconductor and organic molecules to support charge transport across the GaN/(bio)molecular interface and determine a new semiconductor alignment required for low energy photo-induced charge transfer ionization of alkyl chains well below the energy normally required for molecular cleavage. Furthermore, we used similar functional molecules to immobilize enzymes to the surface of SGHEMTs and show original results on the influence of the immobilization process on enzyme functionality in conjunction with a novel electrochemical and environmental control system.

## 4.1 A New Photocatalythic Degradation Effect of Organic Films

In the present work, silanization was performed using ODTMS to create SAMs of ODS on OH-terminated *n*- and *p*-type GaN as well as *n*- and *p*-type 6*H*-SiC. Although alkyl chain molecules decompose radically when subjected to high energy UV irradiation,[151] they remain stable when the wavelength is well below the molecular ionization energy. However, this stability can be compromised if a level is present to support an ionization charge transfer under lower energy excitation. For the current investigation, filtered light from a low pressure Hg lamp with a wavelength of 254 nm was used, corresponding to an energy higher than the bandgap of both GaN and 6*H*-SiC but below the threshold required for direct ionization or generation of ozone, atomic oxygen and hydroxyl radicals from air.[152,153]

Primary characterization of the alkylsilane SAMs was performed by TDS and SWCA measurements. TDS confirmed previous analyses performed on ODS-functionalized GaN

and SiC, in that the desorption enthalpies of hydrocarbon fragments leaving the surfaces indicate strong covalent attachment of molecules. Essentially no desorption of physisorbed contaminants was observed after moderate heating.[15,16]

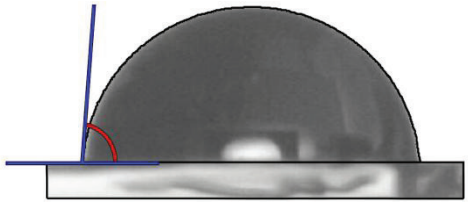

| Substrate | Doping | Native oxide | ODS | ODS + UV |
|---|---|---|---|---|
| **HEMT** | Undoped | < 10 ° | > 100 ° | **≈ 20 °** |
| **GaN** | *n*-type | < 10 ° | > 100 ° | **≈ 20 °** |
| **GaN** | *p*-type | < 10 ° | > 100 ° | > 100 ° |
| **SiC** | *n*-type | < 10 ° | > 100 ° | > 100 ° |
| **SiC** | *p*-type | < 10 ° | > 100 ° | > 100 ° |

**Table 3 | Comparison of Static Water Contact Angles for Native Oxide, ODS-Functionalized and UV (> 3.4 eV) Illuminated ODS Functionalized, *n*- and *p*-type GaN and SiC.** The accompanying image illustrates how the SWCA is obtained from the measurement photographs.

Assessment of the hydrophobicity was carried out both before and after functionalization by SWCA measurements and the results are presented in **Table 3**. After hydroxylation, all samples exhibit contact angles of less than 10°. Following ODS functionalization, all contact angles exceeded 100°. In comparison, contact angles of up to 110° have been reported for high quality, dense ODS monolayers on oxidized Si surfaces.[154] Following illumination at 254 nm a substantial reduction of the contact angle, from the initial value of >100° to a saturation value of 25° after 30 min of illumination, was observed for ODS-functionalized *n*-type GaN and a nominally undoped (*n*-type) HEMT, whereas no significant changes were observed for the surfaces of *p*-type GaN, as well as *n*- or *p*-type SiC. The illumination time required for the contact angle reduction on *n*-type GaN could be accelerated to approximately 1 min by illumination through a water droplet covering the sample surface. Wavelength-dependent measurements were performed on *n*-type GaN, showing that above-bandgap illumination (energies larger than approximately 3.4

eV) is necessary for the contact-angle to saturate at approximately 25° within the aforementioned timeframe.

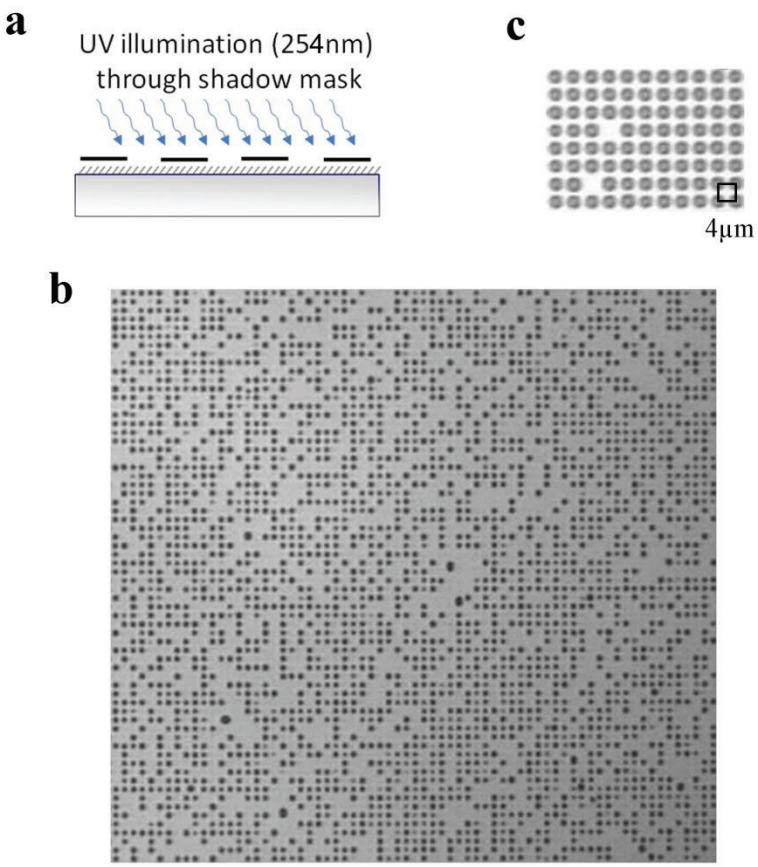


**Figure 24 | UV Illumination Through a Shadow Mask. a)** A cross-sectional diagram of the GaN thin film / ODS monolayer / shadow mask, illustrating how the patterned illumination is made. **b)** Water condensation, formed on a patterned cooled surface, which produces a hydrophobicity pattern consisting of 4 µm dots exemplified in **c)**.

No significant change of the contact angle was observed upon illumination with sub-bandgap light. We note that the presence of low intensity near-UV light from the laboratory ambient, which contains wavelengths shorter than approximately 365 nm, was enough to slightly degrade the contact angle of *n*-type GaN, saturating at a value of 90°. For practical reasons, the remaining experiments were performed using samples exposed to laboratory light. The hydrophobic/hydrophilic contrast between as-prepared and illuminated surfaces is highlighted in **Figure 24**, in which an ODS-modified *n*-type GaN surface was selectively illuminated at 254 nm through a shadow mask and subsequently subjected to water vapor. The retention of the pattern fidelity after illumination

demonstrates the potential utility of UV-induced SAM degradation for selective spatial modification of surface properties.[155]

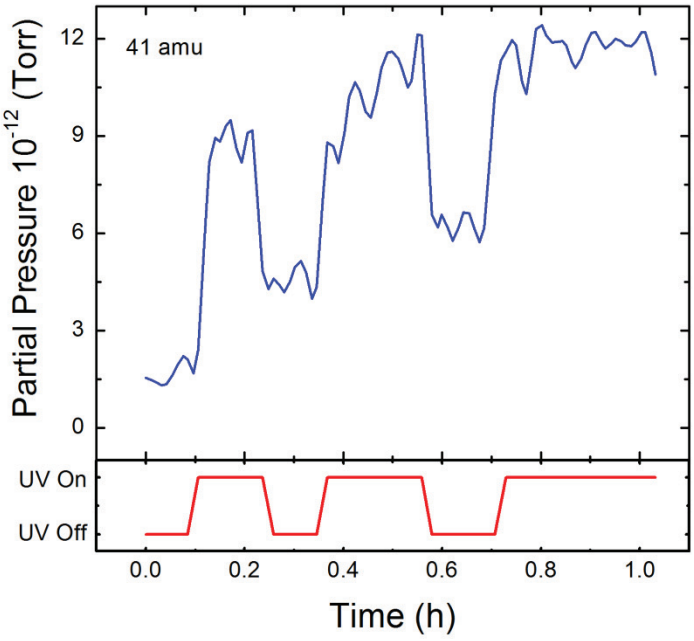


**Figure 25 | TUVDS Measurements of the Organosilane Degradation.** The time-dependent partial pressure mass spectrum (41 amu, corresponding to $C_3H_5$) of functionalized *n*-type GaN along with the on/off times of UV illumination.

Transient measurements of the partial pressures of specific masses under high vacuum during UV illumination, or Transient UV Desorption Spectroscopy (TUVDS), of *n*-type GaN were performed. The temporal evolution of the partial pressure mass spectrum of the most prominent ODS fragments[15] from a functionalized *n*-type GaN sample upon exposure to UV illumination were recorded. The result for one such fragment, 41 amu corresponding to $C_3H_5$, is shown in **Figure 25**. We note that, owing to the pronounced sensitivity of the desorption rate on the presence of residual water on the surface, quantitatively reproducible TUVDS data are currently not available. Nevertheless, the modulation in magnitude of the partial pressure is synchronous with that of the UV source and only occurs in the presence of functionalized *n*-type GaN samples, proving the direct relationship between UV illumination and degradation of the covalently bound organic monolayer. Furthermore, the sensitivity of the measurement to residual water is consistent with the water acceleration effect observed during SWCA measurements.

## 4.2 Characterization of the Degradation

To more specifically understand the process of UV-induced changes in the SWCAs, we studied the impact of irradiation on the chemical and structural properties of the organic films.

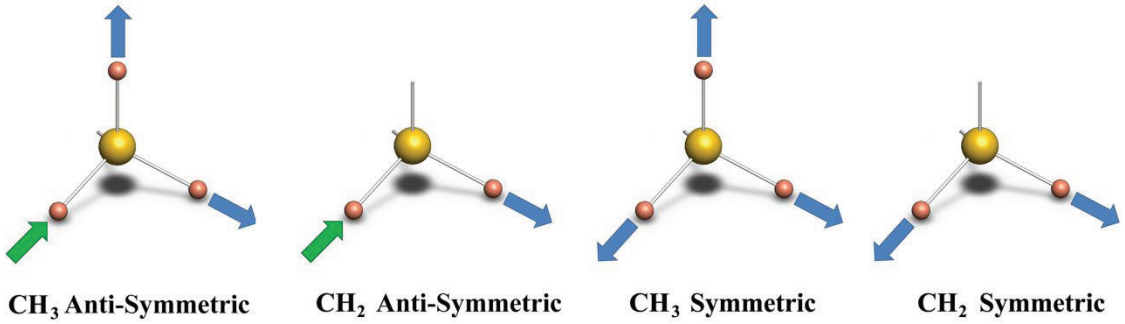


| Molecule | Mode | Wavenumber ($cm^{-1}$) |
|---|---|---|
| **$CH_3$** | Anti-Symmetric Stretch | 2962 ±10 |
| **$CH_2$** | Anti-Symmetric Stretch | 2926 ±10 |
| **$CH_3$** | Symmetric Stretch | 2872 ±10 |
| **$CH_2$** | Symmetric Stretch | 2855 ±10 |

**Table 4 | Characteristic IR Vibrational Modes for Hydrocarbon Compounds.** Infrared stretching vibrational modes of $CH_3$ and $CH_2$ together with their absorption wavenumber and graphical representation. Here, carbon atoms are yellow and hydrogen atoms are orange and the blue arrows indicate hydrogen movement away from carbon while the green arrows indicate hydrogen movement towards carbon.

Here, we analyze ATR-FTIR absorption spectra between 3000-2800 $cm^{-1}$ and study the anti-symmetric and symmetric vibration modes of $CH_2$ and $CH_3$. Their corresponding wavenumbers and a graphical illustration of the vibrations can be seen in **Table 4**.[156] Analyzing the peak positions gives information about the SAMs order. For example, the anti-symmetric $CH_2$ peak has values for its crystalline phase at approximately 2915 $cm^{-1}$, increasing to approximately 2926 $cm^{-1}$ for its liquid phase. Furthermore, quantitative analysis of the calibrated ATR-FTIR spectral intensities provides a relative measure of the quantities of hydrocarbons on the surfaces.

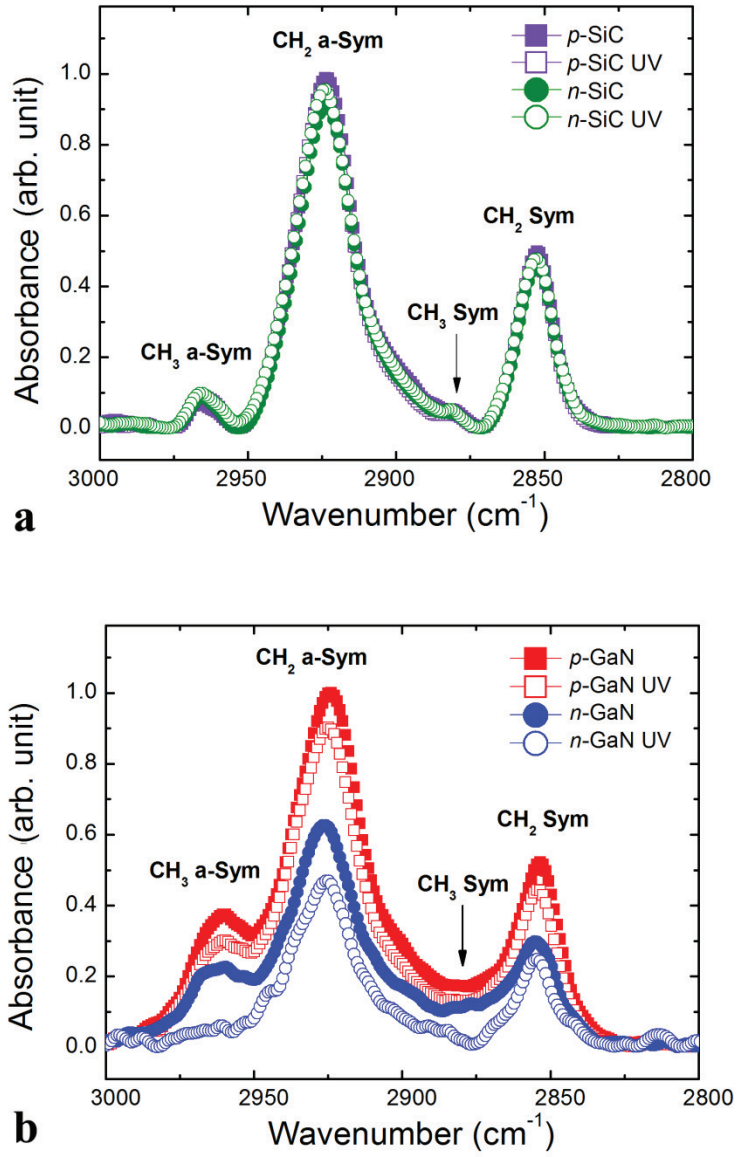


**Figure 26 | ATR-FTIR Spectra in the Region of Hydrocarbon Stretching Modes.** Peaks correspond to the anti-symmetric $CH_3$ ($CH_3$ a-Sym), anti-symmetric $CH_2$ ($CH_2$ a-Sym), symmetric $CH_3$ ($CH_3$ Sym), and symmetric $CH_2$ ($CH_2$ Sym) stretching vibrations. **a)** *n*- and *p*-type SiC measured before and after UV irradiation showed no significant degradation of the monolayer. **b)** *n*- and *p*-type GaN measured before and after UV irradiation reveal significant degradation of the monolayer, including an almost complete disappearance of the $CH_3$ mode, after UV illumination for the case of *n*-type GaN.

The spectra of *n*- and *p*-type SiC and GaN before and after UV illumination can be found in **Figure 26**. All of the samples exhibit modes corresponding to anti-symmetric $CH_3$ ($CH_3$ a-Sym), anti-symmetric $CH_2$ ($CH_2$ a-Sym), symmetric $CH_3$ ($CH_3$ Sym), and symmetric $CH_2$ ($CH_2$ Sym) stretching vibrations as indicated in **Figure 26**. We note that,

the lower spectral resolution used for the GaN spectra causes the peaks to overlap, and the weak signal from the symmetric $CH_3$ peak is difficult to identify. The $CH_2$ line positions for *n*- and *p*-type SiC and *p*-type GaN samples are red-shifted by approximately 2 $cm^{-1}$ relative to the liquid state, indicating partial ordering of the SAMs, since red-shifts of 4-5 $cm^{-1}$ are typically observed for highly ordered monolayers on $SiO_2$.[157] However, the anti-symmetric and symmetric $CH_2$ line positions for monolayers on *n*-type GaN are not shifted relative to those of liquid alkyl chains, indicating significant disorder within the SAM, in agreement with the relatively low SWCA after exposure to ambient light. Quantitative analysis of the calibrated ATR-FTIR spectral intensities provides a relative measure of the quantities of hydrocarbons remaining on the surfaces after illumination. The largest spectral intensities are observed immediately after functionalization of *n*- and *p*-type SiC and *p*-type GaN and very little change is observed upon illumination. In contrast, the absorbance of the as-prepared ODS SAM on *n*-type GaN is significantly reduced relative to that of the *p*-type sample due to stray ambient near-UV light exposure during sample preparation. Following 254 nm UV illumination, a significant reduction of the total hydrocarbon absorption is observed, along with an almost complete disappearance of the $CH_3$ vibrational mode from the end groups of the alkyl chain molecules.

Complementary chemical analysis was performed using XPS. The XPS spectra are fingerprints of atoms and their chemical bonds, which enables the identification of the chemical nature of a surface. Here, we use this technique to gather detailed information regarding changes in the chemical composition of the adsorbed layers due to UV irradiation. Quantitative analysis of the calibrated spectral intensities provides a relative measure of the quantities of hydrocarbons on the surfaces. Since the attenuation length of the photoelectrons is in the order of a few nanometers, a change in layer thickness can be confirmed by analyzing the change of underlying substrate peak intensities in comparison to that of the layer.

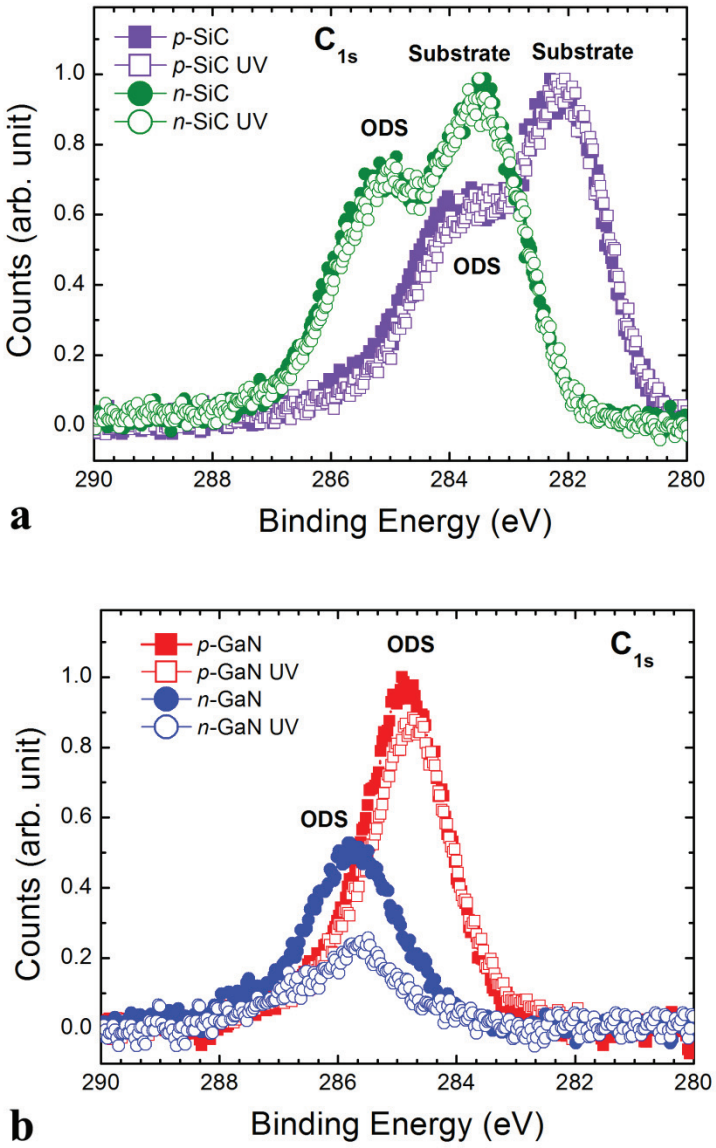


**Figure 27 | XPS Spectra of the $C_{1s}$ Core Level. a)** *n*- and *p*-type SiC measured before and after UV irradiation showed no significant degradation of the monolayer. **b)** *n*- and *p*-type GaN measured before and after UV irradiation reveal significant degradation of the monolayer following UV illumination for the case of *n*-type GaN.

Here, we evaluate the evolution of the $C_{1s}$, $Ga_{2p}$, $N_{1s}$ and $O_{1s}$ core signals for *n*- and *p*-type GaN and for the $C_{1s}$, $Si_{2p}$, and $O_{1s}$ core levels for *n*- and *p*-type SiC upon UV illumination. In the $C_{1s}$ spectra, shown in **Figure 27**, the energetic shifts between the *n*- and *p*-type samples are due to the changes of the Fermi levels with doping, but the shift is reduced due to the oppositely directed surface band bending. It is common in XPS that each peak will be distorted with the convoluted information from slight shifts that are

caused by differences from individual binding energies. In the case of the $C_{1s}$ spectrum of the SiC samples (**Figure 27a),** a double peak is formed from the $C_{1s}^{ODS}$ peaks being shifted far enough to lower binding energies from the $C_{1s}^{SiC}$ peaks. If the $C_{1s}^{ODS}$ peaks became smaller due to loss of material, an enlargement of the $C_{1s}^{SiC}$ peaks would be expected due to the correspondingly smaller amount of attenuation by the layer. However, the $C_{1s}$, $Si_{2p}$, and $O_{1s}$ core level signals are unaffected by UV illumination, confirming the stability of ODS on SiC.

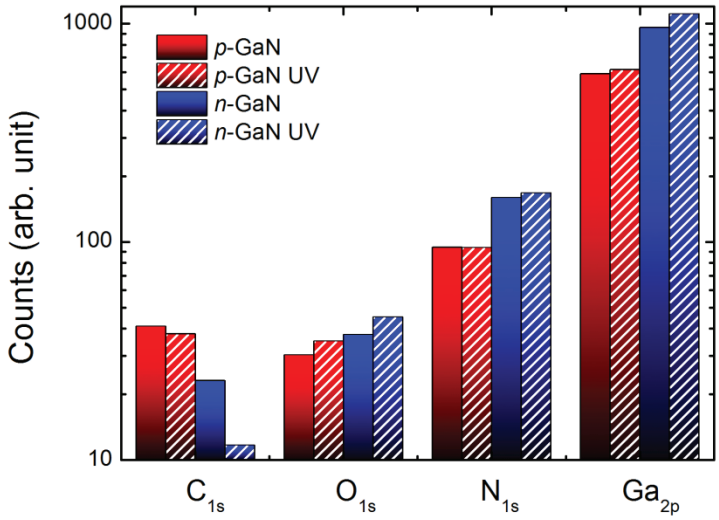


**Figure 28 | XPS Peak Height Comparison of Additional Core Levels.** *n*-type GaN measured before and after UV irradiation reveals significant degradation of the monolayer following UV.

While the core level signals originating from the organic SAMs for *p*-type GaN shows a similar stability to that of SiC, the non-UV-exposed *n*-type GaN already exhibited a reduced signal intensity due to ambient light exposure, while the UV-exposed sample exhibited significant additional degradation (**Figure 27b**), which is also consistent with the observations from ATR-FTIR measurements. Furthermore, following the UV degradation the $C_{1s}$ peak of the *n*-type GaN sample retains its width, despite the significant intensity reduction, indicating that the change is due to hydrocarbon desorption from the surface rather than chemical shifting of the binding energies. This is further strengthened by the loss of attenuation through the layer, seen as an increase in $O_{1s}$, $N_{1s}$, and $Ga_{2p}$ substrate core level signals for decreasing $C_{1s}$, which are summarized as peak height bars in **Figure 28**.

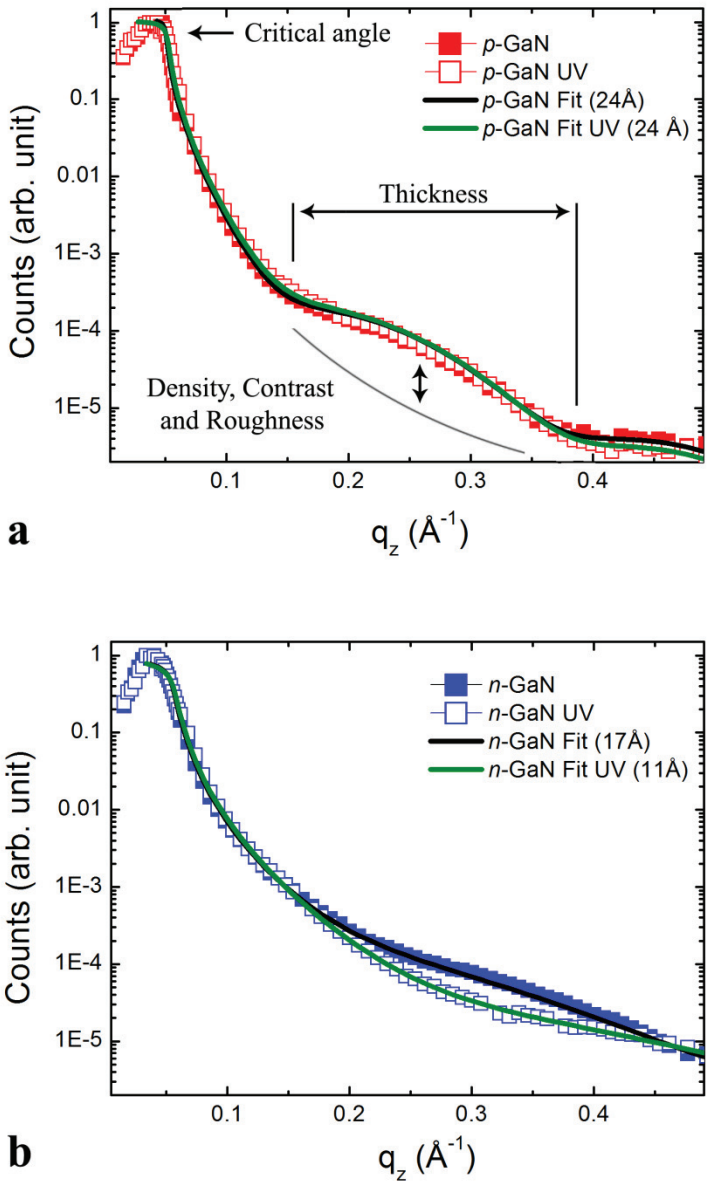


**Figure 29 | XRR Spectra of ODS/GaN Bilayers. a)** *p*-type GaN before and after UV illumination. **b)** *n*-type GaN before and after UV illumination. The obtained fitting parameters for the ODS film thickness are 24Å, 24Å, 17Å, and 11Å for *p*-GaN, *p*-GaN UV, *n*-GaN, *n*-GaN UV, respectively.

Quantification of the monolayer thicknesses of ODS on *n*- and *p*-type GaN upon UV illumination was achieved by XRR, which involves monitoring the intensity of an X-ray beam as a function of the specular angle. The measurement is started for an X-ray incident angle smaller than the critical angle of the sample, where the detector signal is at maximum due to total external reflection. Once it passes this angle, the beam penetrates the surface and the amplitude rapidly drops in a similar way to Fresnel reflectivity for

visible light. Here, "Kissing" fringes are generated by interfering reflections from the different interfaces and their periods are related to the thickness of the ODS layer. The absolute value of the scattering vector $q_z$ can be calculated from the X-ray's wavelength $\lambda$ and the specular angle $\theta$ as

$$q_z = 2 \cdot \underbrace{\frac{2\pi}{\lambda}}_{k} \cdot \sin\theta \qquad (12)$$

where $k$ is the wave vector of the X-rays. The spacing $\Delta q_z$, which represents the length of a period in $Å^{-1}$, can de directly used to obtain the thickness of the ODS layer as

$$d_{ODS} = \frac{2\pi}{\Delta q_z} \qquad (13)$$

This is illustrated in **Figure 29a**, where the data for the *p*-type samples both before and after illumination are presented. The fit gave an estimated monolayer thicknesses of 24 Å, which is in excellent agreement with the known molecular length of ODS.[158] The SAM thickness for the as prepared *n*-type GaN, **Figure 29b**, was 17 Å and decreased to 11 Å following UV illumination, supporting the previous measurements.

## 4.3 Explanation of the Cross Interface Charge Transfer Process

As summarized in **Figure 30**, for all samples there exists a strong correlation between the observations from all different measurement techniques. Among the four different ODS-functionalized samples, only *n*-type GaN showed a large degradation of the covalently bound SAM layer upon exposure to above bandgap light. The surface-bound and cross-linked ODS molecules possess $CH_3$ terminal groups. The combined observations of the $CH_2$ degradation and almost complete loss of $CH_3$ from ATR-FTIR spectra, the approximate halving of the layer thickness from XRR and the change of the hydrocarbon intensity from XPS demonstrate that the remaining (fully degraded) organic film is comprised of the remnants of the ODS molecules after degradation and that UV illumination does not simply reduce the aerial molecular density. Furthermore, the

absence of UV-induced degradation on *p*-type GaN as well as on *n*- and *p*-type SiC proves that the observed process is not inherent to the ODS monolayer itself but requires electronic interaction with the underlying substrate material.

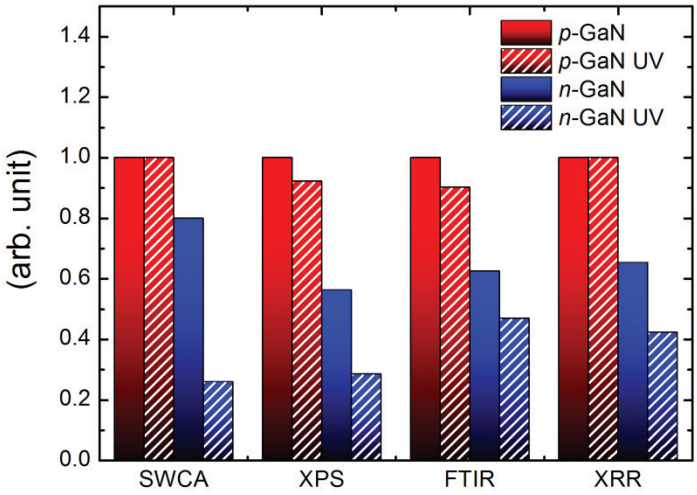


**Figure 30 | Summary of the Degradation Measurements**. Nnormalized changes of SWCA, XPS $C_{1s}$ core level intensity, ATR-FTIR spectral intensity, and XRR SAM thickness on *n*- and *p*-type GaN before and after illumination. Values are normalized to those found for *p*-type GaN prior to illumination (SWCA: 101°, XRR: 24 Å).

Degradation of organic monolayers on solid surfaces under UV illumination has been well studied and widely exploited for patterning of SAMs.[155] A range of radiation energies and materials systems have been used. Under UHV conditions, high energy UV illumination, originating from HeI and HeII emission, introduces defects into monolayers by formation of C=C bonds, but with no pronounced loss of hydrocarbons from the surface.[159] Under ambient conditions, vacuum ultraviolet (VUV) radiation at 185 nm (7.2 eV) can be sufficient for generation of highly reactive atomic oxygen or hydroxyl radicals from air, which oxidize surface-bound organic molecules.[152,153] It has also been demonstrated that VUV radiation is sufficient for ionization or direct cracking of the C-C backbone of molecular monolayers.[151] However, the filtered UV source used in the present work, at 254 nm (4.9 *e*V), intentionally does not have the energy required for either direct generation of oxidizing radicals from air or for direct ionization of aliphatic chains, as evidenced by the stability of monolayers on *p*-type GaN and *n*- and *p*-type SiC. Indeed, we have observed that monolayer degradation on *n*-type GaN occurs under

illumination by above bandgap light with energies as small as 3.4 eV. Degradation of alkanethiol SAMs by near-UV illumination has also been observed and was primarily attributed to photo-oxidation of the thiol head-group rather than the aliphatic chain;[160,161] in the present case, the silicate interfacial binding structure is insensitive to similar processes. In the special case of $TiO_2$, rapid degradation of SAMs has also been extensively studied and is due to photocatalytic generation of hydroxyl radicals on the surface, followed by rapid oxidation of organic monolayers.[162–164] However, it has been shown that these radicals are highly mobile on the surface and can yield remote oxidation as far as 20 μm away from the generation site.[163,164] As demonstrated in **Figure 24** no loss of pattern fidelity is observed following selective illumination through a shadow mask, consisting of a dot array with 4 μm feature sizes, proving that an analogous process does not play a significant role in the present degradation mechanism.

In light of these observations, we propose a mechanism for photocatalytic degradation of ODS monolayers on *n*-type GaN based upon charge transfer between the highest occupied molecular orbital (HOMO) of the organosilane layer and the semiconductor valence band. **Figure 31a-d** show schematic diagrams of the proposed mechanism and corresponding energy level diagrams for *n*-type 6*H*-SiC and GaN. CPD/SPV measurements, calibrated using freshly exposed highly oriented pyrolytic graphite, reveal the surface valence band positions of GaN and 6*H*-SiC to be at -7.5 eV and -7.0 eV below the vacuum level, respectively. The upward surface band bending of *n*-type GaN and 6*H*-SiC, which is measured by SPV to be in the range of 0.4 - 0.5 eV for both materials, results in hole accumulation at the surface under UV illumination. The GaN valence band position, at -7.5 *e*V, is much lower than that of 6*H*-SiC, at -7.0 eV, and is in close alignment with reported values for alkyl chain HOMO levels.[165] We note that the typical method for determination of the HOMO level, ultraviolet photoelectron spectroscopy, could not be used in the present work since rapid UV-induced degradation would yield spurious results.[159] So, the value was therefore obtained from the literature.[165]

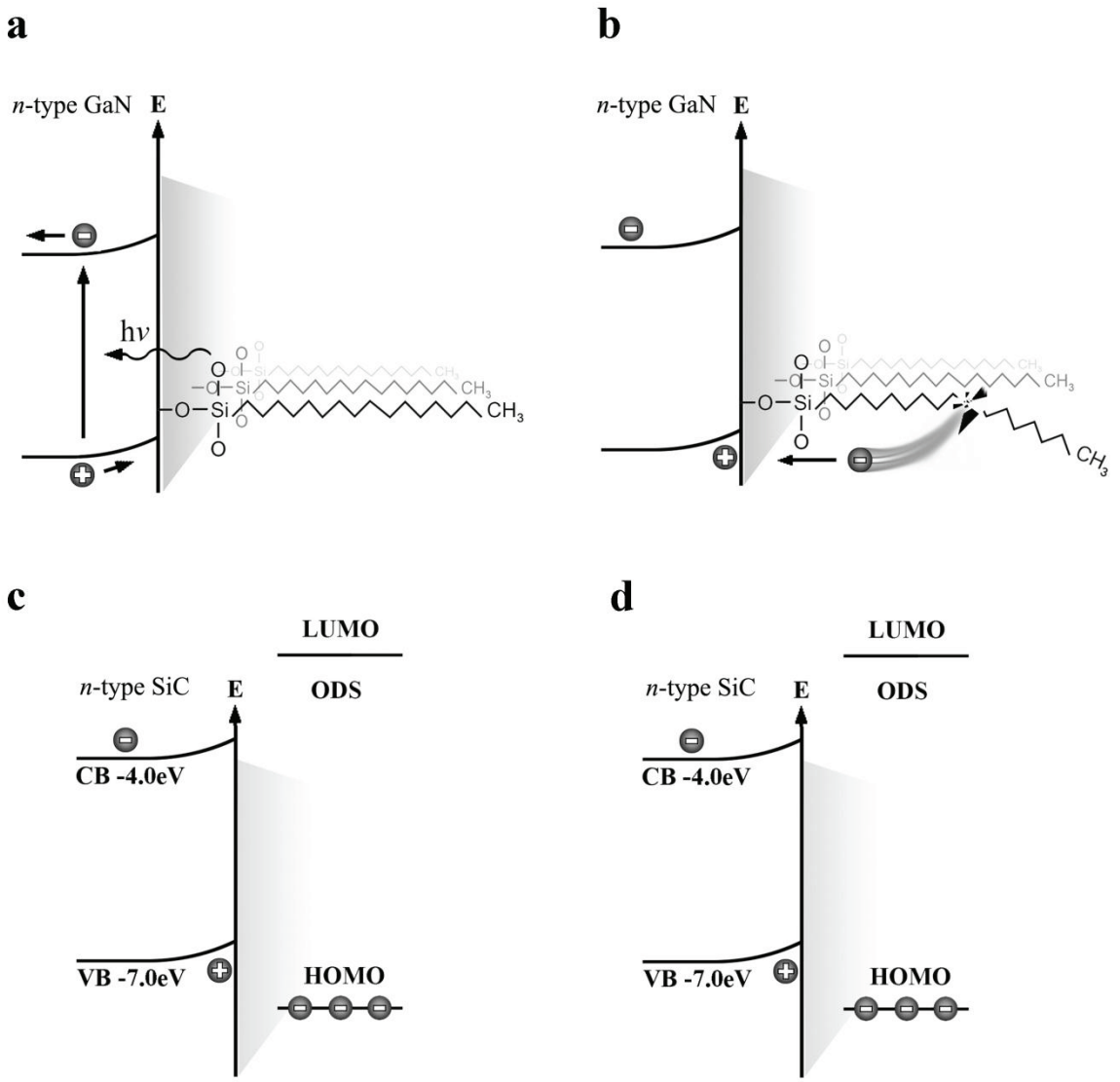


**Figure 31 | Band Diagram Explanation of the degradation Effect**. **a)** An ODS / *n*-type GaN interface is exposed to above-bandgap light and electron-hole pairs are generated. **b)** Photo-assisted recombination cleaves the chain of a previously stable molecule. **c)** *n*-type SiC band alignment does not allow the charge transfer to take place. **d)** *n*-type GaN has the correct band positions to allow the recombination.

This energetic alignment allows for UV-assisted electron transfer from the alkyl HOMO and recombination with a surface-accumulated hole in the semiconductor substrate. The loss of a bonding electron from the C-C backbone is analogous to excitation above the ionization energy and causes the molecule to crack or become very reactive, leading to the observed degradation. As a consequence, the energy threshold for this process is reduced to the GaN bandgap energy. In contrast, due to the downward band bending in *p*-

type GaN and SiC, UV illumination results in surface accumulation of electrons instead of holes. In the absence of recombination sites, the molecular monolayers are stable under UV illumination, independent of energetic alignment. It is, however, evident that an alternate model may explain the experimental findings. It has recently been reported that mid-bandgap states in *n*-type GaN facilitate water splitting.[166] Although a dominant role of these states in the UV-induced charge transfer is considered unlikely due to their comparably low concentration, the acceleration of the degradation process in the presence of water could indicate an indirect involvement that catalyzes the UV-induced degradation. For example, the charge transfer dipole would be significantly reduced due to enhanced screening in the presence of water. Referring to the water splitting mechanism,[166] electron transfer to the oxygen redox level of the adsorbed water film could enhance electronic transitions from shallow donor states to unoccupied defect states and, therefore, also the flux of holes drifting to the surface. Direct chemical reactions of hydrogen peroxide or non-radical hydroxide, being two of the possible products of water splitting, appears unlikely as these species are not reactive enough to cause chemical cracking of the alkyl chain. The proposed degradation mechanism describes the charge transfer-induced destabilization of SAMs on *n*-type GaN. Subsequent oxidation of this reactive intermediate state under ambient conditions is reasonable to expect and may be accelerated in the presence of water.

## 4.4 A New Analysis Showing the Impact of Immobilization on Enzyme Functionality

In this work SGHEMTs are used as an indirect detector in a two-step process. Here, enzymes, immobilized on the non-metallized gate area, catalyze a specific substrate-molecule through a biochemical reaction to form a detectable product.

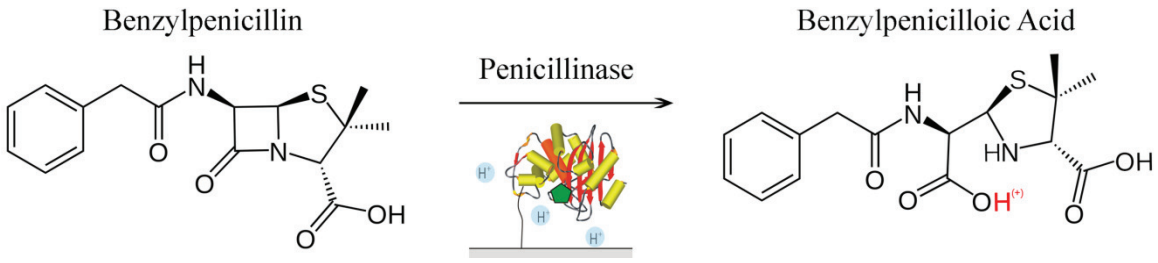


**Figure 32 | Catalytic Conversion of Penicillin.** The catalytic conversion of benzylpenicillin to benzylpenicilloic acid by the enzyme penicillinase.

If the reaction products are basic or acidic, the change of *p*H in the vicinity of a *p*H-sensitive gate area would lead to a variation in the gate potential of the underlying transistor. However, the evaluation of these parameters places significant requirements on the measurement system since it must be capable of controlling the environment of SGHEMTs in such a manner that very stable data is produced for analysis. To this end, an advanced electrochemical and environmental control system was designed and constructed to evaluate hybrid (bio)molecular systems consisting of penicillinase-modified SGHEMTs.

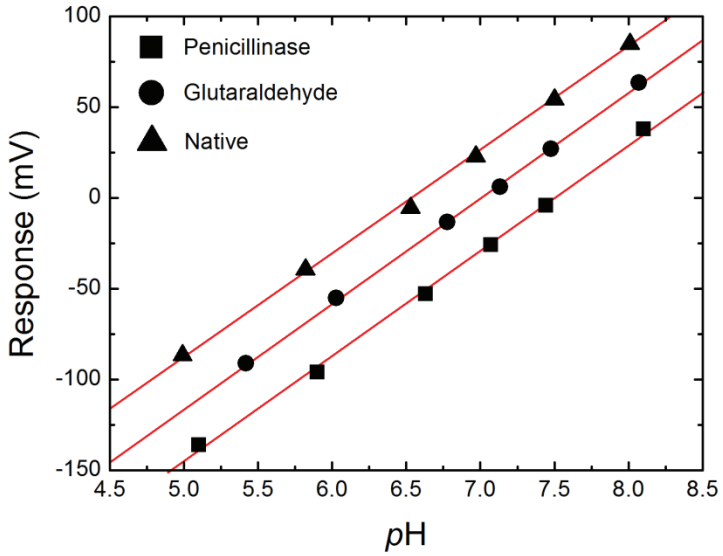


**Figure 33 | *p*H Characteristics of (Bio)Molecularly Functionalized SGHEMTs.** This figure shows the *p*H sensitivity for an SGHEMT with a native oxide, one with APS and glutaraldehyde, and one with the complete functionalization up to the enzyme penicillinase. All of the devices show a high and linear *p*H dependence of approximately 57.6 mV/*p*H due to an approximate 50% monolayer coverage.

For this project the enzyme penicillinase was chosen as a model system.[41,42] As illustrated in **Figure 32**, the dissociation constants of benzylpenicillin allow it to be titrated into a neutral solution without changing its *p*H. However, if the gate of a SGHEMT is functionalized with penicillinase, a local conversion of benzylpenicillin to benzylpenicilloic acid would create an acidic microclimate on the gate. By this method, the impact of the immobilization process on enzyme functionality could be investigated by the comparison of SGHEMTs prepared by covalent immobilization and by physisorption of penicillinase on the gate area of the devices. The experiments were carried out with SGHEMTs with gate dimensions of 1.2×0.5 $mm^2$ in a stirred 0.5 mM PBS solution containing 25 mM sodium chloride at *p*H 7.

Initial reference measurements were carried out to make sure that the devices were still capable of detecting a *p*H change according to the site binding model,[33,146,147] even when some sites are blocked by the functionalization molecules. This was achieved by titrating small amounts of the buffer solution containing high concentrations of hydrochloric acid or sodium hydroxide to give small changes to the *p*H of the bulk solution. The results are shown in **Figure 33** and compare:

- A device with its native oxide.
- A device functionalized up to and including the cross-linker (APS+glutaraldehyde).
- A device with the complete covalent binding procedure including the enzyme (APS+glutaraldehyde+penicillinase).

All three functionalization stages showed a similar *p*H sensitivity of 57.6 mV/*p*H. This is attributed to an approximatly 50% monolayer coverage,[15] which reduces both the ion sensitive sites and regulation sensitive areas by the same amount, allowing the device to not only retain its ion sensitivity but also a similar, but noisier, magnitude of the *p*H response.

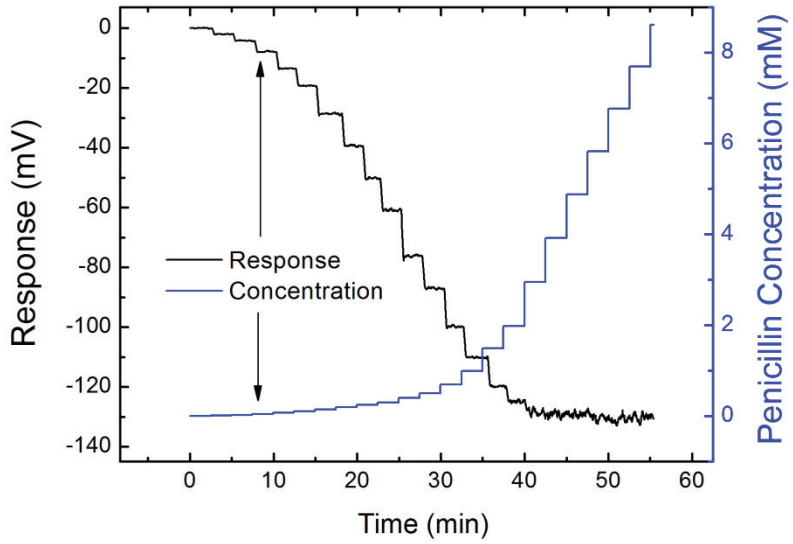


**Figure 34 | The Response of a Penicillinase-Modified SGHEMT.** The transient response of a stabilized covalently bound enzyme (penicillinase) modified SGHEMT (black line) to changes in the substrate-molecule concentration (benzylpenicillin) (blue line).

These (bio)molecularly functionalized ion sensitive SGHEMTs could now be characterized with respect to their response to benzylpenicillin. **Figure 34**, shows the response of a stabilized covalently bound enzyme modified (penicillinase) SGHEMTs to changes in the substrate-molecule concentration, by titrating buffer solution containing 200 mM benzylpenicillin. A monotonically increasing negative signal from -2 mV for 10 µM to -124 mV for 2 mM, due to benzylpenicillin-induced acidification in the vicinity of the gate area, was observed with saturation occurring above 3 mM. Simultaneous measurements of the bulk *p*H revealed a change from 7.07 to 7.02 which, with a sensitivity of 56 mV/pH, would corresponds to a gate voltage shift of 2.8 mV over the entire experiment. This is due to the slight acidification of the bulk solution from the benzylpenicilloic acid produced on the sensor surface.

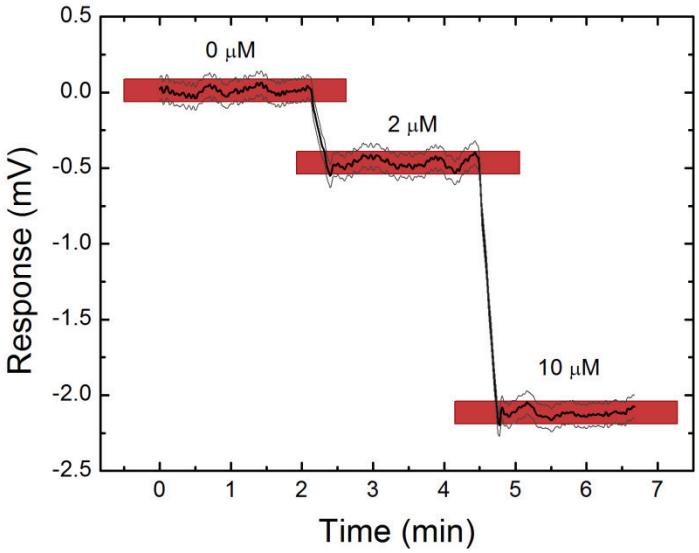


**Figure 35 | The Device Response for Low Substrate-Molecule Concentrations.** The red boxes indicate the manufacture-specified resolution limit of the digital-to-analogue converter employed for these measurements.

**Figure 35** displays the covalently bound enzyme-modified SGHEMTs response for low substrate concentrations, indicating that concentrations as low as 2 μM could be resolved with the measurement conditions applied here. While achieving higher resolutions from a systems standpoint might be possible (e.g. the height of the red boxes indicate the manufactur-specified limit for the data acquisition component of this system, which could easily be upgraded with a higher resolution unit) other variables, such as temperature, must be taken into account. For instance, the baseline noise calculated from this data is approximately 25 μVrms. If this should be calculated into temperature stability using the devices 18 mV/K temperature dependence found in **Figure 18**, it would correspond to requiring the variation of temperature to be of less than 1.4 mK.

With the response to benzylpenicillin being established, we can investigate the possibilities to analyze the functional differences of a bio-chemical system on the surface of the devices. To investigate differences in the ways the biochemical system catalyzes product formation, we chose to compare covalently bound enzymes to physisorbed enzymes. In **Figure 36** the SGHEMT response is shown as a function of substrate-molecule concentration for five different covalently enzyme-modified SGHEMTs and three physisorbed enzyme-modified SGHEMTs.

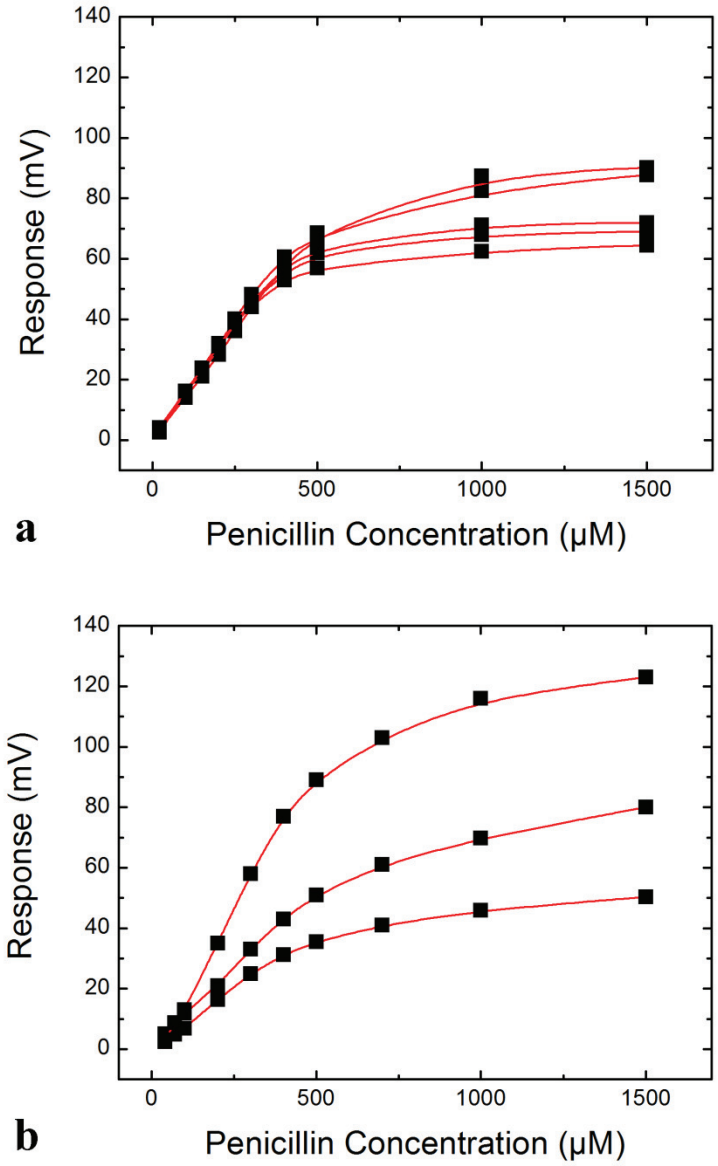


**Figure 36 | Difference Between Covalently Bound and Physisorbed Penicillinase.** The enzyme-modified SGHEMTs gate voltage dependence on benzylpenicillin concentration for **a)** covalently bound and **b)** physisorbed penicillinase.

For substrate-molecule concentrations below 300 μM, a reproducible linear response of 152±8 μV/μM was observed for the covalently enzyme-modified SGHEMTs, as can be seen in **Figure 36a**. For higher substrate-molecule concentrations, variations in the saturation signal were found. In contrast, the physisorbed enzyme-modified SGHEMTs (**Figure 36b**) show large variations in both the low and high concentration regimes, indicating poor reproducibility of the respective immobilization processes.

To explain this behavior it has to be considered that the enzymatic reaction can be described by the two steps in the following equation.[167]

$$A + S \underset{m_{-1}}{\overset{m_1}{\rightleftarrows}} AS \xrightarrow{m_2} A + P \qquad (14)$$

Here, the enzyme *A* and substrate *S* (i.e. substrate molecules, not wafer substrate) form a reversible intermediate enzyme/substrate complex *AS*, which can irreversibly decay into the enzyme reaction product *P*. Under steady state conditions this leads to the Michaelis–Menten kinetics, where the reaction rate has a linear dependence for small *S* concentrations and saturates for high *S* concentrations. $m_1$, $m_{-1}$ and $m_2$ are the equilibrium constants of the respective reactions. Here, the dissociation constant for *P* differs from that of *S*, consequently in the case of penicillinase leading to the release of a proton from the product in neutral *p*H solutions. For small amounts of *AS* in comparison to *A* on the gate surface, all incoming *S* can form *AS* complexes if a high *AS* affinity and turnover frequency exists. In this regime, the resulting amount of *AS* does not depend on *A* but is solely a function of the *S* concentration (affinity regime). If we further assume steady-state conditions, **Equation (14)** results in a linear relationship between the *S* concentration and the *P* concentration. For complete dissociation of the product, a logarithmic response of the SGHEMT would be expected. However, the linear dependence observed in **Figure 36a** is attributed to the influence of the *p*H-dependent buffer capacity, which has a maximum at *p*H 7.2, and to the weak acidity of the product with a $pK_a$ value of 5.2. This is because, for small *S* concentrations the change in proton concentration due to the enzymatic reaction is attenuated. That is, for increasing *S* concentrations the buffer capacity decreases and the resulting increase of proton concentration inhibits further dissociation of *P*. Therefore, the resulting linear slope of the response curve, as well as the resolution limit, is determined by the *AS* affinity, the *A* turnover frequency, the buffer concentration and $pK_a$ value. In addition, the SGHEMT signal is influenced by the diffusion rate of protons to the gate surface, which is attenuated for an increasing proton concentration at the gate. This effect was confirmed by a shift of the transition region between linear response and saturation to higher *S* concentrations with increasing buffer concentration (not shown). When the flux of *S* is larger than the amount the enzymes on the gate can catalyze into product per unit time,

the change in the product concentration is proportional to the gate enzyme density and turnover frequency of the catalytic reaction. This implies that the transition region, which is narrow for covalently enzyme-modified SGHEMTs, is shifted to a higher *S* concentration when the saturation signal increases, as visible in **Figure 36a**. Thus, it can be concluded that the covalent immobilization process shows a high reproducibility with respect to the *AS* affinity and varies in the density of immobilized enzymes. In contrast, physisorbed enzyme-modified SGHEMTs, **Figure 36b,** show a strong variation of the linear behavior for low substrate-molecule concentrations, a wider transition region, and a late onset of signal saturation. We attribute these effects to diffusion of the *S* and *P* through the enzyme multilayer.[168] The reason for the lower average slope for low substrate-molecule concentrations could be a lower *AS*, possibly due to geometrical hindrance in the physisorbed multilayer or due to structural deformation of enzymes in direct contact with the GaN surface. The higher average slope for one of the physisorbed enzyme-modified SGHEMTs can be caused by slow diffusion of the product away from the SGHEMTs surface, resulting in strong acidification of the buffer solution.

# 5 Photoresponse for Ionizing Radiation Dosimetry

In this chapter, we investigate the photoreseponse of advanced AlGaN/GaN heterointerfaces for ionizing radiation dosimetry and compare it to the response of GaN thin films. Here, we found new results exhibiting "photomultiplier" gains and independence of the well-known persistent photoconductivity for soft X-rays and high energy particles in the ultralow dose-rate regime. Furthermore, we study the multi-functional device capabilities of simultaneous bio(chemical) sensing and ionizing radiation dosimetry using single SGHEMTs and the possibility to provide dosimetry via optical detection of the yellow luminescence of irradiated GaN. We expand this work to include energies in the medical X-ray spectrum to support future studies of radiation effects on cell systems grown on the surfaces of devices. We found that their *p*H sensitivity was retained during X-ray irradiation and that the fundamental characteristics can be used to separate the irradiation signal from the *p*H response without compromising operational stability.

## 5.1 Spectral Dependence and Gain of HEMT Devices

In order to characterize the energy dependence and gain of a HEMT to the medical X-ray spectrum, multiple series of dose-rate-dependent transport measurements were performed. Later in this chapter, we use highly characterized focused radiation beams in the form of 20 MeV protons of the ion microprobe SNAKE at the Maier-Leibnitz-Laboratorium tandem accelerator,[123–125] and 1-20 keV monochromatic X-rays from the µSpot Beamline at the BESSY II synchrotron. For these systems the exponential power law, introduced in **section 3.5,** can be used to estimate the dose received by individual GaN layers and used to calculate the devices internal gain. However, in this section we use commercial medical X-ray systems with a fixed 40kV and an adjustable 50-300kV acceleration voltage.

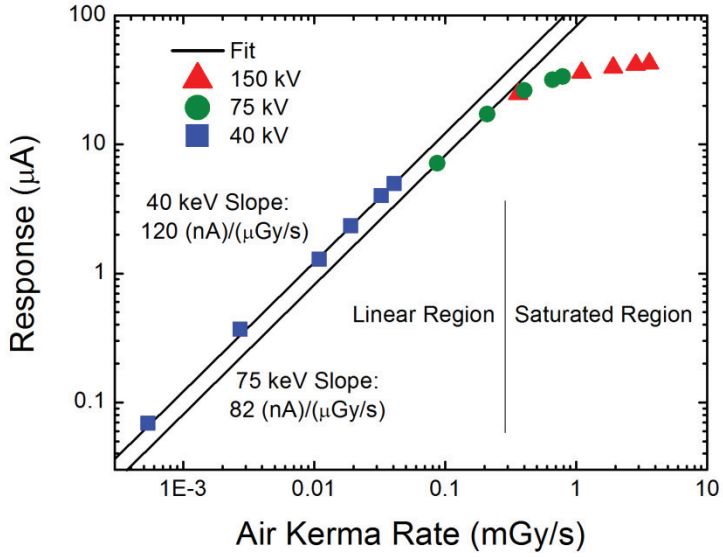


**Figure 37 | Device Calibration for X-ray Energy and Intensity.** Source-drain current of an AlGaN/GaN HEMT as a function of dose-rate for three different Bremsstrahlung energies. The 40 kV series uses a different source and filter set.

These X-ray sources have both broad energy and intensity distributions,[169] which rely on a single ionization chamber calibrated to give the total dose rate. So in order to find the gain of the GaN device, the spectral intensity distribution of the beam must be calculated, adjusted to the measured dose rate and used to find the devices spectral absorption profile so that the total absorbed energy can be found and used to calculate the internal gain. Here, the results from three different acceleration voltages from the two different filtered Bremsstrahlung-derived beams were used; the 40 kV system using a 4mm Al and 0.21mm Cu filter, and the 50-300kV system at 75 kV and 150 kV using a 4mm Al filter. Dose-rate-dependent transport measurements were then made by using the filtered beams to irradiate a device at different emission currents while measuring the photocurrent and the data used to calculate the gain. We note that the residual current, primarily a consequence of conduction through the open HEMT channel, of approximately 65 μA in darkness is subtracted throughout this section.

In **Figure 37**, a compiled source-drain current response of a device at a fixed source-drain voltage of 80 mV and a floating gate potential is plotted versus pulsed irradiations of 40 kV, 75 kV and 150 kV at various dose-rates. A monotonic increase of the source-drain current with X-ray dose-rate due to generation of photo-excited carriers is observed for

each series. The device ceases to have a saturated dependence for dose-rates below 0.3 mGy/s. However, it retains a noticeable energy dependence, as a difference in slope of 120 nA·µGy$^{-1}$·s$^{-1}$ and 82 nA·µGy$^{-1}$·s$^{-1}$ between the 40 kV and 75 kV data, respectively. The measurements correlate well for the same series of rising, falling and randomized pulse heights and have excellent reproducibility, without any noticeable permanent performance alteration after a total dose of several hundred Gy. Furthermore, apart from the higher dark current of the HEMT structure, devices with completely etched 2DEG channels, such that only the underlying GaN layers contribute to conduction, as well as carbon-compensated thin films, show similar X-ray sensing characteristics to that of the HEMT structure. Thus, the X-ray sensitivity is enabled by photoconductivity of the approximately 2.9 µm thick GaN-layer and does not require the presence of an AlGaN/GaN heterointerface. In comparison, MOSFET-based radiation detectors, which have become essential tools in radiology,[59,170–172] reach their detection limits in the low mGy region,[59,172] whereas the GaN devices could now expand this limit down into the nGy-regime.

To be able to discuss the energy dependence and intrinsic gain of the devices, including also the viability of using GaN beyond 20 keV, an appropriate model for the filtered Bremsstrahlung spectrum is required. This is because the only independent information obtained for the X-ray beams was the air kerma rate $K_{air}$, which is defined as the energy absorbed per kg of air per second (J·kg$^{-1}$·s$^{-1}$). Therefore, it lacks information about spectral distribution and irradiated area, two quantities that have to be compensated for theoretically. Since all of the used source output intensities were attenuated, the 150 kV and 75 kV spectra were obtained on the same system with a 4 mm Al filter and the 40 kV spectrum was filtered by 4 mm of Al and 0.21 mm of Cu, a suitable description of the intensity reduction is needed. The exponential power law, **Equation (11)**, was used to calculate the relative intensity transmission through these filters using mass attenuation coefficients obtained from the photon cross-section database,[150] as

$$\frac{I_f(\omega)}{I_{f0}(\omega)} = \exp\left(-\sum_n (\kappa(\omega)\cdot\rho\cdot x)_n\right) \qquad (15)$$

The mass attenuation coefficients are explicitly defined to represent narrow beams of monoenergetic photons. As a consequence of using them to describe a complete spectrum, we consider the monoenergetic portions to represent the partial photon energy spectrum $d\omega$, and thus can only be considered as an approximation. Furthermore, the intensity $I$ and the mass attenuation coefficient $\kappa$ are spectrally dependent, thus being represented by $I(\omega)$ and $\kappa(\omega)$, respectively.

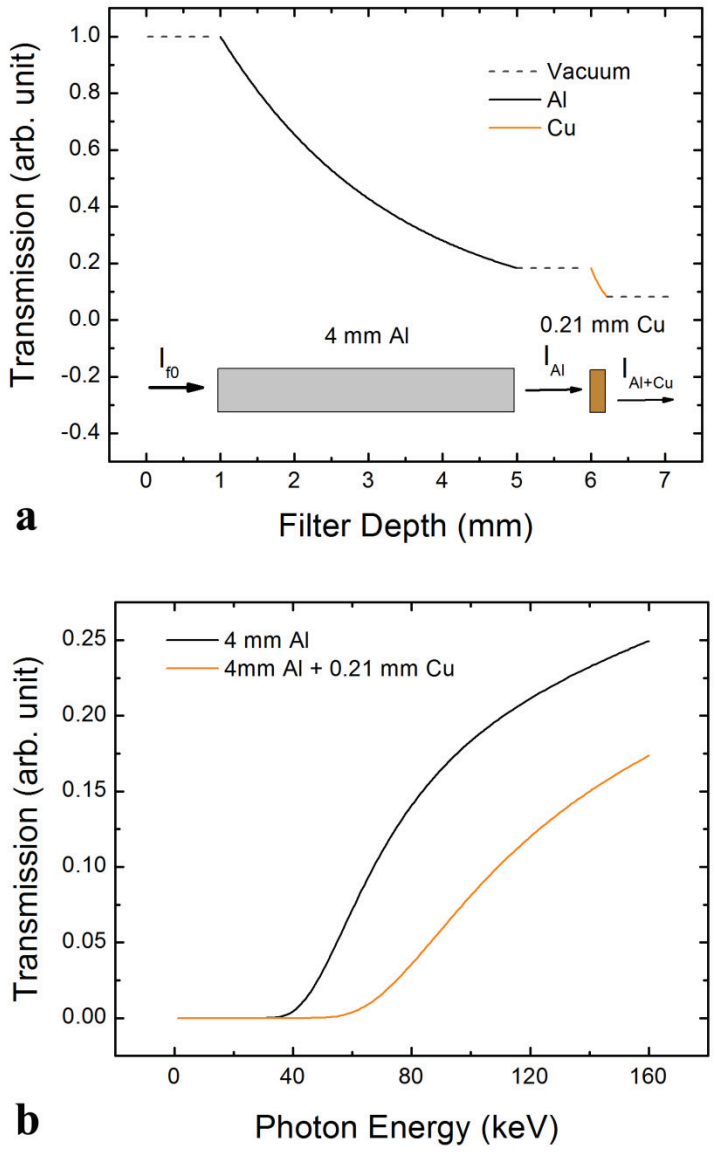


**Figure 38 | Model of Radiation Attenuation Through a Filter Set. a)** The 100 keV photon intensity as a function of transmission length through 4 mm of Al and 0.21 mm of Cu. **b)** The transmission as a function of photon energy after the 4 mm Al filter or the 4 mm Al plus 0.21 mm Cu filter.

Using **Equation (15),** the relative transmission of photons through the filter set was calculated and can be seen for 100 keV photons in **Figure 38a**, where the reduction of the sources output intensity $I_{f0}(\omega)$ is plotted as it first propagates through 4 mm of Al followed by 0.21 mm of Cu. Using this information, the relative spectral transmission through the two filters, 4 mm of Al, and 4 mm of Al and 0.21 mm of Cu, can be calculated and is shown in **Figure 38b**. However, the established filter characteristics are shown for a constant source output intensity $I_{f0}(\omega)$ across the entire spectrum and an estimation of how the real intensity $I_{f0}(\omega)$ behaves is needed. It is an accepted approach to assume that an unfiltered Bremsstrahlung spectrum in vacuum has a linear relationship with intensity. Material specific transmission lines can be disregarded since the eventual application of the correct filters will significantly reduce their intensity. This linear spectrums intensity, illustrated in **Figure 39** for a source set to 150 kV, will cease and become zero at voltages higher than the acceleration voltage, which directly corresponds to the maximum photon energy, but will increase for decreasing voltages. Multiplying this relative source intensity $I_{f0}^{*}(\omega)$ with the calculated filter spectrum gives a relative transmission spectrum $I_{f}^{*}(\omega)$ (**Figure 39**) that, since the source output spectra is not known, needs to be correlated against the air kerma rate measurements made by the different systems ionization chambers after the filters.

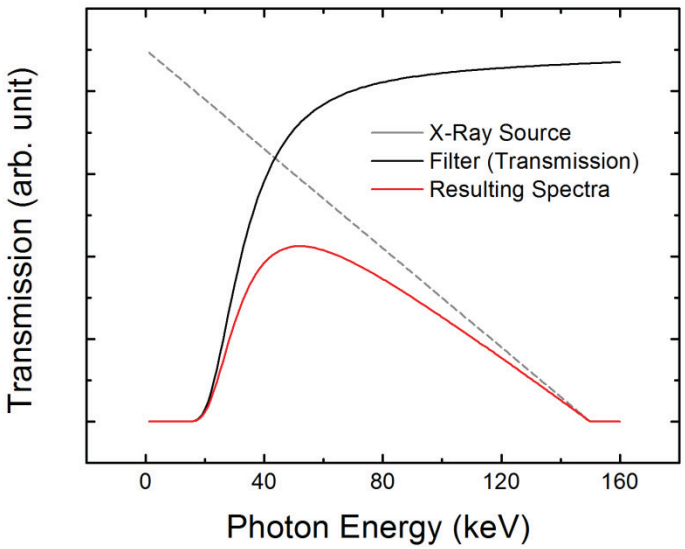


**Figure 39 | Model of a Filtered Bremsstrahlung Spectrum.** The resulting Bremsstrahlung spectrum (red line) after combining the filter calculation (black line) with the source output estimation (gray dashed line).

Since the only independent information obtained for the X-ray beam after the filters is the air kerma rate, $K_{air}$, the relative air absorbance after the filters was calculated from **Equation (15)** by using the relative Bremsstrahlung spectrum, as

$$Q^*_{air}(\omega) = I^*_f(\omega) \cdot \underbrace{\left(1 - \frac{I_{air}(\omega)}{I_{air\,0}(\omega)}\right)}_{absorption} \qquad (16)$$

The dependence of the air kerma rate on mass can be recalculated to area, through the density of air and the 3 μm thickness used in the calculation to match the GaN thin film, giving the measured air absorption, $Q^M_{air}$ ($J \cdot m^{-2} \cdot s^{-1}$), as

$$K_{air} \cdot \rho_{air} \cdot x_{air} = Q^M_{air} \qquad (17)$$

The measured air absorption $Q^M_{air}$ can be set equal to the integral of the relative absorption $Q^*_{air}(\omega)$ over the spectrum multiplied by a factor $R$, as

$$Q^M_{air} = R \cdot \int Q^*_{air}(\omega)\, d\omega = \int Q_{air}(\omega)\, d\omega \qquad (18)$$

We note that, the photon energy and intensity dependencies of the detector must be taken into account, since the instruments were not recalibrated between the 75 and 150 kV measurements. Now a corrected value of the energy absorption in air, $Q_{air}(\omega)$, can be obtained through

$$R \cdot Q^*_{air}(\omega) = Q_{air}(\omega) \qquad (19)$$

and recalculated through **Equation (16)** to the spectrally dependent intensity after the filters so that the Bremsstrahlung spectrum of data plotted in **Figure 37** can be recreated and plotted in **Figure 40a**. The accuracy of these spectra can now be partially determined, since the specifications of the 40 kV source listed a calibrated mean photon energy of 33 keV after the filters. Here, the data shown in **Figure 40a** is in excellent agreement, predicting a mean photon energy of 33 keV. This, now plausible, representation of the transmission spectra can be used to calculate the intensity absorption characteristics of a typical 3 μm thin film of GaN.

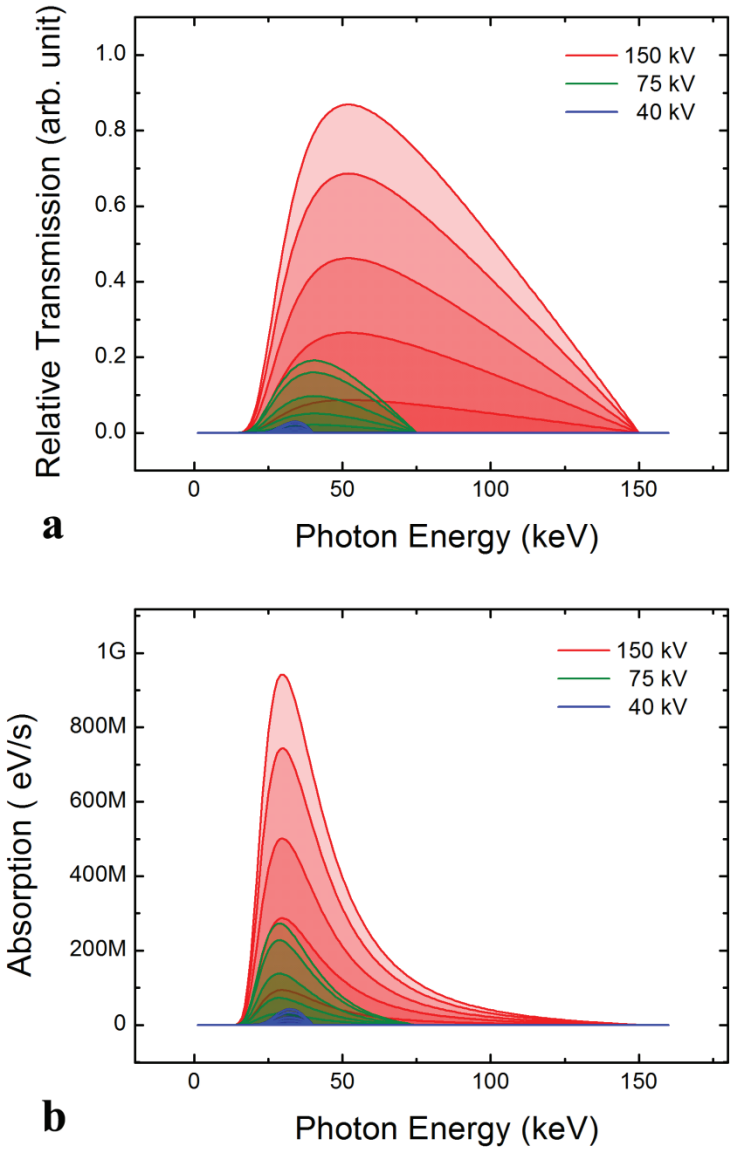


**Figure 40 | Calculation of the Absorbed Dose in GaN.** The same color lines represent different emission currents **a)** The calculated Bremsstrahlung intensity spectra after being transmitted through 4 mm of Al for the 150 kV and 75 kV acceleration voltages and 4 mm of Al and 0.21 mm of Cu for the 40 kV acceleration voltage. **b)** The spectral absorption of energy per GaN device volume.

However, once the exponential power law is used here, we must observe that it only is valid for narrow beams of monoenergetic photons and the result only represents material changes in one dimension. As we are considering an irradiated area, the difference in material area density is missing and the fraction $\rho_{GaN}/\rho_{Air}$ is needed to represent the change in density, as

$$Q_{GaN}(\omega) = \frac{\rho_{GaN}}{\rho_{Air}} \cdot I_f(\omega) \cdot \underbrace{\left(1 - \frac{I_{GaN}(\omega)}{I_{GaN\,0}(\omega)}\right)}_{absorption} \tag{20}$$

This equation can now be used to calculate the spectrally dependent absorption of the output intensity of the source (**Figure 40a)** by the device, and is plotted in **Figure 40b**. Here, it is apparent that a significant fraction of the original spectrum, especially the high energy portion, is not absorbed. Furthermore, there is a very different distribution, with peaks at 28.5 keV for 75 kV, 29.7 keV for 150 kV, and the highest energy peak of 32.2 keV for the lowest acceleration voltage of 40 kV. We note that this is caused by the different filter sets, systems and intensities. From this, the total energy absorbed in a GaN device can be obtained from **Equation (20)** by integrating it over the photon frequency, as

$$Q_{GaN} = \frac{\rho_{GaN}}{\rho_{Air}} \cdot \int I_f(\omega) \cdot \underbrace{\left(1 - \frac{I_{GaN}(\omega)}{I_{GaN\,0}(\omega)}\right)}_{absorption} d\omega \tag{21}$$

Since the ratio between the spectral absorption for GaN, $Q^*_{GaN}(\omega)$, and for air, $Q^*_{air}(\omega)$, stays the same for an X-ray source where only the intensity is modulated (i.e., changing the emission current and not the acceleration voltage), the following equation can be used

$$K_{GaN} = K_{air} \cdot \frac{Q^*_{GaN}}{Q^*_{air}} \tag{22}$$

The resulting energy per area per second or energy per mass per second for **Equations (21)** and **(22)**, respectively, can be recalculated to represent the device area or mass, the energy converted into eV, and then dividing by the ionizing irradiation electron-hole pair formation energy of GaN, which is typically assumed to be on the order of three times the bandgap, or approximately 10 eV. This represents the number of electric charges excited per second and can be converted into Coulomb per second (electric current) and be used to find the gain of the devices.

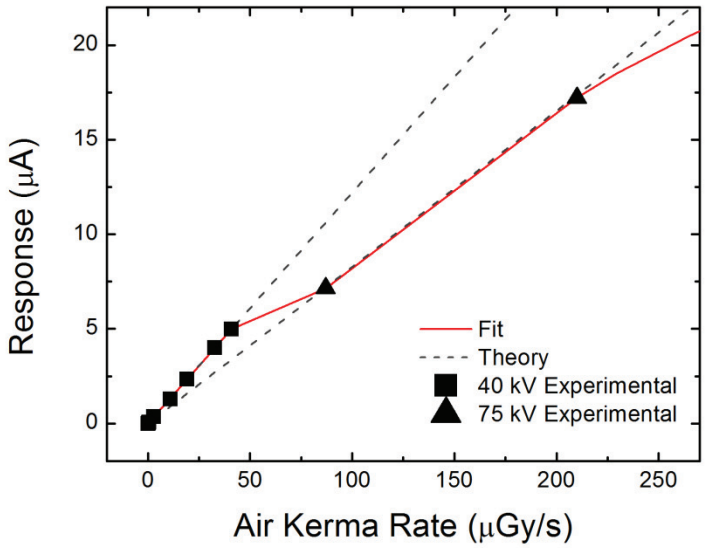


**Figure 41 | Energy Dependence of a GaN Device.** The calculated response from the 40 kV X-ray source (dashed line) needed to be multiplied with (the gain of) $7 \cdot 10^2$ to fit the experimental data (squares). Using this gain, the calculated response from the 75 kV X-ray source (lower dashed line) fit very well to the experimental values (triangles) showing the energy dependence and validity of the model.

The response of a semiconductor photodetector can be evaluated in terms of its quantum efficiency, $\eta$, and photoelectric gain, $g$, where $\eta$ and $g$ are defined as the number of electron-hole pairs generated per incident photon and the number of carriers passing the contacts per one generated pair, respectively.[173] Here, we use the 40 kV spectrum, due to the linearity of the experimental data, and find the ratio between the calculated amount of generated electrons per second for each air kerma rate and the corresponding experimental data showing the amount of electrons measured per second. This ratio gives, by definition, the photoelectric gain, and was found to be $g \approx 7 \cdot 10^2$ carriers passing the contacts for each generated electron-hole pair produced by an incident (spectrally representative) photon for a 80 mV source-drain voltage. The experimental data and the theoretical values multiplied with the gain are plotted in **Figure 41**. The experimental data show a higher slope for the 40 kV spectra than for the 75 kV spectra, prior to going into device-dependent saturation. Although the fit was generated with data from the 40 kV series, the model predicts the relative changes of the 75 kV data, supporting the validity of the theoretical model and showing the devices dependence on photon energy.

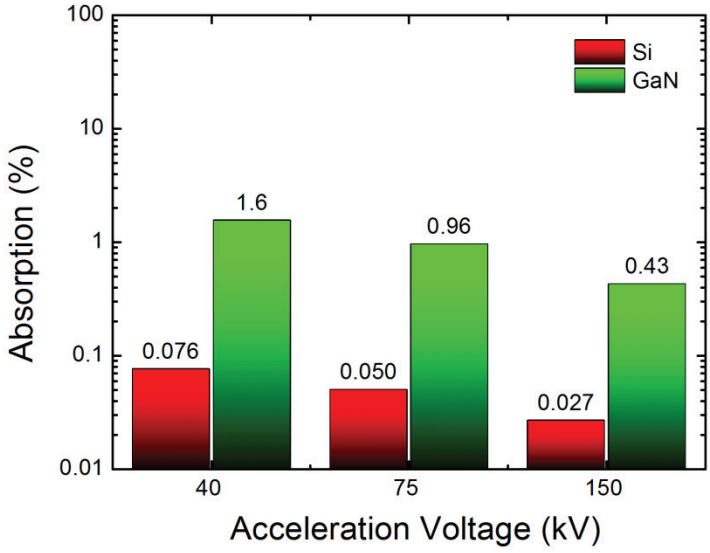


**Figure 42 | Comparison of Absorption for GaN and Si.** The relative absorption of energy from the incoming Bremsstrahlung spectrum after the filters ($I_f$) is compared for GaN and Si.

The larger slope, or device sensitivity, of the 40 kV source can be explained by the model as the influence of its much narrower spectral distribution in a highly absorbing region. Little additional analysis is possible for the 150 kV spectrum with regard to this model, since its first data point is well into the nonlinear response region. Furthermore, while it might seem from, for example, **Figure 40b** that GaN has a large energy absorption in this X-ray spectrum, it must be noted that most of the energy is transmitted. To get a clear picture of by how much, the absorption of $I_f$ in percent for both GaN and Si is presented in **Figure 42**. Even for the 40 kV spectrum, only 1.6% of the incoming energy is absorbed. However, since the device is only operated at 80 mV, it should be possible to increase the gain by several orders of magnitude by increasing the source-drain voltage. In contrast, Si has a much smaller absorption at these energies, but a 20 fold increase of film thickness would provide equal absorption and can exhibit gains of $g \approx 10^5$ configured as a photomultiplier (SiPM).[61] However, as will be discussed in the next section, we found that the 2DEG channels of HEMT structures can be used to radically increase the performance of the device.

## 5.2 Novel Simultaneous Solution-Gate and Dosimeter Single Device Sensors

In addition to the characterization of X-ray response with a floating gate, we show that the transistors retain their sensitivity to potential changes at the GaN surface during irradiation with a solution-gate. **Figure 43a** shows the source-drain current as a function of the gate voltage for a constant source-drain voltage of 120 mV. The transistor was characterized at *p*H 4, *p*H 7 and *p*H 10, before, during and after X-ray irradiation with a dose-rate of 2.9 mGy/s at 150 kV. The devices display high reproducibility through multiple radiation/calibration cycles, showing that the devices do not degrade with negative gate voltages, even in basic environments that are known to etch GaN under anodic conditions, though not the cathodic conditions used in this work.[174] The *p*H dependence is similar in both the non-irradiated and irradiated cases. It can also be seen that the irradiation response is mostly independent of the SGHEMT structure, as each complete characteristic curve is offset to higher currents during irradiation. This radiation dependent offset could be used under negative gate biasing below the threshold potential, at -3.5 V, to make dosimetry measurements with small dark currents. Moreover, since the irradiation increases the current, shifting the characteristic curve in the vertical direction, and the *p*H changes the voltage offset, shifting the characteristic curve in the horizontal direction, it should be possible to separate the two shifts from each other. However, since both the irradiation and the pH changes the current, recording the surface potential for constant source-drain currents cannot distinguish between the effects and a fundamental characteristic of the SGHEMT, such as the maximum transconductance, is needed as a regulation variable. In **Figure 43b**, the first derivative of the data in **Figure 43a** is plotted. Here, the position of the derivatives maximum on the gate-drain voltage axis stays in approximately the same position during irradiation and in darkness, but shows the voltage offset caused by changing the *p*H of the solution gate. Countering the *p*H-induced voltage shift with the gate-potential implies that any change in current should be representative of the photoresponse.

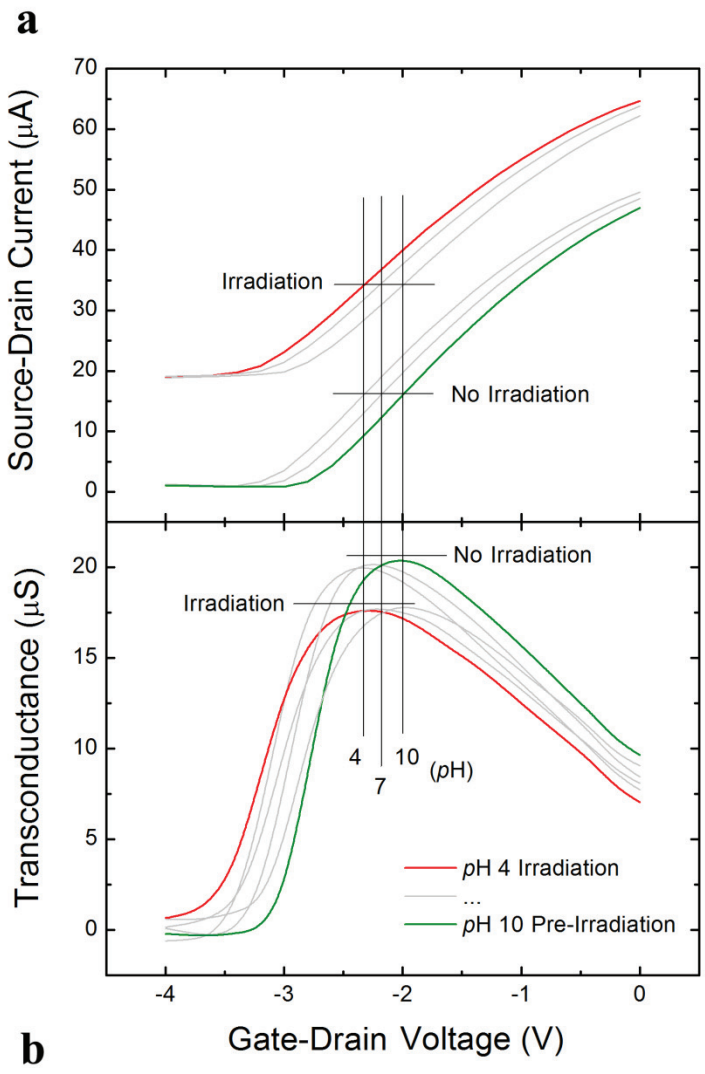


**Figure 43 | Radiation-Dependent Characteristics of a SGHEMT.** A GaN device in solution before, during and after X-ray irradiation with a dose rate of 2.9 mGy/s at *p*H 4, *p*H 7 and *p*H 10. **a)** shows the source-drain current-voltage curves in comparison to the first derivative or transconductance in **b)**. The gray lines show the intermediate data of the two extremes represented by red and green lines.

There is, however, an interesting occurrence: for some devices the transconductance maximum is smaller during irradiation. Moreover, the threshold potential seen between -3 and -4 volts in **Figure 43b**, another fundamental characteristic of the HEMT that could have been used to track the surface potential offset, is rendered exceptionally difficult to use for regulation by this phenomenon. We note that persistent photocurrent and the charge transport across the semiconductor solution interface will interfere with these measurements. A deeper analysis of this effect is presented in **Figure 44**.

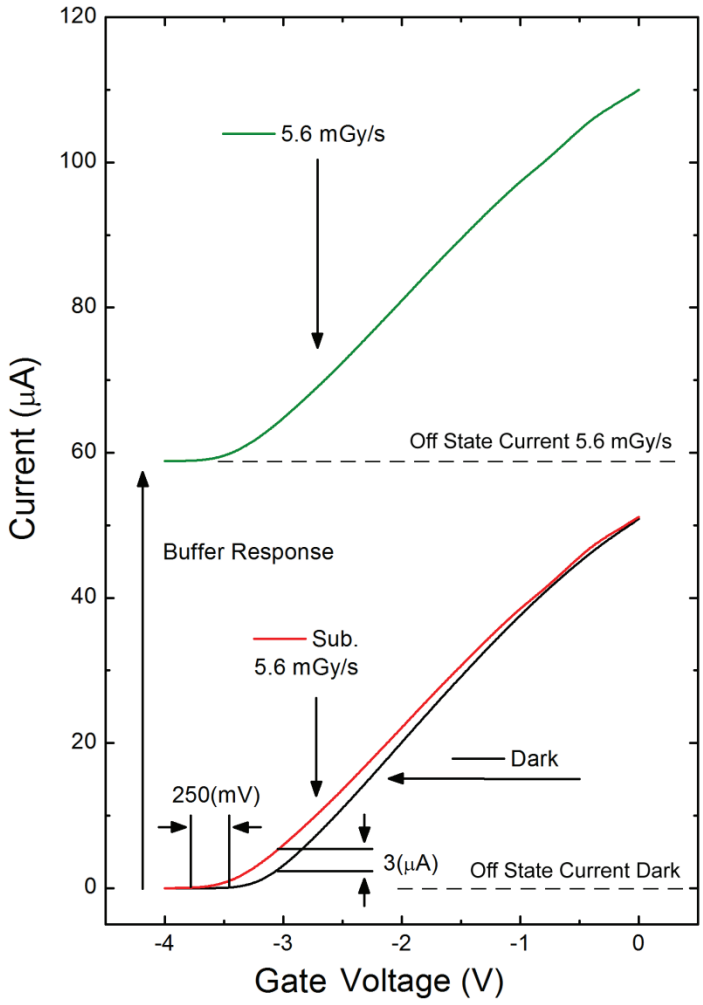


**Figure 44 | A Possible Response from a SGHEMT 2DEG Channel. a)** A comparison of the source-drain current as a function of the gate-drain voltage in darkness (black), under homogeneous 150 kV Bremsstrahlung irradiation of the gated channel (green), and subtraction of the off-state current from the illuminated curve (red).

Here, the source-drain current response versus applied gate-drain voltage in darkness is plotted and is characterized by a threshold potential of approximately -3.5 V. Homogeneous 150 kV illumination of the gated device leads to a vertical shift of the curve which is primarily due to the photoconductive response of the GaN buffer layer. However, a plot of the response of the irradiated device, after subtracting its off-state current, reveals an additional horizontal shift along with a slight change of slope compared to the device measured in darkness. The resulting threshold potential shift of approximately 250 mV provides an indication that the device response is not purely

photoconductive when an AlGaN/GaN heterointerface is present. Furthermore, when this threshold shift is plotted as a function of the air kerma rate, it is almost completely saturated for all dose-rates. This provides the indication that this effect is likely to be highly sensitive in the ultra-low dose-rate regime. This mechanism will be discussed in detail in the next sections.

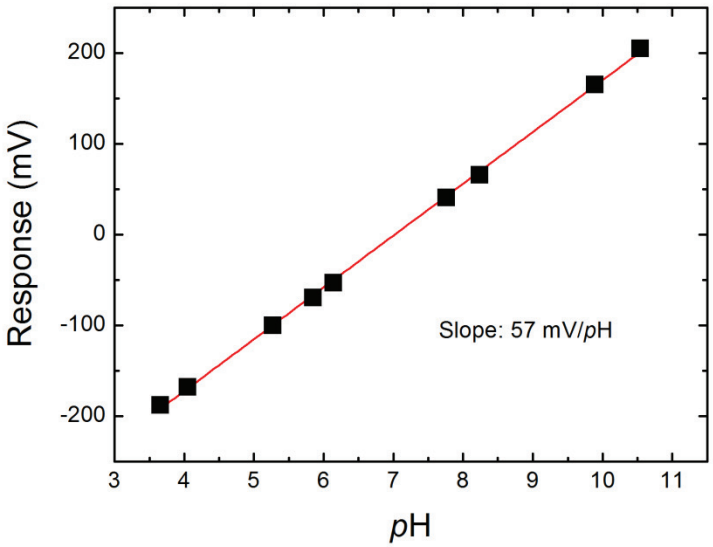


**Figure 45 | *p*H Dependence During Irradiation.** Titration during a continuous irradiation with 150 kV X-rays at a dose-rate of 1.4 mGy/s. The *p*H response is linear and yields a transistor sensitivity of 57 mV/*p*H.

Nevertheless, the photoconductive buffer layer response dominates the total current in this dose-rate range. In order to ascertain whether a radiated device would linearly respond to *p*H in a similar manner as the non-radiated devices reported elsewhere,[31] a transistor was continuously irradiated in an aqueous solution while the *p*H was varied by titration. To gain the surface charge difference per *p*H, the constant source-drain current mode of the electrochemistry system described in **Sections 2.4** and **3.3** was used with a constant source-drain voltage of 120 mV. The regulated changes of the gate voltage are plotted as a function of the output from an X-ray shielded *p*H electrode in **Figure 45**. The slope, corresponding to a *p*H sensitivity of 57 mV/*p*H, was extracted by linear regression. We note that the in-going drift, caused by persistent photoconductivity, was subtracted from this data. This value is comparable to the sensitivity of 56 mV/*p*H without radiation[31] and differs as a consequence of a slightly elevated operational temperature, since our experiments were performed at room temperature while the others were

controlled to 20 °C. We note that the dose-rate of 1.4 mGy/s inside the electrolyte solution was determined using the internal self-calibration curve of the GaN-device signal response in air shown in **Figure 37**.

## 5.3 Separation of the Buffer Response from the Heterostructure Response

One of the most compelling hints for a response of the 2DEG channel, shown in more detail in **Figure 44**, was that the response of the X-ray irradiated device, after subtraction of its off-state current, possesses an additional horizontal shift along with a slight change of slope compared to the device measured in darkness. In order to independently characterize the contribution of the device response associated with this change of the threshold potential, the ultra-low dose-rate regime was investigated.

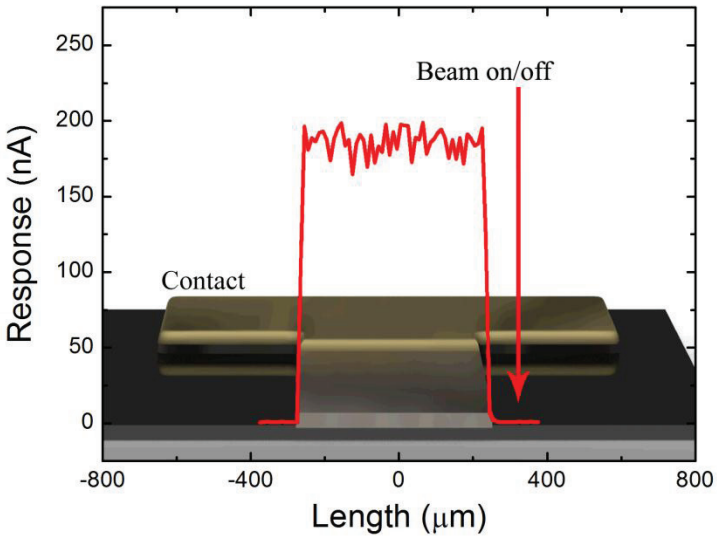


**Figure 46 | HEMT Response to Focused X-rays.** The photon-induced current, at 100 mV source-drain voltage and $10^6$ Hz photon flux, yielding a response of approximately 200 nA, as a function of position. Successive forward and backward scans verified that the signal remained reproducible in magnitude and symmetry, independent of scan direction. The shape of the response matches the known geometry of the mesa structure. No response was detected from the buffer layer, including during turn-on and turn-off of the beam.

This was achieved in two separate sets of experiments, the first by 1-20 keV X-ray irradiation and the second, which independently confirmed the results shown here, by 20 MeV proton irradiation.[123–125] For both cases, micron-sized spots allowed for *in-situ* mapping of the device response as a function of position on the active channel. The devices were operated without additional cooling at room temperatures. As illustrated in **Figure 46**, a 3 μm diameter beam of 1-20 keV synchrotron X-ray radiation, shown here at 7 keV, produces a current on a 500 μm wide device that is unexpectedly large compared to the direct charge extraction predicted by the energy deposition in the GaN film. Moreover, the scan indicates that the devices are over-dimensioned and would remain operational to much smaller sizes. The bi-directional scan across the active area reveals that the response is symmetric, reproducible in magnitude and in agreement with the known width of the mesa structure. Importantly, there was no evidence of a response from the buffer layer, despite the fact that both the contacts and scan were wider than the active channel. This observation was verified by placing the beam outside the active area, but between the contacts, and repeatedly switching the beam on and off, thus confirming that the observed signal is dependent only on the characteristics of the AlGaN/GaN heterostructure, which is located within the mesa region.

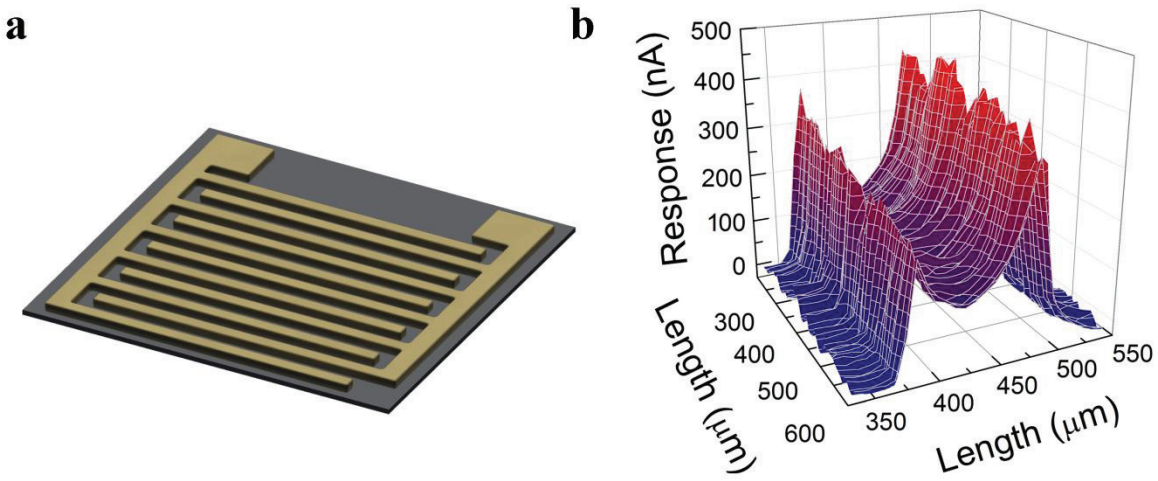


**Figure 47 | Interdigitated Electrode GaN Buffer Response to Focused X-rays. a)** An illustration of a typical interdigitated electrode. **b)** The response of a traditional interdigitated electrode device based on a highly resistive iron-compensated GaN thin film is provided for comparison. In order to obtain a similar current response from this device, a $10^3$ times larger source-drain voltage of 100 V and $10^5$ times larger photon flux of $10^{11}$ Hz was required.

In order to provide a representative comparison of the response of this device to a more traditional structure, a photoconductive GaN dosimeter was fabricated by deposition of interdigitated electrodes on a highly resistive iron-compensated GaN thin film. As shown in **Figure 47**, a photoconductive response from the device was observed between the metallic contacts. However, in order to obtain a response equivalent to that of the HEMT structure, it was necessary to increase the source-drain voltage by a factor of $10^3$, from 100 mV to over 100 V, while simultaneously increasing the photon count rate by a factor of $10^6$, from $10^5$ Hz to $10^{11}$ Hz. As will be discussed below, the strikingly higher sensitivity of the AlGaN/GaN device is a direct consequence of the presence of the 2DEG channel.

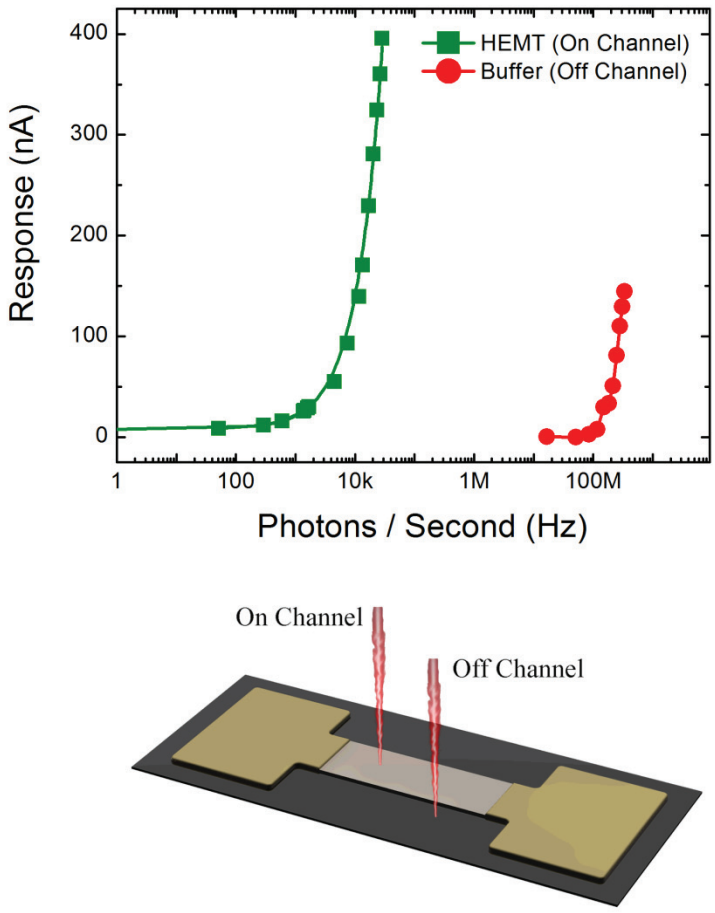


**Figure 48 | Separating the HEMT Response from the GaN Buffer Response.** A comparison of the current response as a function of photon intensity on and off the channel of the HEMT, accompanied with an illustration showing typical on- and off-channel beam positions. The threshold intensity for a detectable response is $10^5$ higher for the buffer layer compared to the HEMT device.

A comparison of the response on and off the channel, as a function of the incident photon count rate, revealed that the signal arising from the HEMT can be separated from that generated within the nominally undoped GaN buffer layer, as shown in **Figure 48.** The threshold for response of the buffer layer, which occurs at a $10^5$ larger photon flux than for the HEMT device, was also similar to that of the inderdigitated electrode.

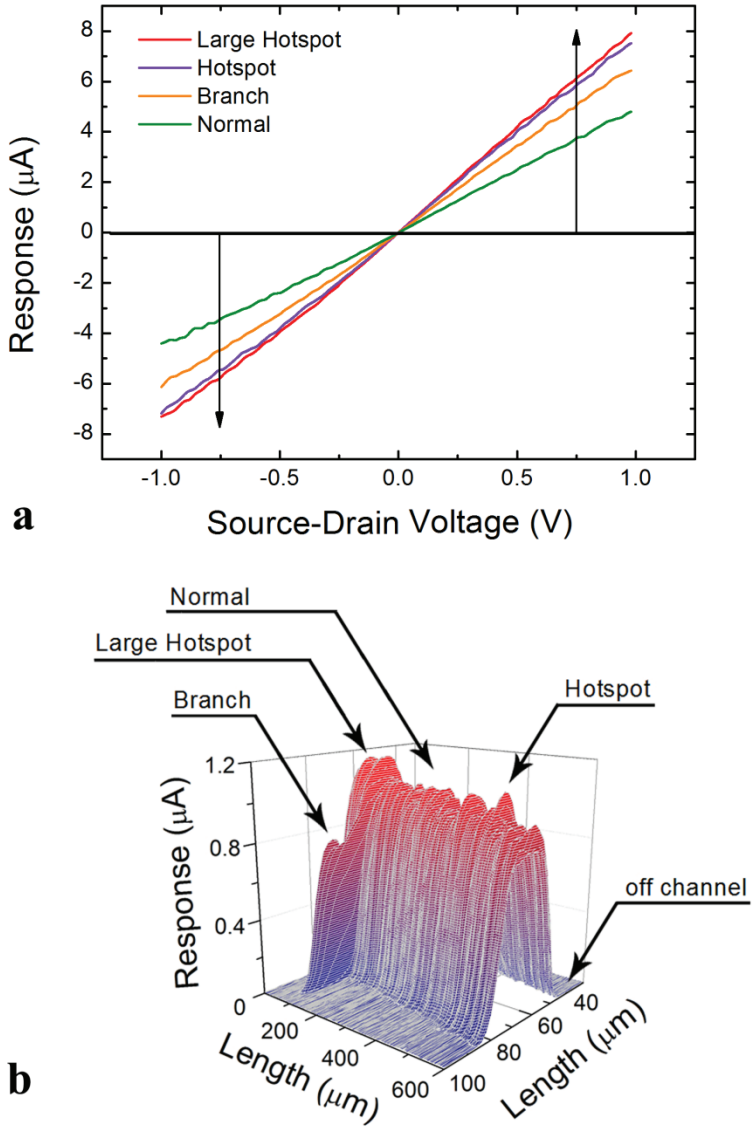


**Figure 49 | Source-Drain Voltage-Dependent Response of HEMT Devices. a)** The dependence of the photon response on the source-drain voltage reveals a linear behavior between ±1 V, where local hotspots cause a reproducible change in current which is shown in **b)**.

**Figure 49** shows the photon response as a function of source-drain voltage for a 20 μm wide floating gate device. For this device, ohmic behavior was retained well beyond the measurement window shown here of ±1 V and there was no detectable difference between subtracting the dark or the off-channel current, verifying that no contribution from the buffer was measured in this potential range. This gives an additional factor of over 10 in gain or a total intrinsic gain in the range of $10^7$, which is calculated in **Section 5.4**, for higher voltages than the set point of 100 mV used in this work for analysis of the response to photon (proton) irradiation. We note that, if the gain continues to linearly follow the transistor characteristics, this would allow for the gain to reach approximately $10^9$ as these devices were still ohmic at ±10 V. Furthermore, several different beam positions were characterized, exhibiting different current values for different beam positions as shown in **Figure 49b**. Moreover, the current for each position was highly reproducible and the two-dimensional current map in **Figure 49b** shows the different positions used for the calibrations. This effect was only observed for devices with thin channels and is most likely produced by changing magnitudes of band bending across the surface of the floating gate due to, for example, lateral confinement, varying lateral damage, differing degrees of oxidation, or subsurface defects such as dislocations or roughness at the 2DEG wall interface. This indicates that a gate-potential dependent change of the gain of the device should be possible. Here, either a photoconductive response, which would be similar to the buffer response and offset the entire calibration curve to lower resistances, or a photovoltaic response, which like the *p*H response would shift the entire calibration curve along the gate-drain voltage axis, would be expected. As we will show, this system has both in almost equal measures in dependence on if the beam, when it is on the channel, is on or off the gate contact area. **Figure 50a** gives the gate-drain voltage-dependent response under X-ray illumination for the on-gate irradiation position.

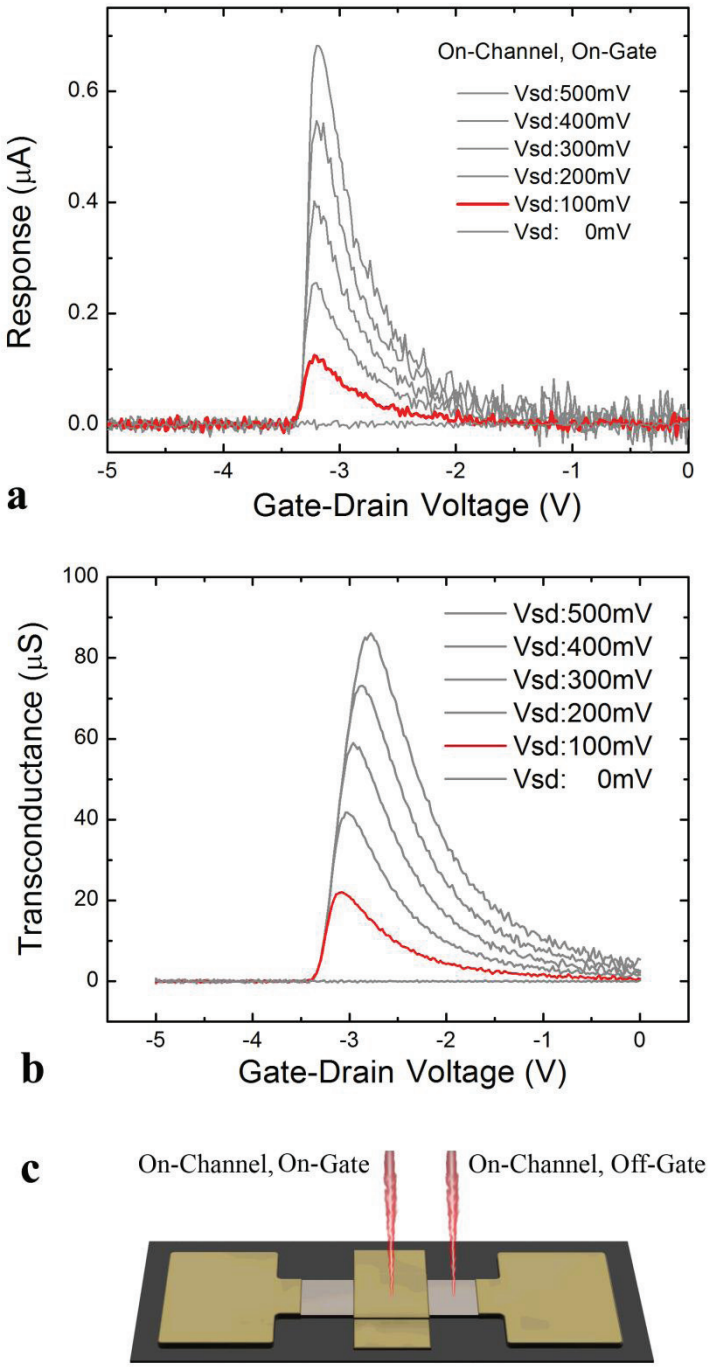


**Figure 50 | HEMT On-Gate Irradiation Response as a Function of Gate Voltage. a)** The "on-gate" irradiated source-drain current response as a function of gate-drain voltage under 7 keV X-ray illumination. b) The transconductance as a function of gate-drain voltage in darkness. **c)** An illustration of the on- and off-gate beam positions.

The close correlation between the transconductance of the device in darkness and its on-gate current response to ionizing radiation, that can be seen by comparing **Figure 50a**

with **Figure 50b,** indicates that the observed signal is directly dependent on the fundamental transistor characteristics and gives experimental evidence for a photovoltaic response mechanism. However, as it can be seen in **Figure 51**, which gives the gate-drain voltage-dependent response under X-ray illumination for the off-gate irradiation position, the response for higher negative gate potentials after the turn-off threshold potential shows a photoconductive behavior. This is an interesting characteristic, since the maximum response occurs for high source-drain resistances, enabling high gain, low power operation with a large optimum voltage window that, for example, would fit exceptionally well to be powered from a simple Li-ion battery circuit, which has a nominal cell voltage of 3.6 V - 3.7 V.

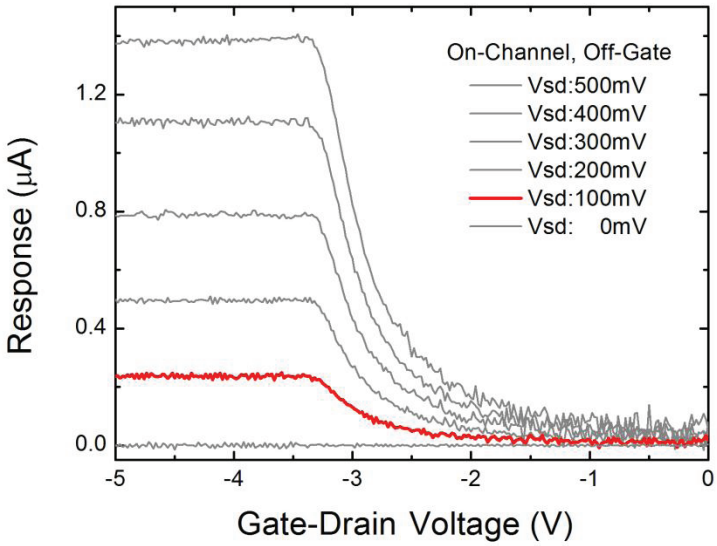


**Figure 51 | HEMT Off-Gate irradiation Response as a Function of Gate Voltage.** The "on-gate" irradiated source-drain current response of the device as a function of gate-drain voltage under 7 keV X-ray illumination.

## 5.4 Analysis of the Heterostructure Showing "Photomultiplier" Gain

In order to quantify the HEMT structures gain, dose-rate-dependent transport measurements were performed. Here the X-ray intensity dependence, of a 20 µm wide floating gate HEMT device, on source-drain current was measured and the results shown in **Figure 52**. For photons, and similarly for protons, the device responses saturate at higher intensities, but the low dose-rate regimes show a linear response that can be evaluated, in the same way as for the buffer, in terms of its quantum efficiency, $\eta$, and photoelectric gain, $g$.[173] To estimate $\eta$, knowledge of the deposited energy in the total film thickness (GaN/GaN/AlGaN/GaN) of approximately 3 µm is required.

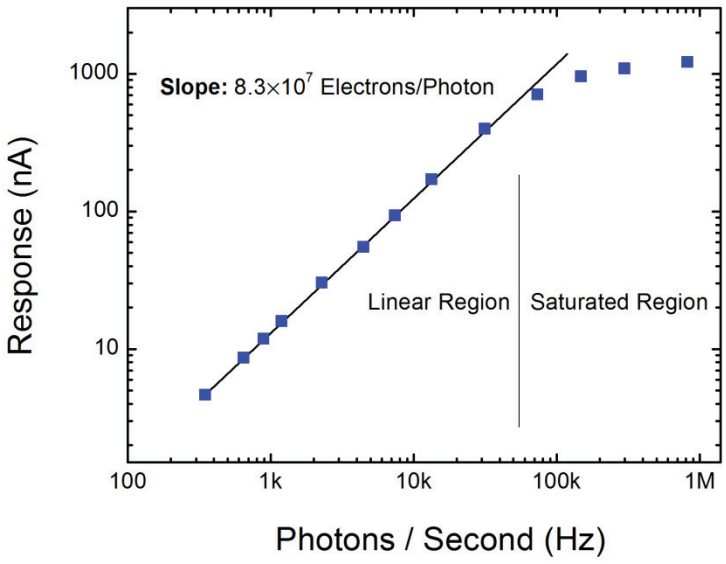


**Figure 52 | Intensity-Dependent Response of the HEMT Device.** The current response as a function of intensity of 7 keV photons. The dynamic range of the device covers photon strike rates from Hz to MHz. The linear portion reveals a gain of approximately $8.3\times10^7$ extracted electrons per photon at a source-drain voltage of 100 mV.

The online X-ray transmission tool from the Center for X-ray Optics (CXRO, Lawrence Berkeley National Laboratory, CA, USA) was used to estimate the transmitted energy for 1-20 keV X-rays through 3 µm of GaN with a density of 6.15 g/cm$^3$, and an approximate deposited energy of 910 eV/photon was found. In comparison, SRIM 2008 was used to calculate the average energy loss of 5000 protons with an energy of 20 MeV through the

3µm GaN/$Al_{0.25}Ga_{0.75}N$/GaN structure with corrected densities for GaN (6.15 g/$cm^3$) and $Al_{0.25}Ga_{0.75}N$ (5.43 g/$cm^3$). The simulation indicated that 30 keV/proton of energy was deposited, the majority of which was due to energy transferred to target electrons or direct ionization. The electron-hole pair formation energy under ionizing radiation exposure is typically assumed to be on the order of three times the bandgap, or approximately 10 eV for the case of GaN, resulting in a net electronic excitation efficiency of $\eta \approx 90$ electron-hole pairs/photon and $\eta \approx 2.9\times10^3$ electron-hole pairs/proton. The total current response of the devices under irradiation corresponded to $8.3\times10^7$ extracted electrons per photon and $1.5\times10^9$ extracted electrons per proton, at a source-drain voltage of 100 mV, respectively. Therefore, the calculated photoconductive (particle-induced) gain is $g \approx 9.1\times10^5$ ($5.3\times10^5$) carriers passing the contacts for each generated electron-hole pair produced by an incident photon (proton), or an average single electron-hole pair $20\times\log_{10}$ gain of 117 dB, in an open gate structure with a source-drain voltage of 100 mV. Given the simple models used for the estimation of the deposited energy, these independent values from photons and protons are in excellent agreement and strongly imply that the detection mechanism is the same. Furthermore, the overall dynamic range extends from a few counts per second to greater than $10^5$ counts per second, which corresponds to an information depth of slightly less than 18 bits. We note that, this is not the full capability of the device, since the gain can be increased by shutting the gate down and increasing the source-drain voltage

## 5.5 Explanation of the Heterostructure Gain

Based on these data, it is possible to conclude that the mechanism is comparable to that reported for HEMT-based UV detectors[76–84] as will be described below, but needs to be significantly extended. When an electron-hole pair is generated from the energy deposited by a high energy particle or absorbed from a photon, charge separation occurs due to the built-in electric field normal to the heterojunction plane. This is shown in **Figure 53** where a nextnano[3] numerical simulation of the GaN/$Al_{0.25}Ga_{0.75}N$/GaN heterostructure band alignment is illustrated, with the conduction and valence band edges shown relative to the Fermi level. As a consequence, electrons drift to the 2DEG channel and holes drift

into the bulk and surface regions of the device. Since 3 µm of the material is nearly transparent for the energies used in this work, the absorbed energy is approximately constant as a function of depth through the structure and the majority of electron-hole pairs are generated within the much thicker GaN buffer layer. This charge separation and associated accumulation of electrons in the 2DEG channel gives rise to an internal photovoltaic effect, which leads to a shift of the threshold potential. As a result, the current response is proportional to the transconductance of the device, as presented for the on-gate irradiation in **Figure 50.** Furthermore, these excess electrons within the 2DEG channel, apart from changing the internal field, also lower the resistive path through the device via a secondary photoconductive effect.

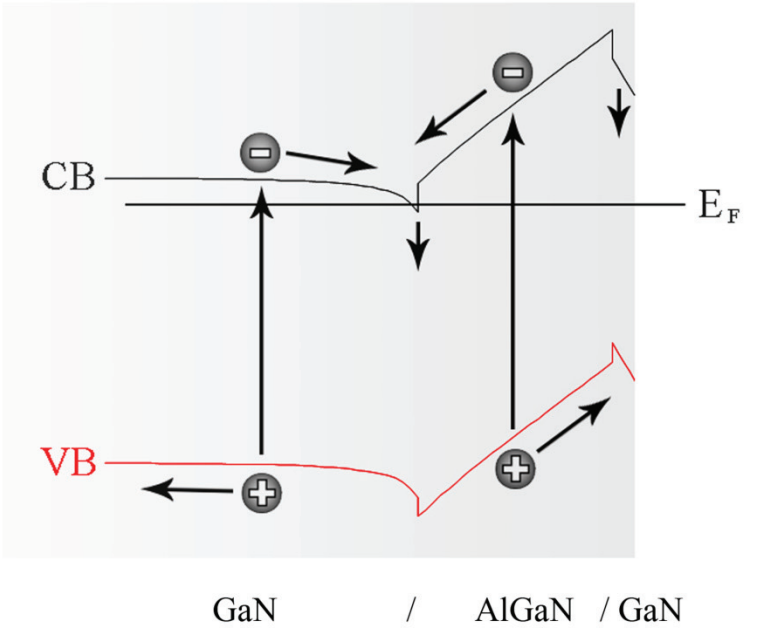


**Figure 53 | Band Diagram Illustrating the Gain Mechanism.** GaN/AlGaN/GaN heterostructure, in which CB, VB, and $E_F$ correspond to the conduction and valence band edge and Fermi level, respectively. During irradiation, separation of the generated electron-hole pairs occurs in the presence of the built-in electric field. As a result, electrons accumulate in the 2DEG channel and holes drift into the bulk and to the surface, resulting in long recombination times. The increased electron concentration in the 2DEG channel, as well as the change of the threshold potential due to excess positive charge from accumulated holes in the bulk lead to the observed ultrahigh gain and high sensitivity.

This is most likely the reason why the threshold potential shift does not give rise to a constant potential offset at all applied gate-drain voltages. Furthermore, this leads to the

photoconductive characteristics for the off-gate irradiation seen in **Figure 51**, since the flow of generated electrons to the 2DEG is not affected by changes of the gate-drain voltage at this beam position. It should be noted that this effect is independent of the buffer layer photoconductive effect, which was discussed in **Section 5.1**. The device can, therefore, be operated at off-state potentials with very low power consumption in darkness. The response is further enhanced since the lifetimes of the generated electron-hole pairs are dominated by recombination times within the 2DEG channel. Here, in the charge separated state, there is a very small concentration of holes within range of the 2DEG channel and the carrier lifetimes are much longer, typically in the sub-millisecond range[80,83] compared to a few nanoseconds[175] for homogeneous GaN thin films. Due to the charge neutrality condition, the external circuit will supply the device with an additional electron for each electron that exits the device until recombination occurs. Thus, these longer lifetimes can lead to many orders of magnitude of gain. However, these longer carrier lifetimes necessarily lead to longer response times. Nevertheless, it is expected that these lifetimes can be tuned by, for example, appropriate choice of layer compositions and thicknesses, as in the case of the InGaAs/GaAs system,[76] in order to provide an engineered balance between the device sensitivity and response time.

Although the irradiation spot sizes are of the order of a few microns, the effects described above are not limited to the beam area since the observed magnitude of the saturated current change would require that the irradiated area be characterized by a negative resistivity. This indicates that when an electron is trapped within the channel, it is delocalized and free to move throughout the 2DEG along the applied electrical field, thereby changing the conductivity, charge and sheet carrier concentration of the entire channel. Thus, the built-in electric field must dominate over the applied potential, enabling the majority of holes to move deep into the quasi-neutral zone where charge neutrality is no longer a local phenomenon.[76] Moreover, since it was possible to reproducibly resolve local inhomogeneities within the active area at the micron resolutions of the focused beams, it is possible to conclude that the response is generated locally but impacts the entire structure and that the devices could be miniaturized using conventional microelectronics techniques.

## 5.6 Transient Response

Even in light of recent advances in growth that have led to improved film qualities, persistent photoconductivity in AlGaN/GaN heterostructures is a well-documented setback for this material system,[176–179] and attributed to the high concentration of trap states, which are associated with capture of photo-excited electrons by broadly distributed deep defect-related acceptor levels. Long transient persistent photoconductivity, with decay time constants in the range of hours, has been ascribed to the transfer of photoexcited electrons from deep level impurities (DX-like centers) in the AlGaN barrier to the channel.[180,181]

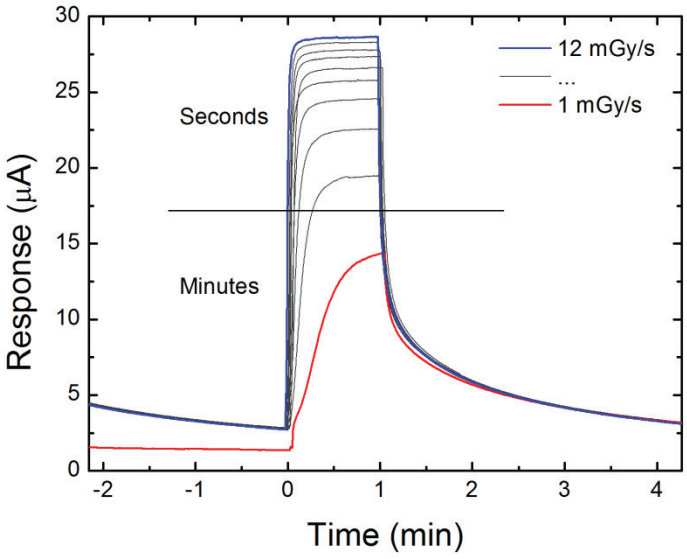


**Figure 54 | Transient Buffer Response to X-rays.** A collapsed view of a rising pulse irradiation train from 1 mGy/s to 12 mGy/s where the on/off transients are exemplified.

This is exemplified in **Figure 54**, where a collapsed view of the irradiation pulse trains on the devices with the medical Bremsstrahlung systems show the transient buffer response where the typical persistent photocurrent is evident. The shape of the pulse, especially of the on-transient, changes significantly as a function of increasing intensity, settling in seconds instead of hours. The same can be said for the off transients if the beam is not completely switched off but adjusted back to a pre-set background level of X-ray radiation. To further evaluate this, a device was illuminated with an Al $K_\alpha$ source, where for every change in emission current, the time the device current needed to settle was

measured, as presented in **Figure 55**. We note that this was realized during maintenance of the surface analytics chamber where the devices were operated at high vacuum pressures.

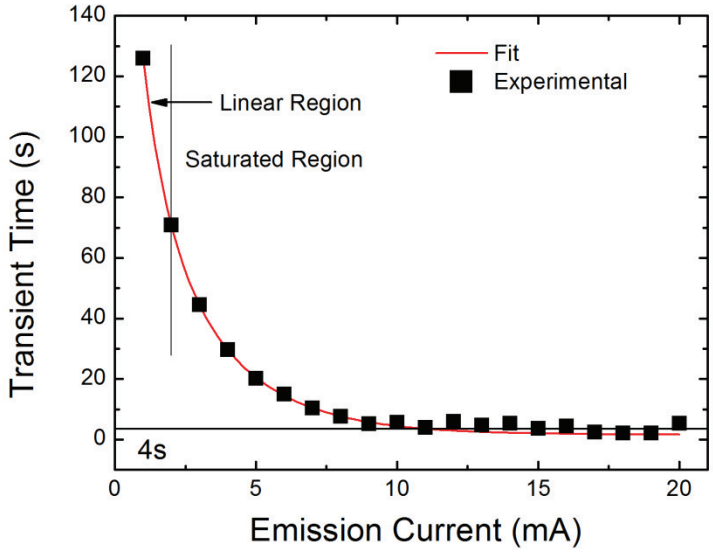


**Figure 55 | Response Settling Time of the Buffer. S**ettling time as a function of X-ray source emission current. Each level took approximately 4 s to adjust to by hand.

The intensity changes were made by hand and the alteration in emission current required approximately 4 seconds to adjust. The linear response region stops at emission currents above approximately 2 mA, corresponding to settling times longer than 70 s, and the device response only became faster than the adjustment speed at 5 times higher power at 11 mA. In comparison, a typical shutter time for a conventional medical X-ray system is approximately 200 - 500 ms, where a "full mouth scan", that consists of 18 exposures, gives a dose of 9-12 mGy (90-122 µSv for skin with a weighting factor of 0.01).[182] For GaN, staying on the border between the linear and saturated region, a dose rate of 0.3 mGy/s (**Figure 37**) is expected for 70 s, effectively doubling the dose to 210 µSv for skin.

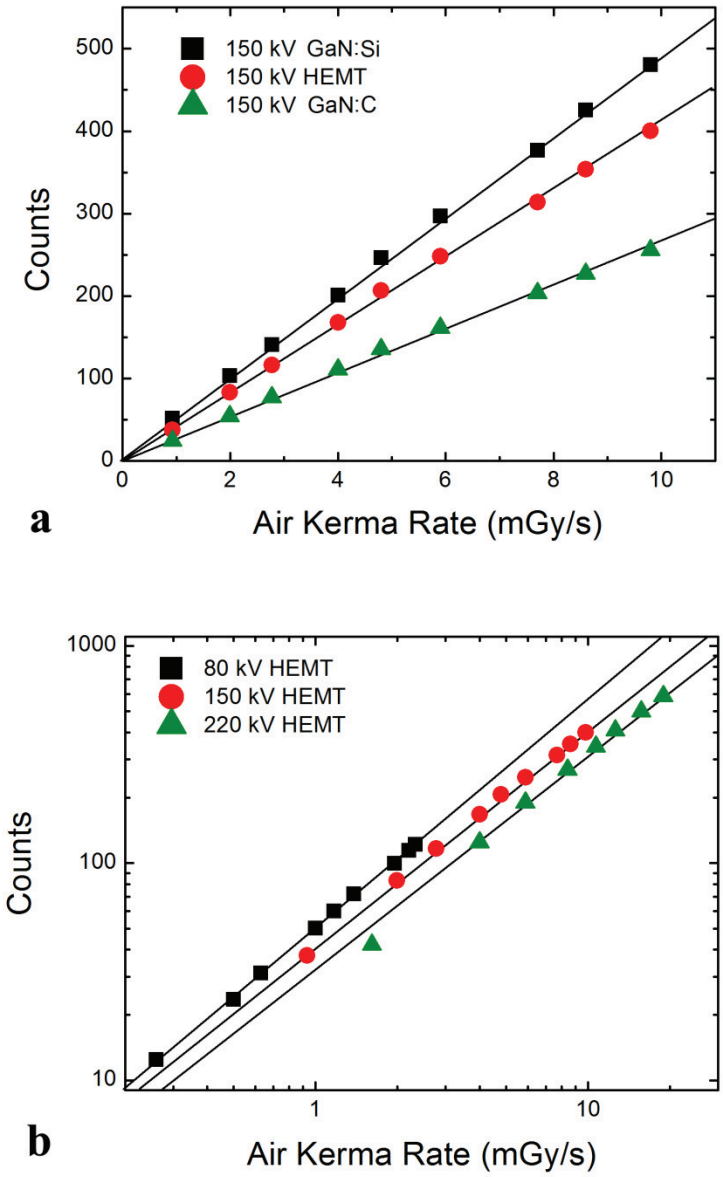


**Figure 56 | Luminescence of GaN during irradiation.** Pixel intensity counts from a low light camera for GaN fluorescence during irradiation. A comparison of *n*-type (Si doped) GaN, HEMT and C-compensated GaN at 150kV. The energy dependence of the HEMT structure is shown in **b)**, and is similar for the other structures.

These trap states are also responsible for the well-known "yellow luminescence" of illuminated GaN,[166,183] which is attributed to an electronic transition between a shallow donor and a deep acceptor widely distributed around 2.2 eV below the conduction band minimum. The deep acceptors are not evenly distributed in the bulk but rather decorate grain boundaries.[184] This effect is weak for these photon energies, but clearly observable

with a low-light camera. This can give an indication of the concentration of defects, but since it depends on the Fermi level position, a comparison of different samples should be made with caution since, for example, *p*-type GaN does not luminesce in this energy range even though such states are present. However, as shown in **Figure 56**, the average emission intensity is linear with the dose-rate and therefore has the possibility to provide dosimetry via optical-detection. Here, we show that it is a material specific property and therefore can be measured on *n*-type (Si doped GaN), HEMT and carbon-compensated GaN. As it is shown in **Figure 56a** for 150 kV, the three sample types have different sensitivities, the carbon compensation reducing the slope in comparison to the Si-doped sample and the intermediate HEMT structure, which contains both materials. Similar results were also obtained for 80 and 220 kV. Furthermore, the effect retains similar energy dependencies to the electrical measurements. As can be seen in **Figure 56b**, there is an energy dependent shift for the slope shown for a HEMT sample for 80, 150 and 220 kV. A similar effect is obtained for the GaN:Si and GaN:C samples.

These persistent photoconductivity effects result in response times that have limited these devices usefulness for real-time detection applications. Here, we make a comparison between the transient response of the buffer and the heterostructure. **Figure 57** shows the behavior of an open gate device during illumination on the channel and the corresponding response of the buffer layer off the channel. The buffer layer response (**Figure 57a**) exhibited the expected behavior, with transient times comparable to those observed for the buffer. In contrast, the on-channel device response in the low dose-rate regime is characterized by very fast response times, as shown in **Figure 57b**. In this low dose-rate regime, deep level charge trapping does not have an observable impact on the overall response. Detailed characterization of the response time was not possible under the current experimental configuration, since our measurements were limited by the 20 ms maximum sampling speed of our instruments. However, even the instrument limited transients shown here are fast enough, for example, for medical imaging.

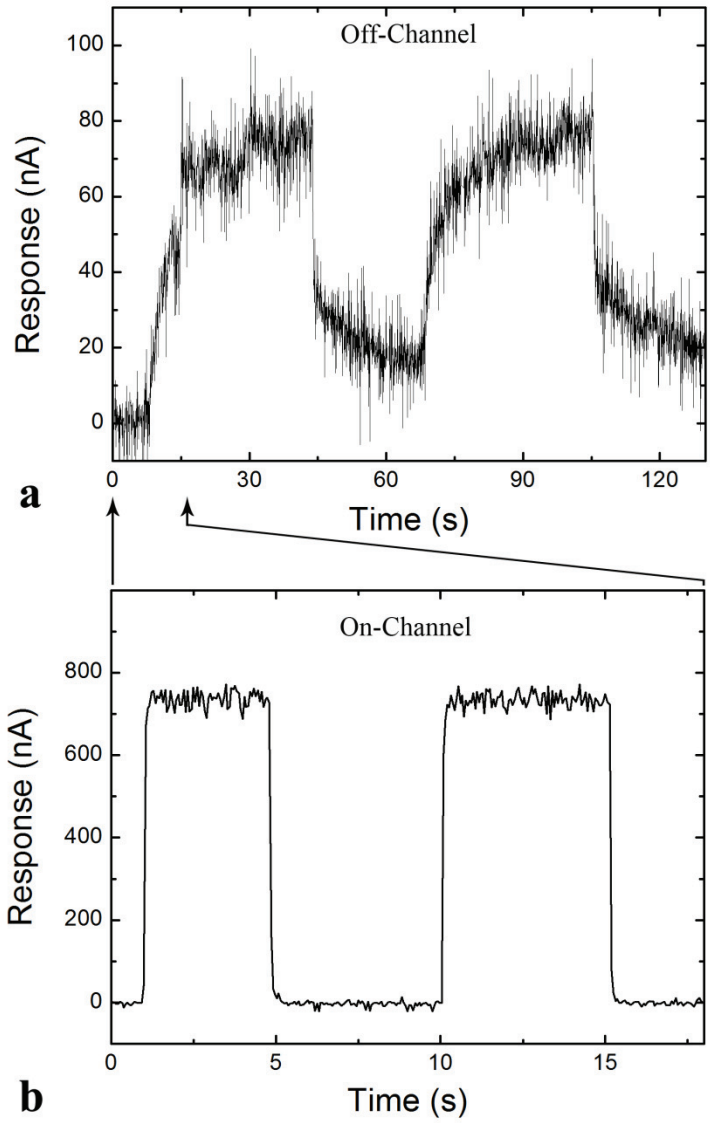


**Figure 57 | Transients of the HEMT Device vs. the GaN Buffer. a)** The transient photon response of the off-channel beam position on the buffer showing the typical long transient persistent photoconductivity. In comparison to a HEMT deviceis shown in **b)** exhibiting millisecond rise and fall times that are much faster than those observed for the buffer. Also note the different response scales in **a)** and **b)**.

# 6 Summary

In this thesis I have summarized our investigation of the interface between GaN wide bandgap semiconductor heterostructures and (bio)molecular systems functionalized on their surfaces for biosensing, bioelectronic and photoelectric applications, with a special emphasis on the processes associated with high energy ionizing irradiation including heterostructure photoelectric gain mechanisms.

## 6.1 Conclusions

### Photocatalytic Degradation

I have presented our findings in the pursuit to identify ***if a compatible energetic window for GaN or SiC can be found, within which it is favorable for a selection of organic systems to be actively charged or discharged by direct interaction with the semiconductor substrate?***

***In conclusion:*** We demonstrated UV-induced photocatalytic cleavage of aliphatic molecules covalently bound to *n*-type GaN surfaces. The associated charge transfer leads to the degradation of the layer due to removal of bonding orbital electrons which is analogous to low energy photo-induced charge transfer ionization of the alkyl chains well below the energy normally required for molecular cleavage. We have proposed a model by which UV illumination of *n*-type GaN leads to surface accumulation of holes at an energetically favorable position for recombination with an electron abstracted from the HOMO of the organosilane ODS. Furthermore, we have shown that either an upward shift of the valence band maximum (as is the case for *n*-type 6*H*-SiC) or an opposite direction of surface band bending (*p*-type GaN), leads to a suppression of the charge transfer. This work demonstrates that the charge transfer can significantly reduce the ionization energy threshold for the removal of bonding orbital electrons from organic SAMs, which could be exploited for driving chemical reactions on surfaces.

Understanding such charge transfer phenomena will be vital in the emerging fields of molecular and biomolecular electronics since it could, for example, allow a selection of organic systems to be actively charged or discharged by direct interaction with the semiconductor substrate.

## Brief Comments on Device Miniaturization

In an initial avenue of this work, we developed techniques to create devices with enhanced sensitivity, resolution and stability. We have optimized processing techniques to reproducibly create devices with single micrometer widths. These methods were used throughout this work and enabled the use of devices down to sizes of 20 µm. We found that the lateral damage, caused by techniques like ICP-RIE and FIB, results in a nonlinear decrease in the 2DEG conductance as a function of width for devices thinner than 7 µm and total current collapse occurred at 2 µm instead of 0 µm as predicted by the linear/ohmic model. However, this method was used to reliably create 2DEGs with an active width estimated to 250 ±100 nm for 2 µm physical channel widths. Furthermore, we show the characteristics of the devices when operated in metal-insulated gate and solution gate modes. We note that devices with 64 nm widths have been fabricated with similar methods,[139] which would be a very interesting continuation of this work.

## Novel Sensors based on Sensitivity-Enhanced HEMTs

Next, we have investigated the question ***whether the reduction of the heterostructure barrier thickness through the use of AlN/GaN-based HEMT structures can give significant advantages, without sacrificing stability, in comparison to AlGaN/GaN devices to merit further investigation as a replacement?***

***In conclusion:*** We have chosen to analyze the devices as ISFETs and successfully constructed a novel electrochemical and environmental control system, which was built to the specifications required to analyze (bio)molecularly modified AlGaN/GaN SGHEMTs. We show that this system is capable of measuring a stable and reproducible *p*H response from both GaN and diamond devices at 53.3 mV/*p*H at 10.6 °C and 25.9 mV/*p*H at 22 °C, respectively, and a temperature dependence of approximately 18 mV/°C for the SGHEMTs. This system was used to demonstrate the enhanced sensing capabilities of

GaN/AlN/GaN HEMT structures as *p*H-sensitive SGHEMTs. This was achieved by using the recent progress of PAMBE to improve upon the transconductive sensitivity of the devices, by decreasing the 2DEG-to-surface distance by replacing the AlGaN layer with an AlN spacer. We found that the thinner 7.5 nm AlN device exhibited a transconductivity of 131 µS in comparison to 72 µS of the thicker 19 nm barrier devices, which are comparable to those used throughout this work, with no negative impacts to the device performance.

## Enzyme Functionality Analysis on Immobilization

Then, we have studied ***if it is possible through a systematic comparison with respect to the techniques applied for enzyme immobilization, to distinguish between their effects on enzyme activity and functionality?***

***In conclusion:*** We used the enzyme penicillinase as a model system and compared its response for covalent immobilization on APTES-modified AlGaN/GaN SGHEMTs and drop-coating on the transistors surface. The control system was shown to be a stable platform for electronic analysis of enzyme activity and was able to produce high quality data-sets where the differences between covalently bound and physisorbed enzymes on the device surfaces are easily identified. Here, we show that the covalently bound enzymes exhibited high reproducibility with respect to the enzyme/substrate-molecule affinity, which resulted in a sensitivity of 152±8 µV/µM of penicillin in 0.5 mM PBS buffer. Furthermore, we show the possibilities to analyze a bio-chemical system on the devices surface by predicting the presence of an enzyme (sub)monolayer for the covalently immobilized enzymes, evidenced by comparison to the properties of physisorbed multilayers.

## Heterostructure Gain Mechanism

Moving to dosimetry applications, we examined whether ***GaN can overcome difficulties, such as long transient persistent photoconductivity, and be used for high energy ionizing radiation dosimetry?***

***In conclusion:*** We investigated the photoreseponse of advanced AlGaN/GaN heterointerfaces, comparing it to the response of GaN thin films. We found that, even in light of recent advances in growth that have led to improved film qualities, GaN is still plagued by, for example, long transient persistent photoconductivity with settling times between minutes and hours. Furthermore, the trap states associated with the yellow luminescence of irradiated GaN are still numerous enough to allow dosimetry via optical-detection. We also propose a model to explain the detection mechanism and energy dependence of the devices and through it calculate an unsaturated internal gain of just below $10^3$ carriers passing the contacts for each generated electron-hole pair produced by an incident (spectrally representative) photon for a 80 mV source-drain voltage. However, while evaluating the photoresponse of the devices there were many indications of a separate response mechanism due to the presence of a 2DEG channel. This response is in complete saturation at the intensities used with the Bremsstrahlung sources in the medical X-ray bandwidth. We note that such 2DEG responses are known, as they have been reported for UV detection. However, we found that a detailed study of the heterostructure, conducted in the ultralow dose-rate regime, gave a far more detailed insight into the mechanism, which is also applicable for UV radiation, for particle energies hitherto not previously investigated. Here, we show that the AlGaN/GaN HEMT structure exhibits pronounced “photomultiplier” gain under ionizing radiation, yielding extremely large sensitivities in ultralow dose-rate regimes. The gain was proven to be similar for X-rays in the 1-20 keV range and for 20 MeV protons, and the device employed obeys the material specific absorption cross-section predicted through the exponential power law using tabulated mass attenuation coefficient values. This ‘ultrahigh’ gain can be described by charge separation within the heterostructure. Similar mechanisms for UV light were reported to have a photovoltaic nature. However, the only way to satisfactorily explain our results was through extending this model to include a combination of photovoltaic and photoconductive effects. Importantly, the more photoconductive portion of the response allows the HEMT devices to function best during small current operation when the channel is completely shut down by, for example, application of a negative gate-drain voltage. This allows for low power, unsaturated single electron-hole pair “photomultiplier gains” of $10^7$ at single Volt potential differences, operated at room temperature.

Furthermore, this response mechanism is virtually unaffected by the charging of trap states. Instead the transients are dominated by the recombination times of the electrons trapped in the 2DEG channel. Here, part of the high gain comes from decreased channel resistance during these millisecond transient times. A certain tuning of gain verses transient time should be possible through heterostructure design. Moreover, the GaN device is characterized by a dynamic range of response of 18 bits per second for each pixel and reacts to both spectral energy and intensity. The devices exhibit an extremely high stability, having been operated for several months with total exposures of several hundred Gy with no evidence of any permanent performance alteration. Thus, together with the exceptional new capabilities for high sensitivity and resolution real time monitoring, which is competitive with and complements state-of-the-art detectors, these devices are extremely promising for future ionizing radiation detector technologies in applications ranging from high energy physics to medical imaging. Indeed, such a device could have high spatial, temporal, energy, and dose resolutions to high energy ionizing radiation and, in this case, could help facilitate rapid detection of harmful radiation breaches, reduce the dose required for medical imaging, enable the study of possible radiation effects on cell systems, and complement existing technologies for high energy particle experiments.

## New Study on Multi-Functional Device Capabilities

Combining these topics and in conjunction with the study of real-time changes in physiological signals of cells prior to, during and after exposure to ionizing radiation, we investigated ***if it is possible to make simultaneous chemical sensing and ionizing radiation dosimetry using single devices.***

***In conclusion:*** We have made a detailed characterization of simultaneous chemical sensing and ionizing radiation dosimetry using single devices. To this end, based on the successful development of processes and instrumentation for precisely controlling and monitoring solution gate devices and collaborative interests in enabling the study of possible radiation effects on cell systems grown on the surfaces of devices, we expand our work to include energies in the medical X-ray bandwidth. Here, we demonstrate the stability of the device in solution during X-ray irradiation and found that SGHEMTs

operating in electrolytes retain their *p*H sensitivity of 57 mV/*p*H. Furthermore, the devices simultaneously show a stable and reproducible response to X-ray radiation in the dose-rate range from 1 µGy/s to 10 mGy/s and the energy range from 10 keV to 150 keV, with a slope of 82 $nA \cdot \mu Gy^{-1} \cdot s^{-1}$ for 75 kV. Moreover, our findings suggest that the fundamental device characteristics could be utilized for separating the irradiation signal from the *p*H response without compromising the operational stability of the device. Such devices are well-suited for combined hard radiation and ion-sensitive measurements in a range of harsh environments and thus also for future integrated radiation dosimetry and bio-sensing medical applications. Furthermore, since the SGHEMTs were found to be "blind" in the buffer region to focused low dose rate beams, seeding cells on arrays and stressing them with irradiation on a blind spot of the device could be an excellent way to continue this work while studying cellular communication.

## 6.2 Outlook

### Charge Transfer to Complex Molecules

We have demonstrated charge transfer between a SAM of simple aliphatic chains and a semiconductor surface and identified the energetic window within which it is favorable. However, there are many unanswered questions on this system as the details of the multi-step reaction are not fully known. Further experiments would help to understand the specific contribution of water to the suggested reaction mechanism and if preliminary data from the electrical manipulation of surface band position, which shows that applying more than a certain surface potential with the electrochemical cell causes the monolayer degradation as seen by a current spike and a change in SWCA, is relevant to the discussed effect. Understanding such charge transfer phenomena will be vital in the emerging fields of molecular and bio-molecular electronics. As the information gathered in this thesis has already been applied to ongoing projects where the goal is to achieve charge transfer between semiconductors and complex biological systems, this is already being demonstrated. Very encouraging results have been achieved with Rhodobacter Sphaeroides and photosystem which is beyond the scope of this thesis. However, a brief

introduction will be given to the preliminary results collected from the the fluorescent barrel protein mtSapphire, which is the light-emitting component of the jellyfish *Aequorea Victoria*, illustrated in **Figure 58**. We chose mtSapphire because it is one of the most bleach resistant, and it has one of the widest spectrally separated absorption and emission peaks at 399 nm and 511nm, respectively. This, in contrast to the photocatalytic work reported in this thesis, has the potential to exemplify the charge transfer visually. To this end photo-bleaching speeds were compared by illuminating mtSapphire on a GaN and on sapphire ($Al_2O_3$) by using a fluorescence microscope.

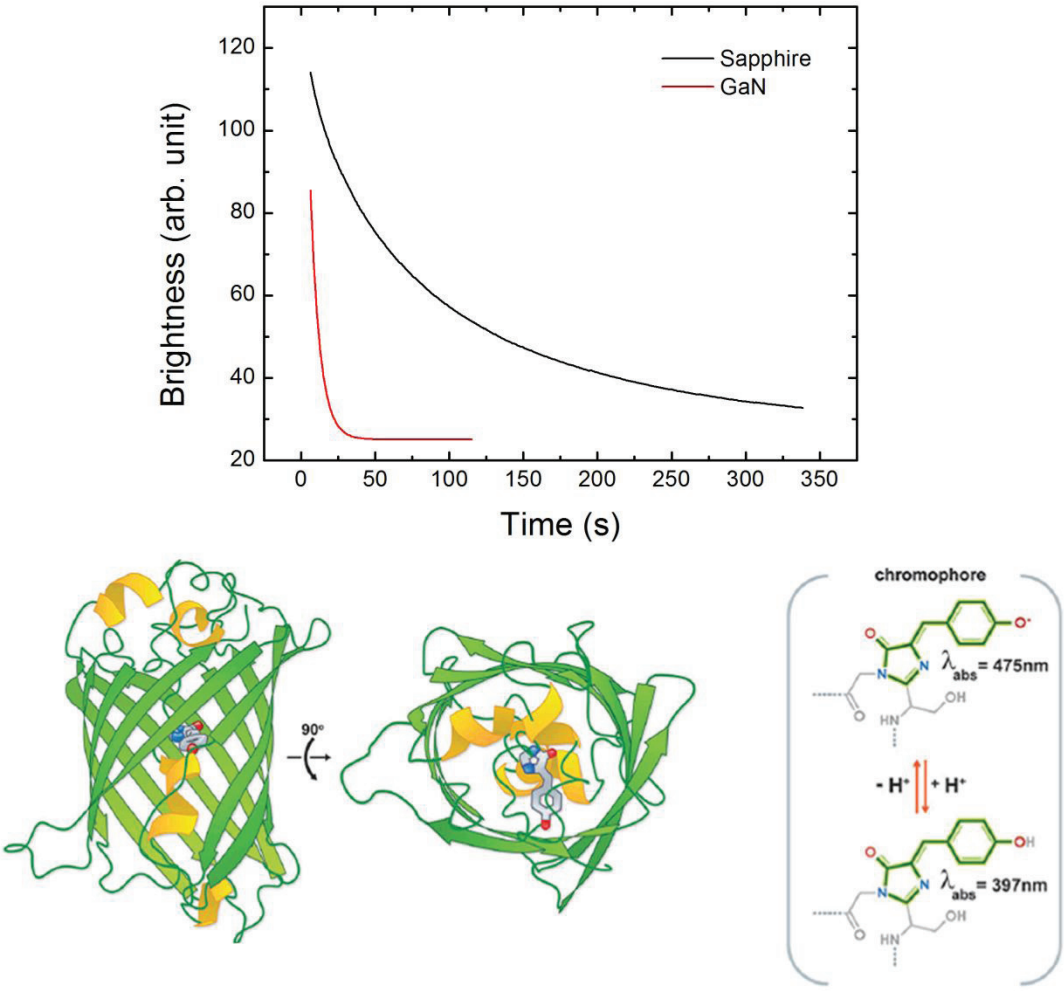


**Figure 58 | Bleaching Curve of mtSapphire.** Bleaching curves of mtSapphire on a sapphire and GaN substrate indicates an energetic alignment between the complex molecule and the semiconductor. Illustration of the fluorescent protein mtSapphire provided by the Max-Plank-Institute for Neurobiology.

The results are depicted in **Figure 58**, and what seems to be successful charge transfer can be seen as a much faster bleaching speed of the biomolecule on GaN in comparison to sapphire. This preliminary result gives a solid direction to continue this work. Furthermore, the demonstrated photocatalytic reduction of molecular ionization levels could also be exploited for driving chemical reactions on surfaces.

## Polymer-Brush Functionalized SGHEMTs

In a similar way to the penicillinase-modified SGHEMTs, other active molecules could be used to functionalize the surface with end groups that react to environmental changes. This technology holds great future promise in, for example, the development of lab-on-chip environments. The outlook for this work is limited only by nature's enormous diversity of functional (bio)molecules and our own creativity. However, recent interest in polymer-brushes makes them an exemplary point for continuation. Not being as selective as enzymes, polymer-brushes make up for this due to their vast possibilities for customizable functionalities. Indeed, polymer-brushes can respond to different external or internal stimuli, such as *p*H, solvent, ions, temperature, radiation, electric or magnetic fields.[185] Here, we study the time-dependent effects of poly-DMAEMA, which has a *p*Ka-dependent change in charge that subsequently causes a variation in its hydrodynamic volume. As can be seen in **Figure 59**, the *p*H dependence of the device before polymerization with 10 min titration steps is compared with the same device after polymerization with the same rate of titration and standard deviation limited titration steps. In a basic solution, at *p*H 10, the molecules should be in a collapsed state (decreased hydrodynamic radius).[185] As its environment is titrated towards low *p*H values (high ionization), the poly-DMAEMA brushes passes its $pK_a$ value and stretches (increasing in hydrodynamic radius). In a similar manner to the previously studied system, which compares the thinner covalently bound penicillinase to the thicker physisorbed layers, the diffusion constants change when the polymer-brush layer expands.

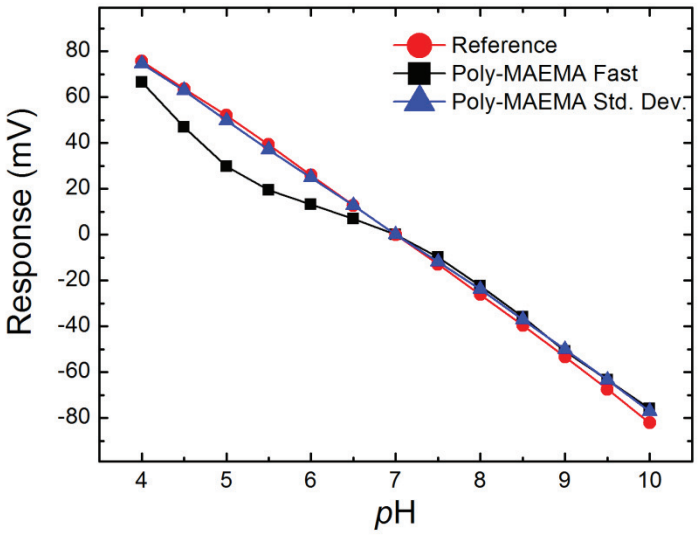


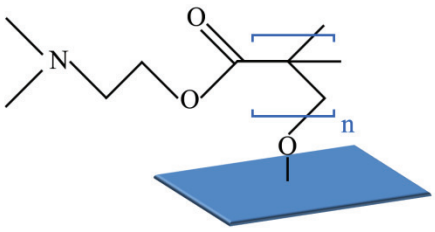


Poly(2-(dimethylaminoethyl)methacrylate)

**Figure 59 | *p*H Dependence of Polymer-Brush Functionalized SGHEMT.** The graph shows how the change in hydrodynamic volume of polymer-brushes as a function of *p*H impacts the diffusion characteristics at the molecular/semiconductor interface. A comparison between a non-functionalized (reference) and a poly-DMAEMA-functionalized device titrated at a fast constant time interval (poly-MAEMA fast) and a slow standard deviation triggered titration (poly-MAEMA Std. Dev.) is shown. An illustration of the molecular structure is also provided.

Since the *p*H of the bulk solution continues to change and the initial smaller slope for the transistor is cause by much longer transients (not shown), the polymer-brush layer is, for the most part, prohibiting the bulk solution from reaching the gate. This conclusion is further strengthened when forcing the system to fulfill a preset standard deviation value, only continuing with the next titration when any drift has settled. Here, the slope goes back almost to the initial characteristics of the device without polymer-brushes, but at the cost of much longer waiting intervals between titrations for small *p*H values.

## Attenuated X-ray Response (Imaging)

We found that advanced AlGaN/GaN heterointerfaces could be used to overcome many of the shortcomings of single GaN thin films, exhibiting "photomultiplier" gains, millisecond response times at room temperature at single Volt operational potential differences. These devices can be structured, as well as miniaturized, using conventional microelectronics techniques that allow for fabrication of integrated two-dimensional pixel detectors. Furthermore, it would seem that the necessity of increasing the arrays complexity by gating could be avoided as enhancement mode transistors can be made by decreasing the width of the device.[139] However, partially removing the barrier layer to create the gate recess,[186] implanting fluorine ions into the barrier under the gate,[187] or selectively inserting a *p*-type AlGaN or GaN layer under the gate,[188] are also options to be considered. Here, a suite of experiments were performed in order to fully assess the efficacy of these devices as versatile tools for online X-ray dosimetry and imaging for medical and technical applications. Many of these results are only applicable to the buffer response and can be found elsewhere.[112] While the heterostructure response is faster and more sensitive than the buffer response, they seem to share the same energy dependence. So a comparison can be made for imaging, where we demonstrate the devices capabilities for dosimetry and spatial resolution, while making attenuated measurements through a human phantom torso and imaging the wrist segment of a human phantom. Here, a particularly important aspect of X-ray imaging is the optimization of spectral energy and intensity to adjust for the best image contrast and brightness. It is also a solid indication that the device is sensitive to and will detect the higher photon spectral energies that can be seen as the change in transmission due to energy-dependent attenuation of a material.

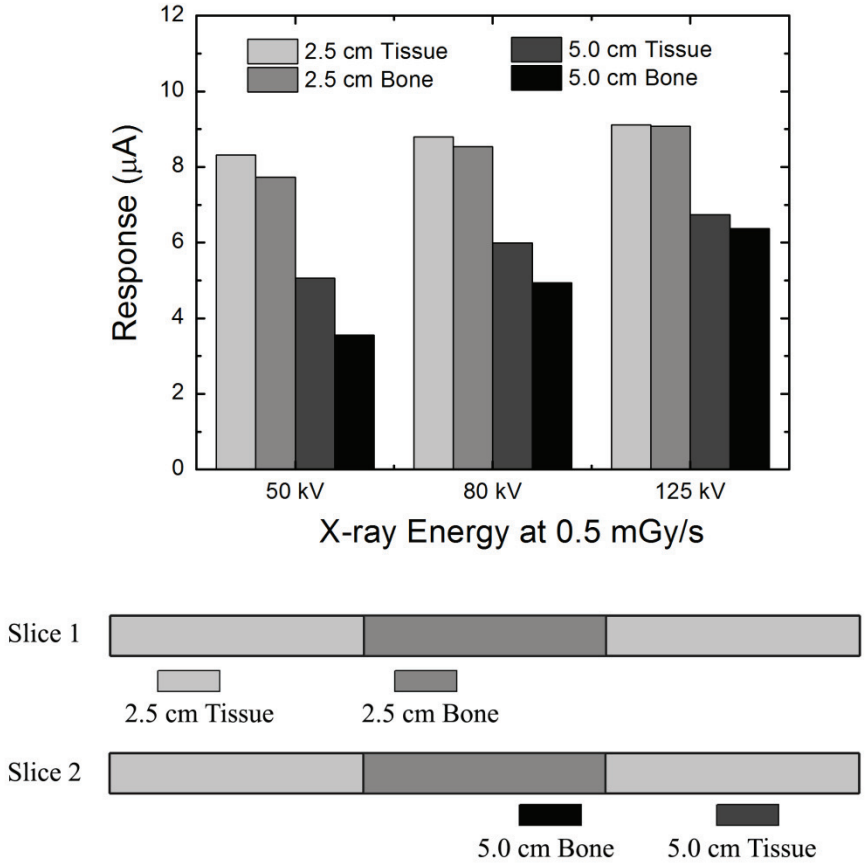


**Figure 60 | X-ray Contrast Calibration of GaN Devices.** Schematic illustration of the sensor arrangement behind 2.5 cm thick slices from an Alderson radiation phantom for contrast and brightness calibration. Here, the difference between human spine and the tissue equivalent in which it is embedded can be measured, providing for total shielding depths of 2.5 cm and 5 cm for each material. As expected, the X-ray transmission through soft tissue equivalent material and human bone is altered by the incident energy and material thickness.

To demonstrate this, four HEMT-sensors were placed in the mid-torso region of a human irradiation phantom composed of both soft tissue equivalent material and a natural human spine, as shown in **Figure 60**. Devices were placed to show the X-ray attenuation through 2.5 and 5 cm of each. **Figure 60** shows the response from the devices at the same air kerma rate at three different energies, requiring the emission current for the acceleration voltages 125, 80 and 50 kV to be adjusted to 2, 6 and 16 mA. Bone material is known to exhibit a higher mass attenuation coefficient than soft tissue, especially at energies below 100 keV,[189] and the expected difference between them is clearly observed.

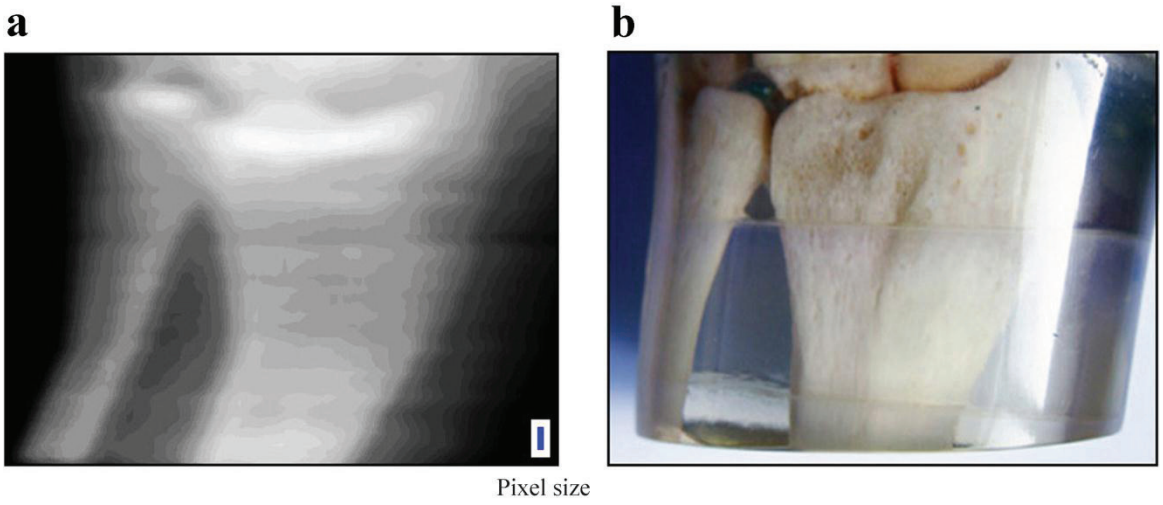


**Figure 61 | X-ray Image of a Human Phantom Wrist Segment. a)** 8-bit X-ray gray scale contour maps recorded using GaN-HEMTs (the total device pixel size is indicated white and the active area blue) of a human phantom wrist segment in comparison to the optical picture in **b)**.

Once the optimum parameters have been selected to match the material-specific shielding properties due to energy dispersive X-ray absorption within the phantom, the response to small changes in attenuation and the capabilities of the device for lateral resolution could be evaluated by creating an X-ray image of the wrist section of a human phantom. While such devices have the potential to be straightforwardly miniaturized in order to form high density pixel arrays for imaging purposes, our fabricated chips were 5×3 $mm^2$ and only contained a single device, thus limiting the pixel dimensions to this size. To boost the spatial resolution, an automated two-dimensional translation stage was used to create the images. Several hundred pictures were taken at different offsets from the center position of each pixel with an acquisition time of 200 ms and the data were recombined into a single image by interpolation and averaging. This technique better utilizes the intentional 2.8×1 $mm^2$ active area of the device, and gives additional data to further enhance the image in post processing. The two-dimensional data were plotted into 8-bit X-ray gray scale contour maps to resemble a standard X-ray photograph in **Figure 61a,** and an optical picture of the corresponding human phantom segment is provided in **Figure 61b**.

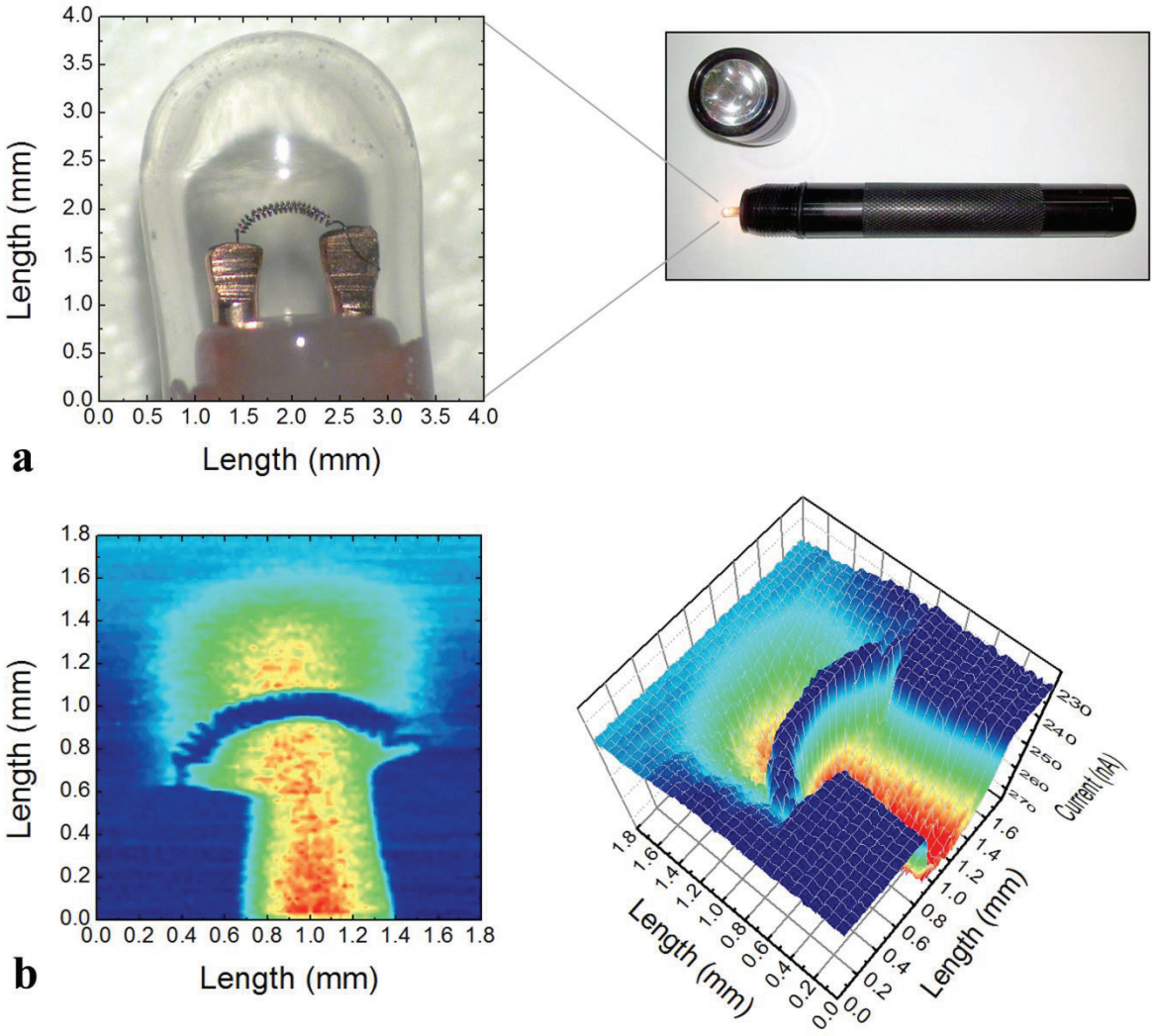


**Figure 62 | High Resolution HEMT X-ray Image of a Flashlight Bulb. a)** A microscope image of the bulb shows the approximately 3×3 mm object with a 50 µm thick spiral filament. **b)** The 2D and 3D images show the plotted X-ray data. Here the spiral filament is clearly visible and in the surrounding area the increase of current shows an absence of material indicating that the center is hollowed out to form a sealed cavity.

The differences between tissue, bone and air, as well as the distances between specific features and joints, can be clearly identified. Furthermore, close inspection of **Figure 61** reveals that segments of the phantom tissue appear as vertical lines in both pictures. This shows that while thin films of this material were expected to be poorly suited for X-ray dosimetery at energies higher than 20 keV,[74] there still seem to be a working range beyond that estimate. In comparison, to demonstrate the imaging capabilities of the

heterostructure, the 3×3 $mm^2$ light bulb of a small flashlight, depicted in **Figure 62a**, was scanned. The scanning resolution was set to 10 µm × 10 µm using a high quality beam with a focal point diameter of about 3 µm. The result can be seen in **Figure 62b**, where the 2D and 3D images show the plotted X-ray data. Here the spiral filament clearly visible and in the surrounding area the increase of current shows an absence of material indicating that the center is hollowed out to form a sealed cavity. This image easily shows the superior device characteristics of the heterostructure over the buffer response.

# 7 Bibliography


1. Schreiber, F. Self-Assembled Monolayers: From Simple Model Systems to Biofunctionalized Interfaces. *Journal of Physics: Condensed Matter* **16**, R881–R900 (2004).

2. Stutzmann, M., Garrido, J. A., Eickhoff, M. & Brandt, M. S. Direct Biofunctionalization of Semiconductors: A Survey. *Physica Status Solidi (a)* **203**, 3424–3437 (2006).

3. Fissel, A. Artificially Layered Heteropolytypic Structures Based on SiC Polytypes: Molecular Beam Epitaxy, Characterization and Properties. *Physics Reports* **379**, 149–255 (2003).

4. Allara, D. L. & Nuzzo, R. G. Spontaneously Organized Molecular Assemblies. 1. Formation, Dynamics, and Physical Properties of n-Alkanoic Acids Adsorbed from Solution on an Oxidized Aluminum Surface. *Langmuir* **1**, 45–52 (1985).

5. Sagiv, J. Organized Monolayers by Adsorption. 1. Formation and Structure of Oleophobic Mixed Monolayers on Solid Surfaces. *Journal of the American Chemical Society* **399**, 92–98 (1980).

6. Ulman, A. Formation and Structure of Self-Assembled Monolayers. *Chemical Reviews* **96**, 1533–1554 (1996).

7. Schreiber, F. Structure and Growth of Self-Assembling Monolayers. *Progress in Surface Science* **65**, 151–257 (2000).

8. Adden, N. *et al.* Phosphonic Acid Monolayers for Binding of Bioactive Molecules to Titanium Surfaces. *Langmuir* **22**, 8197–204 (2006).

9. Twardowski, M. & Nuzzo, R. G. Chemically Mediated Grain Growth in Nanotextured Au, Au/Cu Thin Films: Novel Substrates for the Formation of Self-Assembled Monolayers. *Langmuir* **18**, 5529–5538 (2002).

10. Adlkofer, K. *et al.* Chemical Engineering of Gallium Arsenide Surfaces with 4'-Methyl-4-Mercaptobiphenyl and 4'-Hydroxy-4-Mercaptobiphenyl Monolayers. *Journal of Physical Chemistry B* **107**, 11737–11741 (2003).

11. Nesher, G. *et al.* Energy Level and Band Alignment for GaAs-Alkylthiol Monolayer-Hg Junctions from Electrical Transport and Photoemission Experiments. *Journal of Physical Chemistry B* **110**, 14363–71 (2006).

12. Brzoska, J. B., Azouz, I. B. & Rondelez, F. Silanization of Solid Substrates: A Step Toward Reproducibility. *Langmuir* **10**, 4367–4373 (1994).

13. Stevens, M. J. Thoughts on the Structure of Alkylsilane Monolayers. *Langmuir* **15**, 2773–2778 (1999).

14. Cloarec, J. P. *et al.* Functionalization of Si/SiO2 Substrates with Homooligonucleotides for a DNA Biosensor. *Sensors and Actuators B* **58**, 394–398 (1999).

15. Baur, B. *et al.* Chemical Functionalization of GaN and AlN Surfaces. *Applied Physics Letters* **87**, 263901 (2005).

16. Schoell, S. J. *et al.* Functionalization of 6H-SiC Surfaces with Organosilanes. *Applied Physics Letters* **92**, 153301 (2008).

17. Fujii, K. & Ohkawa, K. Photoelectrochemical Properties of p-Type GaN in Comparison with n-Type GaN. *Japanese Journal of Applied Physics* **44**, L909–L911 (2005).

18. Holzwarth, A., Schatz, G., Brock, H. & Bittersmann, E. Energy Transfer and Charge Separation Kinetics in Photosystem I Part 1: Picosecond Transient

Absorption and Fluorescence Study of Cyanobacterial Photosystem I Particles. *Biophysical Journal* **64**, 1813–1826 (1993).

19. Brettel, K. & Leibl, W. Electron Transfer in Photosystem I. *Biochimica et Biophysica Acta* **1507**, 100–114 (2001).

20. Dimitrov, R. *et al.* Two-Dimensional Electron Gases in Ga-Face and N-Face AlGaN/GaN Heterostructures Grown by Plasma-Induced Molecular Beam Epitaxy and Metalorganic Chemical Vapor Deposition on Sapphire. *Journal of Applied Physics* **87**, 3375–3380 (2000).

21. Wood, C. & Jena, D. *Polarization Effects in Semiconductors: From Ab Initio Theory to Device Applications*. (Springer Science+Business Media, LLC: New York, 2008).

22. Steinhoff, G., Purrucker, O., Tanaka, M., Stutzmann, M. & Eickhoff, M. Al(x)Ga(1-x)N-A New Material System for Biosensors. *Advanced Functional Materials* **13**, 841–846 (2003).

23. Steinhoff, G. *et al.* Recording of Cell Action Potentials with AlGaN⁄GaN Field-Effect Transistors. *Applied Physics Letters* **86**, 033901 (2005).

24. Cimalla, I. *et al.* AlGaN/GaN Biosensor-Effect of Device Processing Steps on the Surface Properties and Biocompatibility. *Sensors and Actuators B* **123**, 740–748 (2007).

25. Kokawa, T., Sato, T., Hasegawa, H. & Hashizume, T. Liquid-Phase Sensors Using Open-Gate AlGaN⁄GaN High Electron Mobility Transistor Structure. *Journal of Vacuum Science and Technology B* **24**, 1972 (2006).

26. Song, J. & Lu, W. Chemically Gated AlGaN⁄GaN Heterostructure Field Effect Transistors for Polar Liquid Sensing. *Applied Physics Letters* **89**, 223503 (2006).

27. Eickhoff, M. *et al.* Electronics and Sensors Based on Pyroelectric AlGaN/GaN Heterostructures - Part B: Sensor Applications. *Physica Status Solidi (c)* **1918**, 1908–1918 (2003).

28. Chen, K. H. *et al.* c-erbB-2 Sensing Using AlGaN⁄GaN High Electron Mobility Transistors for Breast Cancer Detection. *Applied Physics Letters* **92**, 192103 (2008).

29. Chu, B. H. *et al.* Enzyme-Based Lactic Acid Detection Using AlGaN⁄GaN High Electron Mobility Transistors with ZnO Nanorods Grown on the Gate Region. *Applied Physics Letters* **93**, 042114 (2008).

30. Kocha, S. S. Electrochemical Investigation of the Gallium Nitride-Aqueous Electrolyte Interface. *Journal of The Electrochemical Society* **142**, L238 (1995).

31. Steinhoff, G. *et al.* pH Response of GaN Surfaces and its Application for pH-Sensitive Field-Effect Transistors. *Applied Physics Letters* **83**, 177 (2003).

32. Siu, W. M. & Cobbold, R. S. C. Basic Properties of the Electrolyte-SiO2-Si System: Physical and Theoretical Aspects. *IEEE Transactions on Electron Devices* **26**, 1805–1815 (1979).

33. Yates, D. E., Levine, S. & Healy, T. W. Site-Binding Model of the Electrical Double Layer at the Oxide/Water Interface. *Journal of the Chemical Society, Faraday Transactions* **70**, 1807–1818 (1974).

34. Bayer, M., Uhl, C. & Vogl, P. Theoretical Study of Electrolyte Gate AlGaN⁄GaN Field Effect Transistors. *Journal of Applied Physics* **97**, 033703 (2005).

35. Rouviere, J. L., Weyher, J. L., Seelmann-Eggebert, M. & Porowski, S. Polarity Determination for GaN Films Grown on (0001) Sapphire and High-Pressure-Grown GaN Single Crystals. *Applied Physics Letters* **73**, 668 (1998).

36. Wong, M. H. *et al.* Power Performance of MBE-Grown N-Face High Electron Mobility Transistors with AIN Back Barrier. *Device Research Conference* **21**, 201–202. 23–25 June (2008).

37. Dabiran, A. M. *et al.* Very High Channel Conductivity in Low-Defect AlN/GaN High Electron Mobility Transistor Structures. *Applied Physics Letters* **93**, 082111 (2008).

38. Kotzar, G. *et al.* Evaluation of MEMS Materials of Construction for Implantable Medical Devices. *Biomaterials* **23**, 2737–50 (2002).

39. Kang, B. S. *et al.* Electrical Detection of Immobilized Proteins with Ungated AlGaN⁄GaN High-Electron-Mobility Transistors. *Applied Physics Letters* **87**, 023508 (2005).

40. Janata, J. & Moss, S. D. Chemically Sensitive Field-Effect Transistors. *Biomedical Engineering* **11**, 241 (1976).

41. Caras, S. & Janata, J. Field Effect Transistor Sensitive to Penicillin. *Analytical Chemistry* **52**, 1935–1937 (1980).

42. Caras, S. D., Janata, J., Saupe, D. & Schmitt, K. pH-Based Enzyme Potentiometric Sensors. Part 1. Theory. *Analytical Chemistry* **57**, 1917–20 (1985).

43. Dzyadevych, S. V., Soldatkin, A. P., El'skaya, A. V., Martelet, C. & Jaffrezic-Renault, N. Enzyme Biosensors Based on Ion-Selective Field-Effect Transistors. *Analytica Chimica Acta* **568**, 248–58 (2006).

44. Dzyadevich, S. V. *et al.* Application of Enzyme Field-Effect Transistors for Determination of Glucose Concentrations in Blood Serum. *Biosensors and Bioelectronics* **14**, 283–287 (1999).

45. Colapicchioni, C., Barbaro, A. & Porcelli, F. Fabrication and Characterization of ENFET Devices for Biomedical Applications and Environmental Monitoring. *Sensors and Actuators B* **6**, 202–207 (1992).

46. Dzyadevych, S. V. *et al.* Biosensors Based on Enzyme Field-Effect Transistors for Determination of some Substrates and Inhibitors. *Analytical and Bioanalytical Chemistry* **377**, 496–506 (2003).

47. Poghossian, A., Schöning, M. J., Schroth, P., Simonis, A. & Lüth, H. An ISFET-Based Penicillin Sensor with High Sensitivity, Low Detection Limit and Long Lifetime. *Sensors and Actuators B* **76**, 519–526 (2001).

48. Kharitonov, A. B., Zayats, M., Lichtenstein, A., Katz, E. & Willner, I. Enzyme Monolayer-Functionalized Field-Effect Transistors for Biosensor Applications. *Sensors and Actuators B* **70**, 222–231 (2000).

49. Zayats, M., Kharitonov, A. B., Katz, E., Bückmann, A. F. & Willner, I. An Integrated NAD+-Dependent Enzyme-Functionalized Field-Effect Transistor (ENFET) System: Development of a Lactate Biosensor. *Biosensors and Bioelectronics* **15**, 671–80 (2000).

50. Pijanowska, D. G. & Torbicz, W. pH-ISFET Based Urea Biosensor. *Sensors and Actuators B* **44**, 370–376 (1997).

51. Alexander, M. D. *et al.* Patient Radiation Exposure During Diagnostic and Therapeutic Interventional Neuroradiology Procedures. *Journal of Neurointerventional Surgery* **2**, 6–10 (2010).

52. Knoll, G. F. *Radiation Detection and Measurement*. (John Wiley & Sons, Inc.: Michigan, 2010).

53. Leybovich, L. B., Sethi, A. & Dogan, N. Comparison of Ionization Chambers of Various Volumes for IMRT Absolute Dose Verification. *Medical Physics* **30**, 119 (2003).

54. Lambert, J. *et al.* A Prototype Scintillation Dosimeter Customized for Small and Dynamic Megavoltage Radiation Fields. *Physics in Medicine and Biology* **55**, 1115–26 (2010).

55. Beddar, A. S. Plastic Scintillation Dosimetry and its Application to Radiotherapy. *Radiation Measurements* **41**, 124–133 (2006).

56. Vatnitsky, S. & Järvinen, H. Application of a Natural Diamond Detector for the Measurement of Relative Dose Distributions in Radiotherapy. *Physics in Medicine and Biology* **38**, 173–84 (1993).

57. Sellin, P. Recent Advances in Compound Semiconductor Radiation Detectors. *Nuclear Instruments and Methods in Physics Research A* **513**, 332–339 (2003).

58. Ehringfeld, C. *et al.* Application of Commercial MOSFET Detectors for in Vivo Dosimetry in the Therapeutic X-Ray Range from 80 kV to 250 kV. *Physics in Medicine and Biology* **50**, 289–303 (2005).

59. Peet, D. J. & Pryor, M. D. Evaluation of a MOSFET Radiation Sensor for the Measurement of Entrance Surface Dose in Diagnostic Radiology. *The British Journal of Radiology* **72**, 562–8 (1999).

60. Belau, E. *et al.* Charge Collection in Silicon Strip Detectors. *Nuclear Instruments and Methods* **214**, 253–260 (1983).

61. Buzhan, P. *et al.* Silicon Photomultiplier and its Possible Applications. *Nuclear Instruments and Methods in Physics Research A* **504**, 48–52 (2003).

62. Lechner, P. *et al.* Silicon Drift Detectors for High Resolution Room Temperature X-Ray Spectroscopy. *Nuclear Instruments and Methods in Physics Research A* **377**, 346–351 (1996).

63. Lindström, G., Moll, M. & Fretwurst, E. Radiation Hardness of Silicon Detectors – a Challenge from High-Energy Physics. *Nuclear Instruments and Methods in Physics Research A* **426**, 1–15 (1999).

64. Lauxtermann, S., Bronner, W., Ludwig, J. & Runge, K. Radiation Detection Using Integrated GaAs HEMT Electronics. *Nuclear Instruments and Methods in Physics Research A* **379**, 247–251 (1996).

65. Betzel, G. T., Lansley, S. P., Baluti, F., Reinisch, L. & Meyer, J. Operating Parameters of CVD Diamond Detectors for Radiation Dosimetry. *Nuclear Instruments and Methods in Physics Research A* **614**, 130–136 (2010).

66. Burgemeister, E. A. Dosimetry with a Diamond Operating as a Resistor. *Physics in Medicine and Biology* **26**, 269–75 (1981).

67. Bertuccio, G. & Casiraghi, R. Study of Silicon Carbide for X-Ray Detection and Spectroscopy. *IEEE Transactions on Nuclear Science* **50**, 175–185 (2003).

68. Pittet, P. *et al.* Implantable Real-Time Dosimetric Probe Using GaN as Scintillation Material. *Sensors and Actuators A* **151**, 29–34 (2009).

69. Grant, J. *et al.* GaN as a Radiation Hard Particle Detector. *Nuclear Instruments and Methods in Physics Research A* **576**, 60–65 (2007).

70. Vaitkus, J. A New Radiation Hard Semiconductor — Semi-Insulating GaN: Photoelectric Properties. *AIP Conference Proceedings* **772**, 207–208 (2005).

71. Vaitkus, J. *et al.* Semi-Insulating GaN and its Evaluation for α Particle Detection. *Nuclear Instruments and Methods in Physics Research A* **509**, 60–64 (2003).

72. Sellin, P. & Vaitkus, J. New Materials for Radiation Hard Semiconductor Dectectors. *Nuclear Instruments and Methods in Physics Research A* **557**, 479–489 (2006).

73. Rahman, M. *et al.* Super-Radiation Hard Detector Technologies : 3-D and Widegap Detectors. *IEEE Transactions on Nuclear Science* **51**, 2256–2261 (2004).

74. Duboz, J.-Y. *et al.* GaN for X-Ray Detection. *Applied Physics Letters* **92**, 263501 (2008).

75. Duboz, J.-Y., Beaumont, B., Reverchon, J.-L. & Wieck, A. D. Anomalous Photoresponse of GaN X-Ray Schottky Detectors. *Journal of Applied Physics* **105**, 114512 (2009).

76. Romero, M. A., Martinez, M. A. G. & Herczfeld, P. R. An Analytical Model for the Photodetection Mechanisms in High-Electron Mobility Transistors. *IEEE Transactions on Microwave Theory and Techniques* **44**, 2279–2287 (1996).

77. Subramanian, S. *et al.* A High-Gain, Modulation-Doped Photodetector Using Low-Temperature MBE-Grown GaAs. *IEEE Electron Device Letters* **16**, 20–22 (1995).

78. Huang, Y. *et al.* Photocurrent Characteristics of Two-Dimensional-Electron-Gas-Based AlGaN/GaN Metal-Semiconductor-Metal Photodetectors. *Applied Physics Letters* **96**, 243503 (2010).

79. de Salles, A. A. & Romero, M. A. Al(0.3)Ga(0.7)As/GaAs HEMT's Under Optical Illumination. *IEEE Transactions on Microwave Theory and Techniques* **39**, 2010–2017 (2010).

80. Khan, M. A., Shur, M. S., Chen, Q., Kuznia, J. N. & Sun, C. J. Gated Photodetector Based on GaN/AlGaN Heterostructure Field Effect Transistor. *Electronics Letters* **31**, 398 (1995).

81. Kuan, T.-M. *et al.* High Optical-Gain AlGaN/GaN 2 Dimensional Electron Gas Photodetectors. *Japanese Journal of Applied Physics* **42**, 5563–5564 (2003).

82. Chang, S. J. *et al.* Nitride-Based 2DEG Photodetectors with a Large AC Responsivity. *Solid-State Electronics* **47**, 2023–2026 (2003).

83. Zhou, J. J., Jiang, R. L., Wen, B., Liang, L. Y. & Ji, X. L. Influence of AlGaN/GaN Interface Polarization Fields on the Properties of Photoconductive Detectors. *Journal of Applied Physics* **95**, 5925 (2004).

84. Jiang, H., Egawa, T., Ishikawa, H., Shao, C. & Jimbo, T. Visible-Blind Metal-Semiconductor-Metal Photodetectors Based on Undoped AlGaN/GaN High Electron Mobility Transistor Structure. *Japanese Journal of Applied Physics* **43**, L683–L685 (2004).

85. Aktas, O. *et al.* 60Co Gamma Radiation Effects on DC, RF, and Pulsed I-V Characteristics of AlGaN/GaN HEMTs. *Solid-State Electronics* **48**, 471–475 (2004).

86. Hu, X. *et al.* The Energy Dependence of Proton-Induced Degradation in AlGaN/GaN High Electron Mobility Transistors. *IEEE Transactions on Nuclear Science* **51**, 293–297 (2004).

87. Hu, X. *et al.* Proton-Irradiation Effects on AlGaN/AlN/GaN High Electron Mobility Transistors. *IEEE Transactions on Microwave Theory and Techniques* **50**, 1791–1796 (2003).

88. Luo, B. *et al.* Influence of 60Co γ-Rays on DC Performance of AlGaN/GaN High Electron Mobility Transistors. *Applied Physics Letters* **80**, 604 (2002).

89. Luo, B. *et al.* High-Energy Proton Irradiation Effects on AlGaN/GaN High-Electron Mobility Transistors. *Journal of Electronic Materials* **31**, 437–441 (2002).

90. Luo, B. *et al.* Proton Irradiation of MgO- or Sc2O3 Passivated AlGaN/GaN High Electron Mobility Transistors. *Solid-State Electronics* **47**, 1015–1020 (2003).

91. Vitusevich, S. A. *et al.* Effects of γ-Irradiation on AlGaN/GaN-Based HEMTs. *Physica Status Solidi (a)* **195**, 101–105 (2003).

92. White, B. D. *et al.* Electrical, Spectral, and Chemical Properties of 1.8 MeV Proton Irradiated AlGaN/GaN HEMT Structures as a Function of Proton Fluence. *IEEE Transactions on Nuclear Science* **50**, 1934–1941 (2003).

93. Thomas, C. A., Springer, P. A., Loeb, G. E., Berwald-Netter, Y. & Okun, L. M. A Miniature Microelectrode Array to Monitor the Bioelectric Activity of Cultured Cells. *Experimental Cell Research* **74**, 61–6 (1972).

94. Connolly, P., Clark, P., Curtis, A. S. G., Dow, J. A. T. & Wilkinson, C. D. W. An Extracellular Microelectrode Array for Monitoring Electrogenic Cells in Culture. *Biosensors and Bioelectronics* **5**, 223–234 (1990).

95. Heer, F. *et al.* CMOS Microelectrode Array for the Monitoring of Electrogenic Cells. *Biosensors and Bioelectronics* **20**, 358–66 (2004).

96. Bergveld, P., Wiersma, J. & Meertens, H. Extracellular Potential Recordings by Means of a Field Effect Transistor Without Gate Metal, Called OSFET. *IEEE Transactions on Biomedical Engineering* **BME-23**, 136–144 (1976).

97. Estephan, E., Larroque, C., Cuisinier, F. J. G., Bálint, Z. & Gergely, C. Tailoring GaN Semiconductor Surfaces with Biomolecules. *Journal of Physical Chemistry B* **112**, 8799–8805 (2008).

98. Schoell, S. J. *et al.* Organic Functionalization of 3C-SiC Surfaces. *Langmuir (Submitted)* (2012).

99. Schoell, S. J. *et al.* Electrical Passivation and Chemical Functionalization of SiC Surfaces by Chlorine Termination. *Applied Physics Letters* **98**, 182106 (2011).

100. Howgate, J. *et al.* Photocatalytic Cleavage of Self-assembled Organic Monolayers on GaN Surfaces. *Materials Research Society: Fall Meeting, Surface Functionalization for Chemical and Biological Sensing.* 30 November – 4 December (2009).

101. Howgate, J. *et al.* Sensing applications of GaN-based devices. *International Symposium on Advances in Nanoscience.* 25–26 Oktober (2010).

102. Howgate, J., Schoell, S. J., Steins, W., Stutzmann, M. & Eickhoff, M. UV-induced patterning of organic monolayers on GaN. *The International Workshop on Nitride Semiconductors. WS7: Electronic devices.* 6–10 Oktober (2008).

103. Howgate, J. *et al.* Photocatalytic Cleavage of Self-Assembled Organic Monolayers by UV-Induced Charge Transfer from GaN Substrates. *Advanced Materials* **22**, 2632–2636 (2010).

104. Hauf, M. V. *et al.* Low-Frequency Noise in Diamond Solution-Gated Field Effect Transistors. *Applied Physics Letters* **97**, 093504 (2010).

105. Encabo, A. B., Howgate, J., Stutzmann, M., Eickhoff, M. & Sánchez-García, M. A. Ultrathin GaN/AlN/GaN Solution-Gate Field Effect Transistor with Enhanced Resolution at Low Source-Gate Voltage. *Sensors and Actuators B* **142**, 304–307 (2009).

106. Howgate, J. *et al.* Characterization of AlGaN/GaN Enzyme Modified Field Effect Transistors. *Deutsche Physikalische Gesellschaft: Halbleiterphysik* 26–30 March (2007).

107. Baur, B. *et al.* Catalytic Activity of Enzymes Immobilized on AlGaN/GaN Solution Gate Field-Effect Transistors. *Applied Physics Letters* **89**, 183901 (2006).

108. Thalhammer, S., Howgate, J., Hofstetter, M. & Stutzmann, M. Strahlendetektor und Messeinrichtung zur Detektion von Röntgenstrahlung. Patent: DE102011013057A1 (2011).

109. Thalhammer, S., Howgate, J., Hofstetter, M. & Stutzmann, M. Röntgenkamera zur ortsaufgelösten Detektion von Röntgenstrahlung. Patent: DE102011013058A1 (2011).

110. Thalhammer, S., Howgate, J., Hofstetter, M. & Stutzmann, M. Verfahren zur Detektion von Strahlung und Untersuchungseinrichtung zur strahlungsbasierten Untersuchung einer Probe. Patent: Pending (2012).

111. Howgate, J. *et al.* Ultrahigh Gain AlGaN/GaN High Energy Radiation Detectors. *Physica Status Solidi (a)* **8**, 1562–1567 (2012).

112. Hofstetter, M., Howgate, J., Sharp, I. D., Stutzmann, M. & Thalhammer, S. Development and Evaluation of Gallium Nitride-Based Thin Films for X-Ray Dosimetry. *Physics in Medicine and Biology* **56**, 3215–31 (2011).

113. Thalhammer, S., Howgate, J., Hofstetter, M. & Stutzmann, M. GaN Halbleiterstrukturen als biophysikalische Zellaktivitätssensoren / Semiconductor Biosensors. Patent: WO2010142773A2 (2010).

114. Hofstetter, M. *et al.* In Vitro Bio-Functionality of Gallium Nitride. *Biochemical and Biophysical Research Communications* **424**, 348–353 (2012).

115. Hofstetter, M. *et al.* Strahlenbiophysik, Strahleneffekte –Dosimeter oder Biosensor? *Labor&More* **4**, 52–54 (2011).

116. Hofstetter, M. *et al.* Real-Time X-Ray Response of Biocompatible Solution Gate AlGaN/GaN High Electron Mobility Transistor Devices. *Applied Physics Letters* **96**, 092110 (2010).

117. Murphy, M. J. *et al.* High-Frequency AlGaN/GaN Polarization-Induced High Electron Mobility Transistors Grown by Plasma-Assisted Molecular-Beam Epitaxy. *Applied Physics Letters* **75**, 3653 (1999).

118. Kim, H. S., Yeom, G. Y., Lee, J. W. & Kim, T. I. Characteristics of Inductively Coupled Cl/BCl Plasmas During GaN Etching. *Journal of Vacuum Science and Technology A* **17**, 2214 (1999).

119. Hollering, M. *et al.* Electronic and Atomic Structure of the 6H-SiC (0001) Surface Studied by ARPES, LEED, and XPS. *Physical Review B* **58**, 4992 (1998).

120. Sieber, N. *et al.* PES and LEED Study of Hydrogen-and Oxygen-terminated 6H-SiC (0 0 0 1) and (0 0 0-1) Surfaces. *Applied Surface Science* **184**, 278–283 (2001).

121. Starke, U. *et al.* The (0001)-Surface of 6H—SiC: Morphology, Composition and Structure. *Applied Surface Science* **89**, 175–185 (1995).

122. Steenackers, M. *et al.* Structured Polymer Brushes on Silicon Carbide. *Chemistry of Materials* **22**, 272–278 (2010).

123. Datzmann, G. *et al.* The Munich Microprobe SNAKE: First Results Using 20 MeV Protons and 90 MeV Sulfur Ions. *Nuclear Instruments and Methods in Physics Research B* **181**, 20–26 (2001).

124. Dollinger, G. *et al.* Microirradiation of Cells with Energetic Heavy Ions. *Nuclear Instruments and Methods in Physics Research B* **231**, 195–201 (2005).

125. Hable, V. *et al.* The Live Cell Irradiation and Observation Setup at SNAKE. *Nuclear Instruments and Methods in Physics Research B* **267**, 2090–2097 (2009).

126. Ambacher, O. *et al.* Two-Dimensional Electron Gases Induced by Spontaneous and Piezoelectric Polarization Charges in N- and Ga-Face AlGaN/GaN Heterostructures. *Journal of Applied Physics* **85**, 3222 (1999).

127. Ibbetson, J. P. *et al.* Polarization Effects, Surface States, and the Source of Electrons in AlGaN/GaN Heterostructure Field Effect Transistors. *Applied Physics Letters* **77**, 250 (2000).

128. Harris, J. J., Pals, J. A. & Woltjer, R. Electronic Transport in Low-Dimensional Structures. *Reports on Progress in Physics* **52**, 1217–1266 (1989).

129. Lin, Y. C., Chang, S. J., Su, Y. K., Shei, S. C. & Hsu, S. J. Inductively Coupled Plasma Etching of GaN Using Cl2/He Gases. *Materials Science and Engineering B* **98**, 60–64 (2003).

130. Fay, M. W. *et al.* Structural and Electrical Characterization of AuPdAlTi Ohmic Contacts to AlGaN/GaN with Varying Ti Content. *Journal of Applied Physics* **96**, 5588 (2004).

131. Ruvimov, S. *et al.* Microstructure of Ti/Al and Ti/Al/Ni/Au Ohmic Contacts for n-GaN. *Applied Physics Letters* **69**, 1556 (1996).

132. Lin, Y.-J., Chen, Y.-M., Cheng, T.-J. & Ker, Q. Schottky Barrier Height and Nitrogen–Vacancy-Related Defects in Ti Alloyed Ohmic Contacts to n-GaN. *Journal of Applied Physics* **95**, 571 (2004).

133. Mohammed, F. M., Wang, L., Adesida, I. & Piner, E. The Role of Barrier Layer on Ohmic Performance of Ti/Al-Based Contact Metallizations on AlGaN/GaN Heterostructures. *Journal of Applied Physics* **100**, 023708 (2006).

134. Wang, D.-F. *et al.* Low-Resistance Ti/Al/Ti/Au Multilayer Ohmic Contact to n-GaN. *Journal of Applied Physics* **89**, 6214 (2001).

135. Duan, X. & Lieber, C. M. Laser-Assisted Catalytic Growth of Single Crystal GaN Nanowires. *Journal of the American Chemical Society* **122**, 188–189 (2000).

136. Kipshidze, G. *et al.* Controlled Growth of GaN Nanowires by Pulsed Metalorganic Chemical Vapor Deposition. *Applied Physics Letters* **86**, 033104 (2005).

137. Furtmayr, F. *et al.* Nucleation and Growth of GaN Nanorods on Si (111) Surfaces by Plasma-Assisted Molecular Beam Epitaxy - The Influence of Si- and Mg-Doping. *Journal of Applied Physics* **104**, 034309 (2008).

138. Li, Y. *et al.* Dopant-Free GaN/AlN/AlGaN Radial Nanowire Heterostructures as High Electron Mobility Transistors. *Nano Letters* **6**, 1468–73 (2006).

139. Liu, S., Cai, Y., Gu, G., Wang, J. & Zeng, C. Enhancement-Mode Operation of Nanochannel Array (NCA) AlGaN/GaN HEMTs. *Device Letters, IEEE* **33**, 354–356 (2012).

140. Ohi, K. & Hashizume, T. Drain Current Stability and Controllability of Threshold Voltage and Subthreshold Current in a Multi-Mesa-Channel AlGaN/GaN High Electron Mobility Transistor. *Japanese Journal of Applied Physics* **48**, 081002 (2009).

141. Steinhoff, G. *Selected Topics of Semiconductor Physics and Technology 94: Group III-Nitrides for Bio- and Electrochemical Sensors.* (Walter Schottky Institut, Technische Universität München: 2008).

142. Sze, S. M. *Physics of Semiconductor Devices*. (Wiley & Sons: 1982).

143. Bard, A. J. & Faulkner, L. R. *Electrochemical Methods: Fundamentals and Applications*. (Wiley & Sons: 2001).

144. Stern-Hamburg, H. O. Zur Theorie der Elektrolytischen Doppeldchicht. *Zeitschrift für Elektrochemie und Angewandte Physikalische Chemie* **30**, 508–516 (1924).

145. Harris, D. C. *Quantative Chemical Analysis*. (W. H. Freeman and Company: 2007).

146. Bousse, L., De Rooij, N. F. & Bergveld, P. Operation of Chemically Sensitive Field-Effect Sensors as a Function of the Insulator-Electrolyte Interface. *Electron Devices, IEEE Transactions on* **30**, 1263–1270 (1983).

147. Fung, C. D., Cheung, P. W. & Ko, W. H. A Generalized Theory of an Electrolyte-Insulator-Semiconductor Field-Effect Transistor. *IEEE Transactions on Electron Devices* **33**, 8–18 (1986).

148. Garrido, J. A. *et al.* pH Sensors Based on Hydrogenated Diamond Surfaces. *Applied Physics Letters* **86**, 073504 (2005).

149. Hubbell, J. H. & Seltzer, S. M. Tables of X-Ray Mass Attenuation Coefficients and Mass Energy-Absorption Coefficients from 1 keV to 20 MeV for Elements Z = 1 to 92 and 48 Additional Substances of Dosimetric Interest. at <http://www.nist.gov/pml/data/xraycoef/index.cfm>

150. Berger, M. J. *et al.* XCOM: Photon Cross Sections Database. at <http://www.nist.gov/pml/data/xcom/index.cfm>

151. Sugimura, H., Ushiyama, K., Hozumi, A. & Takai, O. Micropatterning of Alkyl- and Fluoroalkylsilane Self-Assembled Monolayers Using Vacuum Ultraviolet Light. *Langmuir* **16**, 885–888 (2000).

152. Ye, T., Wynn, D., Dudek, R. & Borguet, E. Photoreactivity of Alkylsiloxane Self-Assembled Monolayers on Silicon Oxide Surfaces. *Langmuir* **17**, 4497–4500 (2001).

153. Norrod, K. L. & Rowlen, K. L. Ozone-Induced Oxidation of Self-Assembled Decanethiol: Contributing Mechanism for “Photooxidation”? *Journal of the American Chemical Society* **120**, 2656–2657 (1998).

154. Wasserman, S. R., Tao, Y. T. & Whitesides, G. M. Structure and Reactivity of Alkylsiloxane Monolayers Formed by Reaction of Alkyltrichlorosilanes on Silicon Substrates. *Langmuir* **5**, 1074–1087 (1989).

155. Smith, R. K., Lewis, P. A. & Weiss, P. S. Patterning Self-Assembled Monolayers. *Progress in Surface Science* **75**, 1–68 (2004).

156. Ruan, C.-M., Bayer, T., Meth, S. & Sukenik, C. N. Creation and Characterization of n-Alkylthiol and n-Alkylamine Self-Assembled Monolayers on 316L Stainless Steel. *Thin Solid Films* **419**, 95–104 (2002).

157. Le Grange, J. D., Markham, J. L. & Kurkjian, C. R. Effects of Surface Hydration on the Deposition of Silane Monolayers on Silica. *Langmuir* **9**, 1749–1753 (1993).

158. Boulas, C., Davidovits, J. V., Rondelez, F. & Vuillaume, D. Suppression of Charge Carrier Tunneling Through Organic Self-Assembled Monolayers. *Physical Review Letters* **76**, 4797–4800 (1996).

159. Amy, F. *et al.* Radiation Damage to Alkyl Chain Monolayers on Semiconductor Substrates Investigated by Electron Spectroscopy. *Journal of Physical Chemistry B* **110**, 21826–32 (2006).

160. Ballav, N., Weidner, T. & Zharnikov, M. UV-Promoted Exchange Reaction as a Tool for Gradual Tuning the Composition of Binary Self-Assembled Monolayers and Chemical Lithography. *Journal of Physical Chemistry C* **111**, 12002–12010 (2007).

161. Brewer, N. J., Janusz, S., Critchley, K., Evans, S. D. & Leggett, G. J. Photooxidation of Self-Assembled Monolayers by Exposure to Light of Wavelength 254 nm: a Static SIMS Study. *Journal of Physical Chemistry B* **109**, 11247–56 (2005).

162. Lee, J. P. *et al.* Photocatalytic Decomposition of Alkylsiloxane Self-Assembled Monolayers on Titanium Oxide Surfaces. *Journal of Physical Chemistry B* **107**, 8997–9002 (2003).

163. Haick, H. & Paz, Y. Remote Photocatalytic Activity as Probed by Measuring the Degradation of Self-Assembled Monolayers Anchored near Microdomains of Titanium Dioxide. *Journal of Physical Chemistry B* **105**, 3045–3051 (2001).

164. Kawahara, K., Ohko, Y., Tatsuma, T. & Fujishima, A. Surface Diffusion Behavior of Photo-Generated Active Species or Holes on TiO2 Photocatalysts. *Physical Chemistry Chemical Physics* **5**, 4764 (2003).

165. Salomon, A. *et al.* What is the Barrier for Tunneling Through Alkyl Monolayers? Results from n- and p-Si–Alkyl/Hg Junctions. *Advanced Materials* **19**, 445–450 (2007).

166. Chakrapani, V. *et al.* Electrochemical Pinning of the Fermi Level: Mediation of Photoluminescence from Gallium Nitride and Zinc Oxide. *Journal of the American Chemical Society* **130**, 12944–52 (2008).

167. Bisswanger, H. *Front Matter, in Enzyme Kinetics: Principles and Methods*. (Wiley-VCH Verlag GmbH & Co. KGaA: Weinheim, 2002).

168. Ogundiran, S. O., Varanasi, S. & Ruckenstein, E. Modeling of Enzyme-Potentiometric Sensors Involving Acid- or Base-Forming Reactions. *Biotechnology and Bioengineering* **37**, 160–76 (1991).

169. Fewell, T. R. & Shuping, R. E. Photon Energy Distribution of Some Typical Diagnostic X-Ray Beams. *Medical Physics* **4**, 187 (1977).

170. Brenner, D. J. Is it Time to Retire the CTDI for CT Quality Assurance and Dose Optimization? *Medical Physics* **32**, 3225 (2005).

171. Chuang, C. F., Verhey, L. J. & Xia, P. Investigation of the use of MOSFET for Clinical IMRT Dosimetric Verification. *Medical Physics* **29**, 1109 (2002).

172. Yoshizumi, T. T. *et al.* Validation of Metal Oxide Semiconductor Field Effect Transistor Technology for Organ Dose Assessment During CT: Comparison with Thermoluminescent Dosimetry. *American Journal of Roentgenology* **188**, 1332–6 (2007).

173. Razeghi, M. & Rogalski, A. Semiconductor Ultraviolet Detectors. *Journal of Applied Physics* **79**, 7433 (1996).

174. Ma, L. *et al.* Comparison of Different GaN Etching Techniques. *CS Mantech Conference* 105–108. April (2006).

175. Muñoz, E. *et al.* Photoconductor Gain Mechanisms in GaN Ultraviolet Detectors. *Applied Physics Letters* **71**, 870 (1997).

176. Li, J. Z., Lin, J. Y., Jiang, H. X. & Khan, M. a. Effects of Persistent Photoconductivity on the Characteristic Performance of an AlGaN/GaN Heterostructure Ultraviolet Detector. *Applied Physics Letters* **72**, 2868 (1998).

177. Kordos, P. *et al.* Material and Device Issues of GaN-Based HEMTs. *8th IEEE International Symposium on High Performance Electron Devices for Microwave and Optoelectronic Applications* 61–66 (2000).

178. Asif Khan, M., Shur, M. S. & Chen, Q. High Transconductance AlGaN/GaN Optoelectronic Heterostructure Field Effect Transistor. *Electronics Letters* **31**, 2130 (1995).

179. Mohammad, S. N. *et al.* Photoluminescence Characterization of the Quantum Well Structure and Influence of Optical Illumination on the Electrical Performance of AlGaN/GaN Modulation-Doped Field-Effect Transistors. *Applied Physics Letters* **69**, 1420 (1996).

180. Li, J. Z., Lin, J. Y., Jiang, H. X., Asif Khan, M. & Chen, Q. Persistent Photoconductivity in a Two-Dimensional Electron Gas System Formed by an AlGaN/GaN Heterostructure. *Journal of Applied Physics* **82**, 1227 (1997).

181. Nozaki, S., Feick, H., Weber, E. R., Micovic, M. & Nguyen, C. Compression of the DC Drain Current by Electron Trapping in AlGaN/GaN Modulation Doped Field-Effect Transistors. *Applied Physics Letters* **78**, 2896 (2001).

182. Ludlow, J. B., Davies-Ludlow, L. E. & White, S. C. Patient Risk Related to Common Dental Radiographic Examinations: The Impact of 2007 International Commission on Radiological Protection Recommendations Regarding Dose Calculation. *Journal of the American Dental Association* **139**, 1237–1243 (2008).

183. Shalish, I. *et al.* Yellow Luminescence and Fermi Level Pinning in GaN Layers. *Applied Physics Letters* **77**, 987 (2000).

184. Ponce, F. A., Bour, D. P., Götz, W. & Wright, P. J. Spatial Distribution of the Luminescence in GaN Thin Films. *Applied Physics Letters* **68**, 57 (1996).

185. Xu, Y. *et al.* pH and Salt Responsive Poly(N,N-Dimethylaminoethyl Methacrylate) Cylindrical Brushes and their Quaternized Derivatives. *Polymer* **49**, 3957–3964 (2008).

186. Moon, J. S. *et al.* Submicron Enhancement-Mode AlGaN/GaN HEMTs. *60th DRC. Conference Digest Device Research Conference* 23–24 (2002).

187. Chen, H. & Wang, M. Enhancement-mode AlGaN/GaN HEMTs Fabricated by Standard Fluorine Ion Implantation. *CS MANTECH Conference* 145–148.17–20 May (2010).

188. Uemoto, Y. *et al.* A Normally-off AlGaN/GaN Transistor with RonA=2.6mΩcm2 and BVds=640V Using Conductivity Modulation. *International Electron Devices Meeting* 1–4. 11–13 December (2006).

189. ICRU *Tissue Substitutes in Radiation Dosimetry and Measurement. Report 44* (International Commission on Radiation Units and Measurements: Bethesda, USA, 1989).

# 8 List of Figures

# 9 List of My Publications on the Topic of this Thesis

## 9.1 Peer-Reviewed Journal Publications

1. Schoell, S. J., Sachsenhauser, M., Oliveros, A., **Howgate, J.**, Stutzmann, M., Brandt, M. S., Frewin, C., Saddow, S., Sharp, I. D. Organic Functionalization of 3C-SiC Surfaces. *Langmuir (Submitted)* (2012).

2. **Howgate, J.**, Hofstetter, M., Schoell, S. J., Schmid, M., Schäfer, S., Zizak, I., Hable, V., Greubel, C., Dollinger, G., Thalhammer, S., Stutzmann, M., Sharp, I. D. Ultrahigh Gain AlGaN/GaN High Energy Radiation Detectors. *Physica Status Solidi (a)* **8**, 1562–1567 (2012).

3. Hofstetter, M., **Howgate, J.**, Schmid, M., Schoell, S. J., Sachsenhauser, M., Adigüzel, D., Stutzmann, M., Sharp, I. D., Thalhammer, S.
In Vitro Bio-Functionality of Gallium Nitride. *Biochemical and Biophysical Research Communications* **424**, 348–353 (2012).

4. Hofstetter, M., **Howgate, J.**, Sharp, I. D., Schmid, M., Stutzmann, M., Thalhammer, S. Strahlenbiophysik, Strahleneffekte –Dosimeter oder Biosensor? *Labor&More* **4**, 52–54 (2011).

5. Hofstetter, M., **Howgate, J.**, Sharp, I. D., Stutzmann, M., Thalhammer, S. Development and Evaluation of Gallium Nitride-Based Thin Films for X-Ray Dosimetry. *Physics in Medicine and Biology* **56**, 3215–31 (2011).

6. Schoell, S. J., **Howgate, J.,** Hoeb, M., Auernhammer, M., Garrido, J. A., Stutzmann, M., Sharp, I. D. Electrical Passivation and Chemical Functionalization of SiC Surfaces by Chlorine Termination. *Applied Physics Letters* **98**, 182106

(2011).

7. Hauf, M., Hess, L., **Howgate, J.**, Dankerl, M., Stutzmann, M., Garrido, J. A. Low-Frequency Noise in Diamond Solution-Gated Field Effect Transistors. *Applied Physics Letters* **97**, 093504 (2010).

8. **Howgate, J.**, Schoell, S. J., Hoeb, M., Steins, W., Baur, B., Hertrich, S., Nickel, B., Sharp, I. D., Stutzmann, M., Eickhoff, M. Photocatalytic Cleavage of Self-Assembled Organic Monolayers by UV-Induced Charge Transfer from GaN Substrates. *Advanced Materials* **22**, 2632–2636 (2010).

9. Hofstetter, M., **Howgate, J.**, Sharp, I. D., Funk, M., Stutzmann, M., Paretzke, H., Thalhammer, S. Real-Time X-Ray Response of Biocompatible Solution Gate AlGaN/GaN High Electron Mobility Transistor Devices. *Applied Physics Letters* **96**, 092110 (2010).

10. Encabo, A. B., **Howgate, J.**, Stutzmann, M., Eickhoff, M., Sánchez-García, M. A. Ultrathin GaN/AlN/GaN Solution-Gate Field Effect Transistor with Enhanced Resolution at Low Source-Gate Voltage. *Sensors and Actuators B* **142**, 304–307 (2009).

11. Baur, B., **Howgate, J.**, von Ribbeck, H.-G., Gawlina, Y., Bandalo, V., Steinhoff, G., Stutzmann, M., Eickhoff, M. Catalytic Activity of Enzymes Immobilized on AlGaN/GaN Solution Gate Field-Effect Transistors. *Applied Physics Letters* **89**, 183901 (2006).

## 9.2 Conference Proceeding

1. **Howgate, J.** *et al.* Sensing applications of GaN-based devices. *International Symposium on Advances in Nanoscience.* 25–26 Oktober (2010).

2. **Howgate, J.** *et al.* Photocatalytic Cleavage of Self-assembled Organic Monolayers on GaN Surfaces. *Materials Research Society: Fall Meeting, Surface Functionalization for Chemical and Biological Sensing.* 30 November – 4 December (2009).

3. **Howgate, J.**, Schoell, S. J., Steins, W., Stutzmann, M. & Eickhoff, M. UV-induced patterning of organic monolayers on GaN. *The International Workshop on Nitride Semiconductors. WS7: Electronic devices.* 6–10 Oktober (2008).

4. **Howgate, J.** *et al.* Characterization of AlGaN/GaN Enzyme Modified Field Effect Transistors. *Deutsche Physikalische Gesellschaft: Halbleiterphysik* 26–30 March (2007).

## 9.3 Patents

1. Thalhammer, S., **Howgate, J.**, Hofstetter, M. & Stutzmann, M. Verfahren zur Detektion von Strahlung und Untersuchungseinrichtung zur strahlungsbasierten Untersuchung einer Probe. Patent: Pending (2012).

2. Thalhammer, S., **Howgate, J.**, Hofstetter, M. & Stutzmann, M. Röntgenkamera zur ortsaufgelösten Detektion von Röntgenstrahlung. Patent: DE102011013058A1 (2011).

3. Thalhammer, S., **Howgate, J.**, Hofstetter, M. & Stutzmann, M. Strahlendetektor und Messeinrichtung zur Detektion von Röntgenstrahlung. Patent: DE102011013057A1 (2011).

4. Thalhammer, S., **Howgate, J.**, Hofstetter, M. & Stutzmann, M. GaN Halbleiterstrukturen als biophysikalische Zellaktivitätssensoren / Semiconductor Biosensors. Patent: WO2010142773A2 (2010).

# 10 Acknowledgements

Firstly, I would like to express my gratitude to my thesis advisor **Prof. Dr. Martin Stutzmann,** whose continuing thoughtful guidance and support forms the foundation of this work. I would also like to thank him for his assistance in acquiring my financial support and, in turn, also to acknowledge the support of the German Excellence Initiative via the Nanosystems Initiative Munich.

**Prof. Dr. Martin Eickhoff**, who made it possible for me to make my degree at the Walter Schottky Institute (Garching b. München) and Physics Department of the Technische Universität München and was my initial direct supervisor, I am especially grateful for his guidance through **Chapters 3** and **4**, which we worked on prior to and after his leaving the institute.

**Chapter 3:** I acknowledge **Vedran Bandalo** and **Florian Furtmayr** for providing me with the initial masks to work with and also **Sonja Matich** who helped me with focused ion beam milling that was provided by **Prof. Dr. Alex Holleitner**. I would also like to thank **A. Bengoechea Encaboa** and **Prof. Dr**. **M. A. Sanchez-Garcia** from the University Politecnica in Madrid for a productive collaboration on the ultrathin heterostructures.

To **Dr. Ian D. Sharp**, whom I collaborated with during the second half of this thesis, I am grateful for his many efforts during the work on **Chapters 4** and **5** which we worked on prior to and after his leaving the institute.

**Chapter 4:** I would like to convey my gratitude to **Sebastian Schöll** for very productive collaboration on the photocatalytic degradation project. I would also like to acknowledge the initial contributions of **Barbara Baur** and **Wiebke Steins** to this work, and furthermore, **Samira Hertrich** for the assistance with X-ray reflectivity provided by **Priv.-Doz. Dr. Bert Nickel** (Department für Physik and CeNS, Ludwig Maximilians-Universität München). I am grateful to **Jonathan Mackinnon** of the Max-Plank-Institute for Neurobiology (München) for providing fluorescent barrel proteins. I would also like to express my gratitude to **Sebastian Schöll** and **Dr. Ian Sharp** for the hard work we all

put into building the surface analytics system, and also to acknowledge the work and help with the former X-ray photoelectron spectroscopy system by **Olaf Weidemann** and the readily available assistance of **Michael Fischer**. Furthermore, I would like to convey my gratitude to **Barbara Baur** for a productive collaboration on the catalytic enzyme project, and thank **Dr. Marin Steenackers** and **Frank Deubel** for functionalizing devices with polymer-brushes.

**Chapter 5:** I am especially grateful to **Priv.-Doz. Dr. Stefan Thalhammer** (Helmholtz Zentrum München) and his group for the collaborative effort within the Nanosystems Initiative Munich. Furthermore, I would like to convey my gratitude to **Markus Hofstetter** for a productive collaboration. Moreover, I am grateful for the many very helpful discussions with **Sebastian Schöll** during this project. I acknowledge the Helmholtz-Zentrum Berlin - electron storage ring BESSY II for provision of synchrotron radiation at beamline 3.2. For the two one-week time slots at this facility I am exceptionally grateful for the assistance of **Markus Hofstetter**, **Martin Schmid, Susanne Schäfer**, **Dr. Ian D. Sharp**, and the beam line engineer **Dr. Ivo Zizak** for their help and dedication to keep the experiments running 24 hours a day. I also acknowledge the Maier-Leibnitz Laboratorium (Garching b. München) for access to the tandem accelerator provided by **Prof. Dr. Günther Dollinger** and the help of **Markus Hofstetter**, **Martin Schmid**, **Dr. Volker Hable**, and **Christoph Greubel**. I am also grateful for the assistance of **Dr. Ralf Mayer**, **Linda Mora** and **Gabi Riedl** with the deposition of $SiO_2$ and for the use of Nextnano$^3$ (Germany, Stefan Birner).

Lastly, but definitely not least, I would like acknowledge: **Priv.-Doz. Dr. Jose Garrido** for the helpful discussions and brief collaborative work we made together. **Sebastian Schöll** for the extended discussions and work we made; **Prof. Dr. Peter Vogl** for many very useful discussions, generosity and unwavering support; **Sebastian Schöll, Markus Hofstetter, Olaf Weidemann, Barbara Baur, Dr. Ian D. Sharp, Vedran Bandalo, Thomas Wassner, Vera Zon** the remaining members of **Prof. Dr. Martin Eickhoff's**, **Dr. Ian D. Sharp's** and **Priv.-Doz. Dr. Stefan Thalhammer's** groups and also the entire Walter Schottky Institute (Garching b. München) for the working environment.